UNIVERSITY OF CALIFORNIA
RIVERSIDE

Small Scale Structure:
A Local and Cosmological View of Dwarf Galaxies and Their Satellites

A Dissertation submitted in partial satisfaction
of the requirements for the degree of

Doctor of Philosophy

in

Physics

by

Ethan Jahn

September 2021

Dissertation Committee:

Dr. Laura Sales, Chairperson
Dr. Hai Bo Yu
Dr. Simeon Bird

The Dissertation of Ethan Jahn is approved:

_____

_____

_____

Committee Chairperson

University of California, Riverside

Acknowledgments

Thanks to my advisor Prof. Laura Sales for all her hard work in training me on the techniques used in this research and to the other members of the Astro Simulations group for being great teammates. Thanks also to the members of the FIRE Local Group collaboration for additional guidance and enlightening conversations, and the members of the SMUGGLE collaboration for their advice on a difficult research project. I especially want to thank the crew in POWUR for their dedication to equity, and for all the fun times we had together.

This dissertation is dedicated to Richard and Carol Genberg, who always inspired me to work hard and dream of the stars, as well as to my wonderful family whose support this could not have been done without.

ABSTRACT OF THE DISSERTATION

Small Scale Structure:
A Local and Cosmological View of Dwarf Galaxies and Their Satellites

by

Ethan Jahn

Doctor of Philosophy, Graduate Program in Physics
University of California, Riverside, September 2021
Dr. Laura Sales, Chairperson

Dwarf galaxies are sensitive tests of the ΛCDM cosmological model and the physics of galaxy formation. We use numerical simulations to investigate the interaction between galaxies, their DM halos, and their satellites. We study zoom-in simulations from the Feedback In Realistic Environments (FIRE) project to show that Large Magellanic Cloud (LMC)-mass centrals destroy fewer of their dark subhalos compared to Milky Way (MW)-mass centrals. Gaia proper motions provide new insight into the satellite population of the LMC, bringing it to 5 with $M_\star > 10^4$ $M_\odot$, consistent with our simulated satellite populations. The star formation histories of FIRE LMC-satellites have greater diversity than those of similar mass centrals and that the overall stellar mass dependence of the quenched fraction is consistent with previous results for MW satellites. LMC-mass halos can quench their satellites via ram-pressure stripping, sometimes aided by internal feedback processes. Gravitational interactions between the host and satellites can form stellar tidal streams around the host, which should be detectable in observations. We then use idealized simulations of a dwarf galaxy with both the Springel & Hernquist 2003 [SH03, 260] model and the `SMUGGLE` model [181] to investigate feedback-driven core formation. `SMUGGLE` produces bursty star formation, high

gas densities, and large fluctuations of gas content within the inner regions leading to the growth of a core, while the SH03 does not produce a feedback-driven core formation. We implement variations on the SMUGGLE model which all form cores, suggesting that detailed modeling is more important than parameter tuning. None of the SMUGGLE models produce gas components with rotational velocity profiles that trace the DM potential, systematically rising slower than the circular velocity profile. The rotational velocity profiles exhibit significant variation across time, suggesting that a diversity of rotation curves could be produced by feedback-driven gas kinematics alone.

Contents

List of Figures

List of Tables

Chapter 1

Introduction

The theoretical framework in which the following research is presented is known as ΛCDM, which includes the cosmological constant, Λ, referring to the observed acceleration of the expansion of the Universe [223], and Cold Dark Matter, the principle matter component of the Universe [133, 147]. Dark matter halos are extended structures of self-bound DM in which primordial gas condenses to form stars and galaxies [299]. Galaxy formation is studied through both empirical and theoretical methodology. This research primarily focuses on numerical simulations of galaxy formation, which implement effective models for relevant physical processes to self-consistently produce galaxies, often in an expanding universe with an ionizing UV background, and have been very successful in both reproducing observed trends and making robust predictions [100, 277, 242, 293, 127, 280]. This work primarily aims to address open questions in ΛCDM relating to small-scale[1] discrepancies between observations and numerical simulations [33], as well as to characterize certain aspects of dwarf galaxy formation from a theoretical perspective.

[1] that is, on the scale of individual galaxies and their satellites

Dwarf galaxies, due to their shallow potentials and low baryon fractions, represent ideal laboratories within which to study both galaxy formation and dark matter. Present-day sensitivity limits have restricted the observational study of dwarf galaxies, especially the faintest ones, to the Local Group (LG; the Milky Way (MW), Andromeda, and all galaxies within ~2 Mpc of each). Therefore, much effort has been put to studying MW-mass halos or LG-like pairs [e.g. 148, 256, 239, 6, etc.] and the formation of dwarf galaxies within such environments [29, 93, 293, 249, 97, 95, 31, 5]. Dwarf galaxies can be studied in isolation as primary centrals of their own environments [234, 297], but they often are found as substructure of larger halos, with the Large Magellanic Cloud (LMC; the MW's largest satellite) as a well-studied example. Recent works investigating the observed and predicted satellite population of the LMC have revealed that these environments, while less disruptive than MW-like centrals [132], can be host to significant populations of dwarf galaxies [62, 232, 292, 57, 134, 233, 64, 138, 207, 77, 237].

There are several aspects that are important to galaxy formation on the low-mass end. For example, as dark matter halos decrease in mass, they increase in abundance [113]. When examining the galaxies that live in these halos, it is found that they are proportionally smaller compared to higher mass galaxies like the Milky Way [33]. This points to an inefficiency in the galaxy formation process that affects low-mass halos, while leaving higher mass halos unaffected. One avenue of investigation into this process is to examine the relative abundance of dark subhalos and luminous satellites [97].

1.1 Satellites and Substructure

Since dark matter halos are the sites of galaxy formation, galaxies can be used to constrain the abundance and mass of DM halos predicted by various cosmological models. Therefore, understanding the connection between DM subhalos (local self-bound overdensities of DM within a parent halo), the satellite galaxies they contain, and their parent halos is an important task in modern cosmology. Subhalo abundances have largely been explored in the context of DM-only simulations [e.g. 261, 256, 111], where large volumes that provide statistical samples of DM halos are more computationally feasible. However, recent works have demonstrated that the baryonic component of halos, namely the central galaxy, plays a large role in shaping the abundance of substructure in the halo. A recent study [97] demonstrated that MW-mass halos destroy a large fraction of subhalos that come within the vicinity of the central galaxy as a result of strong tidal forces, leaving a substantially reduced population behind. However, as discussed in Chapter 2, dwarf galaxies on the scale of the LMC ($\sim$ 10 times smaller than the MW) do not destroy such a substantial portion of their substructure due to a smaller central galaxy relative to the size of the DM halo, i.e. its reduced $M_\star/M_{\rm halo}$.

The abundance of substructure leads directly to another long-standing (though arguably solved) problem in ΛCDM known as the 'missing satellites' problem [148, 189]. The problem states that there are fewer luminous satellites around the MW than expected from cosmological dark matter simulations, and its root is the difference in mass function shape between DM subhalos (steep) and observed satellite galaxies (shallow). This points to an inefficiency and incompleteness of galaxy formation in the regime of dwarf galaxies, worsening towards even lower masses (i.e. ultrafaints, with $M_\star < 10^5$ M$_\odot$). Early solutions to the missing satellites problem include the suppression of star formation via reionization heating [32] and incompleteness of observational data sets, particularly on

the faint end [248]. Computational and algorithmic advances have led to cosmological hydrodynamic simulations of MW-like halos that account for the inefficiencies of galaxy formation and implement models for reionization heating. These simulations have self-consistently resolved satellites down to the ultrafaint regime [293, 240, 6], with abundances that match updated observational counts of MW satellites [185].

While it can be argued that the MW no longer faces a missing satellite problem, properly accounting for the pre-infall satellites of the LMC has proven challenging [232, 234]. Its proximity provides a good opportunity for detailed observations of its satellites, which can be thought of as a scaled-down version of the MW satellite population. Further, its recent infall [137] suggests that it may be possible to dynamically infer its pre-infall satellite population and distinguish them from true MW satellites [23, 57]. This provides an appealing situation to test how our models of structure formation apply to a smaller scale within our own cosmic back yard. Recent works have predicted that several ultrafaint galaxies may be associated with the LMC-system [233, 138], as well as the intermediate-mass galaxies Carina & Fornax [132, 207], as discussed in Chapter 2. An effect of association with a larger system is sometimes referred to as 'pre-processing' and can result in lowered satellite densities, and perhaps the truncation of star formation at an earlier time than expected. These are broadly classified as environmental effects.

1.2 The Impact of Environment

The environments that galaxies are found within (i.e. their proximity to similar or more massive halos) naturally impacts many aspects of their formation. For example, it is known that environments correlate with morphology, color, and star formation rate (SFR) in satellite galaxies

[8, 143, 7, 49, 167, 9, 287], though most studies explore massive host halos and satellite galaxies at the heavy end of the dwarf regime (i.e. $M_\star \gtrsim 10^8$ $M_\odot$). An observationally testable question relating to the impacts of environments on their satellites is the fraction of quenched (non star-forming) galaxies around a given host, and how that depends on both host and satellite stellar mass. Within the Local Group (the MW, M31, and their satellites), it has been shown that the quiescent fraction rises as satellite stellar mass falls [289, 185, 291, 295]. Studies of LG and near-field dwarf galaxies have further corroborated this trend by demonstrating the dependence of HI abundance and star formation history (SFH) on environment [109, 108, 289]. In contrast to the high quenching fractions found in the LG, the Satellites of Galactic Analogs (SAGA) survey [178] showed that MW-mass systems outside the LG may have systematically lower quenched fractions, even at lower masses, indicating that the picture might be more complicated than indicated by the LG alone.

Star formation histories (SFHs) are a powerful tool to study the evolution and quenching of galaxies. Advances in observational techniques have allowed for detailed measurements of the SFHs of local dwarf galaxies [289, 290, 291]. Comparisons of this data with simulations [295, 98, 60, 249, 31, 5] have demonstrated that satellites of individual MW-mass hosts and satellites of Local Group-like pairs quench similarly, and form their stars earlier than comparable dwarf centrals, supporting the host-satellite interaction model for quenching. Of particular interest to this investigation is the quenching timescale, which compares the time of infall of a given satellite to its quenching time, which constrains the physics responsible for its quenching. For example, mass-dependent quenching models have been demonstrated [86, 295] wherein satellites with $M_\star = 10^{6-8}$ $M_\odot$ have short quenching time-scales consistent with ram-pressure stripping, while the longer quenching time-scales of higher mass satellites ($M_\star \gtrsim 10^8$ $M_\odot$) are consistent with starvation.

Interactions between satellites and their host galaxies are also known to produce observable features, such as stellar streams. Extensive work has been done to identify and characterize streams around the MW [129, 16, 136, 176, 119, 208], revealing evidence of close satellite encounters. While stellar streams have been identified outside the Local Group [177, 183, 182], few have been discovered around dwarf hosts [184, 39], and their cosmological frequency remains unknown.

Naturally, much attention has been given to the environments of MW-like halos in the literature, as the majority of high resolution observations are constrained to nearby galaxies. However, as next-generation surveys come online, data for systems outside the Local Group will become available [41, 66, 54], and theoretical constraints for a wide variety of host masses will be necessary to fully characterize the findings. Previous works have characterized properties of LMC analogs [44, 45, 72] or the predicted satellite population [134, 233, 138, 132, 207, 77, 237], but limited work has been done on characterizing the influence such environments have on observable properties of the satellite population, in particular their SFHs, quenched fractions, and tidal structures.

While baryonic physics can affect luminous objects in the vicinity of dwarf galaxies, it is also thought that their injection of energy into the interstellar medium via SN feedback and other processes is able to alter the structure of dark matter within the main halo as well.

1.3 The Structure of DM halos

One of the most well-tested predictions from ΛCDM is the structure of dark matter halos. Cosmological simulations containing only DM have robustly predicted the shape of the density profile of halos [e.g. 299, 256], which takes a universal form as a double power law, such as the Hernquist [120] or Navarro-Frenk-White [NFW - 196] profiles, among many others. No matter the

exact functional form, cold dark matter halos are universally predicted to have a steep inner density profile ('cusp') with $\rho_{\rm dm} \propto r^{-1}$. Potential theory allows the density profile to be reformulated as a rotation curve, with CDM halos predicted to have steeply rising inner velocities that plateau at $v_{\rm max}$ and remain constant toward the outer regions.

In contrast, observations of rotation curves have demonstrated that real galaxies do not universally follow this prediction. Measurements of dwarf galaxy rotation curves from gas kinematics have largely suggested that they follow what is known as a 'cored' profile - a slowly rising rotation curve (flattened inner density profile) [55, 102, 199, 200]. This structure is consistent with an expansion of the inner regions of a traditional CDM halo, and has been characterized as an 'inner mass deficit' [203]. As a greater number of detailed measurements of dwarf galaxy rotation curves have become available, this 'core-cusp' problem has complexified into something more akin to a 'uniformity versus diversity' problem, with predicted CDM halos having a universal form while observed galaxies exhibit a wide variety of rotation curves.

Various solutions to this discrepancy have been postulated, including more complex models of dark matter than the interactionless picture of CDM. These include warm dark matter [61, 20] and self-interacting dark matter [305, 255, 274], which has been fairly successful in reproducing diverse rotation curves [e.g. 222, 140]. Additionally, 'fuzzy' dark matter postulates that DM takes the form of an ultra-light scalar particle, creating a halo-sized Bose-Einstein condensate [128, 187, 159, 37]. These models provide plausible alternatives to ΛCDM that address discrepancies with observations [224, 27], but they may remain difficult to distinguish from CDM on small scales, especially when the effects of galaxy formation are taken into account [75, 87].

On the other hand, baryons have long been seen as a possible source for the expansion of DM halos, with early works suggesting that large outflows due to violent supernovae (SNe) could be capable of gravitationally perturbing the inner DM content such that a core is formed [195]. Further, theoretical models for how the motion of baryons can gravitational induce DM cores have been proposed [214]. While much progress has been made on cosmological hydrodynamic simulations that reproduce observed properties of galaxies [308, 279, 242, 122, 286], not all models have been able to produce cores [47, 22], and those that do struggle to reproduce the diversity of observed rotation curves [203, 202, 220, 69, 236, 238]. Much of the literature on this subject has pointed to the star formation density threshold as the source for the discrepancy between different galaxy formation models, indicating that interstellar gas must first condense to sufficiently high densities such that it dominates the gravitational potential of dark matter before being blown away via feedback [104, 174, 268, 59, 18, 241, 29, 69].

In this dissertation, we use numerical simulations to investigate some of the open questions discussed above. In particular, we focus our attention on the scale of the Milky Way's two largest satellites: the Large Magellanic Cloud, and the Small Magellanic Cloud. Galaxies in these size ranges are of particular interest due to their demonstrably different behavior in comparison to MW-like objects, yet their relative brightness on the scale of dwarf galaxies makes them promising candidates for observational searches, enabling the testability of the theoretical predictions that follow.

Chapter 2

Dark and luminous satellites of LMC-mass galaxies in the FIRE simulations

Within ΛCDM, dwarf galaxies like the Large Magellanic Cloud (LMC) are expected to host numerous dark matter subhalos, several of which should host faint dwarf companions. Recent Gaia proper motions confirm new members of the LMC-system in addition to the previously known SMC, including two classical dwarf galaxies ($M_\star > 10^5$ $M_\odot$; Carina and Fornax) as well as several ultra-faint dwarfs (Car2, Car3, Hor1, and Hyd1). We use the Feedback In Realistic Environments (FIRE) simulations to study the dark and luminous (down to ultrafaint masses, $M_\star$ ~6×10^3 $M_\odot$) substructure population of isolated LMC-mass hosts (M_{200m}= 1-3×10^{11} $M_\odot$) and place the Gaia + DES results in a cosmological context. By comparing number counts of subhalos in simulations with and without baryons, we find that, within 0.2 r_{200m}, LMC-mass hosts deplete ~30% of their

substructure, significantly lower than the ∼70% of substructure depleted by Milky Way (MW) mass hosts. For our highest resolution runs ($m_{\rm bary}$=880M$_\odot$), ∼ 5-10 subhalos form galaxies with $M_\star$ ≥ 10^4 M$_\odot$, in agreement with the 7 observationally inferred pre-infall LMC companions. However, we find steeper simulated luminosity functions than observed, hinting at observation incompleteness at the faint end. The predicted DM content for classical satellites in FIRE agrees with observed estimates for Carina and Fornax, supporting the case for an LMC association. We predict that tidal stripping within the LMC potential lowers the inner dark matter density of ultra faint companions of the LMC. Thus, in addition to their orbital consistency, the low densities of dwarfs Car2, Hyd1, and Hyd2 reinforce their likelihood of Magellanic association.

2.1 Introduction

The ΛCDM structure formation scenario predicts a nested hierarchy of dark matter (DM) halos, subhalos, and sub-subhalos at all mass scales from galaxy clusters to well below the molecular cooling limit of 10^6 M$_\odot$ [216, 299, 267, 256]. The abundance of substructure is thought to be nearly scale-free and self-similar. That is, the mass function of subhalos takes a universal form when normalized to the mass of the host [91, 153, 103, 303]. This means that objects from the most massive halos at the centers of giant clusters to isolated dwarf galaxies should host a similar distribution of DM substructure when normalized properly[1]. These halos and subhalos act as hosts of galaxy formation, providing potential wells in which gas can accumulate and condense into star forming regions. The fact that the relation between stellar mass M_* and halo mass is a near power-law below Milky Way (MW) masses [302, 11, 113, 191, 301], together with the near invariance of

[1]Though, disruption of subhalos and galaxies due to baryons complicates this relation, as described later

subhalo abundance, means that the number of satellite galaxies normalized to the stellar mass of the central is expected to be independent of host halo mass for $\log_{10}(M_*^{\rm host} / {\rm M}_\odot) = 7.25 - 11.75$ [234].

The local group, consisting of the Milky Way (MW), M31, and their numerous satellite galaxies, offers an ideal testing ground for ΛCDM. For instance, the Large Magellanic Cloud (LMC), the largest satellite of the MW, has long been speculated to host satellites of its own [172, 62, 232]. Recent observational missions including DES, SMASH, PAN-STARRS, ATLAS, and Gaia have revealed numerous dwarf galaxies in the vicinity of the Magellanic system [10, 65, 145, 150, 273, 158, 90], greatly expanding the population of potential LMC-satellites. Based on the orbital properties of these dwarfs, recent works ([233, 138], hereafter S17 and K18) have discovered several possible associations of dwarf galaxies to the LMC [see also 57, 134, 245]. According to S17 & K18, there are currently five firm candidates to LMC-system membership: the Small Magellanic Cloud (SMC), Car2, Car3, Hor1, Hyd1, as well as eight promising possible associations awaiting additional proper motion measurements: Dra2, Eri3, Hor2, Hyd2, Phx2, Ret3, Tuc4, and Tuc5. [207] have also suggested the possibility of LMC association for the classical dwarf galaxies Carina and Fornax. We expand on this claim in Section 2.4. Each new measurement marks a step closer to a complete picture of the pre-infall satellite population of the LMC, which will greatly inform our theories of galaxy formation.

While it is known that satellite galaxies trace substructure, it is unclear from a theoretical perspective exactly how the population of dark subhalos is mapped to a population of luminous companions. Cosmological N-Body (dark matter only, 'DMO') simulations (e.g. [196, 133, 261, 256]) and hydrodynamical baryonic simulations (e.g. [3, 105, 231, 28, 239, 293]) have been instrumental in making predictions for both central galaxies and smaller-scale subhalo and satellite

mass functions, as well as in revealing discrepancies between theoretical predictions of dark matter structure and the observed stellar structure that follows it.

Tension in predictions made by numerical simulations with the observed population of galaxies include the 'missing satellites' problem [148, 189] and 'too big to fail' ([25, 270, 146]; though see also [221, 201]), which address this mapping from dark to luminous substructure. Encouragingly, several solutions to such problems have been proposed, mostly invoking a combination of reionization heating, observational incompleteness, and the addition of realistic feedback modeling [32, 254, 293, 240, 286, 96, 249]. Furthermore, tides within the host potential affect subhalos. In particular, the addition of the gravitational potential of the central baryonic disk in MW-mass halos has been shown to suppress the presence and survival of dark matter subhalos compared to DMO runs [63, 97, 107]. With a smaller population of subhalos predicted, the number of eligible sites for satellite dwarf galaxies to form is also reduced, highlighting the need for a better understanding of the dark-to-luminous mass mapping predicted within ΛCDM. Because the central galaxy is the source of this effect, the actual efficacy of this effect depends on the $M_\star$ - $M_{\rm halo}$ ratio. Galaxies near the size of the MW have the highest $M_\star$ - $M_{\rm halo}$ ratio, while galaxies of both higher and lower stellar mass are observed to be hosted by fractionally larger halos, a trend which motivates exploring the magnitude of subhalo depletion by the central galaxy at different host mass scales.

Many of the above studies do not resolve satellite galaxies down to the scale of ultrafaints (UFs; $M_\star \lesssim 10^5$ $M_\odot$) - presumably, the most abundant class of galaxies in the universe. Since the satellite population of the LMC can be considered a scaled-down version of that of the MW, it is likely to be dominated by UFs, as the current (incomplete) population of LMC satellites seems to suggest. Due to their shallower gravitational potential, the effects of reionization at this scale of

galaxy formation are believed to be stronger than for more massive galaxies like the MW or classical dwarf spheroidals (though feedback effects are weaker since they form proportionally fewer stars). Thus, exploring the ultrafaint population of the LMC (and of LMC-mass hosts in general) is critically important to push the limits of our knowledge of dark-to-luminous substructure mapping into much fainter scales than currently known.

A possible avenue to overcome numerical resolution limitations in cosmological simulations is to focus on the formation of isolated dwarf galaxies. The lower masses and smaller sizes expected for dwarf halos translate into smaller mass per particle and smaller gravitational softening at a fixed number of particles compared to a more massive halo. For example, [297, 296] were able to study an extremely high resolution population of ultrafaint satellites in simulations of dwarf host halos in the scale $M_{200\mathrm{m}} \sim 10^{10}$ M$_\odot$. On average, $1-2$ ultrafaints were expected above $M_\star \geq 3 \times 10^3$ M$_\odot$, making important predictions for the numbers and distribution of ultrafaint dwarfs around dwarf galaxies in the field. Promisingly, larger numbers of ultrafaints shall be expected for more massive dwarf hosts. The inferred virial mass of the LMC, $\sim 10^{11}$ M$_\odot$ at the large end of the dwarf galaxy scale, promises to provide numerous substructures with which subhalo abundance can be studied. In addition, its recent infall to the MW ($1-3$ Gyr ago, [137]), means its satellite population will remain relatively undisturbed by the tidal field of the MW [232, 23, 57] and may offer an observational avenue to reconstruct its pre-infall satellite companions.

Previous theoretical works on local group satellite galaxies have predicted that ~30% of $M_\star \lesssim 10^5$ M$_\odot$ satellites of MW-mass hosts fell in as a satellite of a more massive galaxy [292], and that such groups of dwarf galaxies typically disperse in phase space about 5 Gyr after infall to a MW/M31 system [57]. In addition, [64] predicts ~ 8 large ultrafaint dwarf satellites of the LMC

using reionization and abundance matching models with the Caterpillar simulations [111]. However, such predictions are all based on DMO simulations missing important phenomena expected once the baryons are self-consistently taken into account, for example, SNe feedback, gas hydrodynamics affecting morphology, and tidal effects from the central baryonic disk.

In this chapter, we present the first analysis of satellite galaxies down to the ultra-faint mass scale in simulations of LMC-mass hosts, using the Feedback In Realistic Environments (FIRE) project. We investigate the luminous and dark substructure of these hosts in hopes of gleaning insight into the real history of the LMC-system. How many satellites, dark and luminous, did the LMC bring with it as it fell into the MW system? What is the mass distribution of these satellites? How have they been shaped by co-evolution with the LMC, and does this differ from satellites/substructures of the MW? Are there ways of constraining membership beyond orbital phase space similarity with the LMC?

This chapter is organized as follows: In Section 2.2 we descibe the FIRE simulations, incuding the feedback model, the zoom-in technique, halo finding, and resolution. We also describe our sample of LMC-mass zoom-in runs. In Section 2.3 we describe the effect of the central galaxy population of the abundance of subhalos as compared to DMO runs. In Section 2.4 we expand on the analysis of S17, K18, and [207] by analyzing Gaia orbital angular momenta of satellites in [90]. We compare the updated observationally inferred pre-infall mass function of the LMC to the satellite populations in our FIRE runs. We also investigate the structural kinematics of both observed and simulated dwarf satellites, with a focus on ultrafaint dSphs, and consideration of infall time and tidal stripping. We present a summary of this work and concluding remarks in Section 2.5.

2.2 Simulations

We analyze a sample of five cosmological zoom-in simulations of LMC-mass host galaxy systems from the Feedback In Realistic Environments project[2] (FIRE). These runs, implemented in the updated FIRE-2 scheme [127], use the fully conservative cosmological hydrodynamic code GIZMO[3] [121], a multi-method gravity plus hydrodynamics code, in its meshless finite-mass ("MFM") mode. This is a mesh-free Lagrangian finite-volume Godunov method which automatically provides adaptive spatial resolution while maintaining conservation of mass, energy, and momentum, and excellent shock-capturing and conservation of angular momentum, capturing advantages of both smoothed-particle hydrodynamics (SPH) and Eulerian adaptive mesh refinement (AMR) schemes (for extensive tests, see [121]). Gravity is solved with an improved version of the Tree-PM solver from GADGET-3 [257], with fully-adaptive (and fully-conservative) gravitational force softenings for gas (so hydrodynamic and force softenings are always self-consistently matched), following [217].

FIRE-2 implements a variety of methods for cooling, star formation, and stellar feedback processes. Heating and cooling rates are calculated across 10 - 10^{10}K, including CLOUDY ionization states for free-free, photoionization & recombination, Compton scattering, photoelectric, metal-line, molecular, fine structure, dust collisional, uniform cosmic ray heating, from a spatially uniform, redshift-dependent UV background [80]. Local self-shielding is accounted for using a Sobolev approximation. Stars are formed in accordance with [123], requiring gas to be locally self-gravitating, self-shielding [following 155], Jeans unstable, and with density $n_H > n_{\rm crit} = 1000$ cm^{-3}, with all

[2] http://fire.northwestern.edu

[3] http://www.tapir.caltech.edu/~phopkins/Site/GIZMO.html

Simulation	Resolution ($M_\odot$)	M_{200m} ($M_\odot$)	$M_\star$ ($M_\odot$)	r_{200m} (kpc)	V_{max} (km s^{-1})	min. V_{max} (km s^{-1})	N_{sub} $< 0.2r_{200m}$	N_{sub} $< 0.4r_{200m}$	N_{sub} $< r_{200m}$	N_{lum} $< r_{200m}$	Ref.
m11c	2100	1.5e11	8.2e8	167.4	81.0	2.5	9	34	118	9	1
m11d	7070	2.8e11	4.1e9	203.9	88.8	4.0	16	76	257	11	2
m11d-dmo	7070	3.4e11		216.5	95.4	4.8	21	95	333		3
m11e	7070	1.5e11	1.4e9	166.0	84.3	4.2	10	31	129	5	2
m11e-dmo	7070	1.8e11		176.2	92.1	4.6	4	34	162		3
m11q	880	1.5e11	3.4e8	168.7	81.0	1.7	17	56	123	8	4
m11q-dmo	880	1.9e11		182.5	91.2	1.8	20	81	192		4
m11v	7070	2.9e11	2.4e9	210.5	84.0	4.0	11	62	257	6	4
m12b	7070	1.4e12	7.3e10	335.1	180.9	4.2	19	125	544	25	5
m12b-dmo	7070	1.4e12		358.8	178.8	4.7	91	343	1116		5
m12c	7070	1.4e12	5.1e10	328.4	156.4	4.0	62	285	895	42	5
m12c-dmo	7070	1.3e12		350.0	154.1	4.4	156	537	1492		5
m12f	7070	1.7e12	6.9e10	354.7	183.4	4.0	34	202	863	31	4,5
m12f-dmo	7070	1.8e12		383.7	176.0	4.6	132	519	1693		4,5
m12i	7070	1.2e12	5.5e10	314.2	161.2	4.0	28	194	681	24	4,5
m12i-dmo	7070	1.2e12		339.3	162.3	4.8	103	431	1225		4,5
m12m	7070	1.6e12	1.0e11	341.6	184.3	4.3	48	259	900	40	4,5
m12m-dmo	7070	1.5e12		364.5	171.1	4.9	116	515	1622		4,5
m12r	7070	1.1e12	1.5e10	304.3	136.8	4.1	53	250	822	28	6
m12r-dmo	7070	1.1e12		322.6	146.0	4.8	95	420	1192		6
m12w	7070	1.1e12	4.8e10	300.5	156.2	4.5	33	181	638	31	6
m12w-dmo	7070	1.2e12		328.3	158.6	4.9	125	448	1167		6

Table 2.1: Properties of the host halo of all simulations analyzed herein for both the N-body dark matter only run (`-dmo`) and hydrodynamic run (no suffix) at $z = 0$. References for additional details on each simulation are shown in the rightmost column. Our primary sample, the LMC-mass `m11` hosts, are shown in the top block, and our reference sample, the MW-mass `m12` hosts, are shown below. Resolution refers to the baryonic mass resolution. All quantities are computed from halo catalogs generated by the `ROCKSTAR` halo finder (calculated using DM particles unless the item explicitly refers to stellar quantities, e.g. $M_\star$). The minimum $V_{\rm max}$ is the median value for subhalos of $195<N_{\rm particles}<205$, and serves as an effective resolution limit for substructures in each simulation. This particle number was chosen in accordance with the [127] determination of DM convergence radii with the [215] criterion. The virial radius ($r_{\rm 200m}$) is the radius where the average interior DM density is equal to 200 times the mean matter density in the Universe. The number of subhalos within $0.2\times r_{\rm 200m}$, $0.4\times r_{\rm 200m}$, and $r_{\rm 200m}$ of the host are selected as having $V_{\rm max} > 5$ km s^{-1}, this cutoff value is chosen to include only confidently resolved subhalos in all simulations. Note that `m11c` and `m11v` do not have DMO versions. In the last column, we include the number of luminous satellites, defined as $M_\star > 0$, though, practically, the stellar mass of the smallest resolved satellite (and hence total number of resolved satellites) varies with resolution. All $M_{\rm 200m}$ and $M_\star$ for non-DMO `m12` simulations were taken from [235], as they include all mass components in the calculation of $M_{\rm 200m}$, as well as only include stellar mass associated with the galactic disk (i.e. excluding stellar mass contained in the stellar halo). References: 1 - [45]; 2 - [72]; 3 - [161]; 4 - [127]; 5 - [293]; 6 - [235].

conditions met. Global star formation efficiency is naturally self-regulated by feedback processes, with good observational agreement [204]. All newly formed star particles inherit mass and metallicity from their progenitor gas particles.

Stellar feedback quantities are tabulated from the stellar population model STARBUST99 [163], assuming a [154] IMF, including supernova Type Ia, II, and stellar winds, as detailed in [127] and [126]. Radiative feedback is modelled with the Locally Extincted Background Radiation in Optically-thin Networks (LEBRON) algorithm [127], accounting for absorbed photon momentum, photo-ionization, and photo-electric heating.

The zoom-in technique [142, 198] is implemented by first simulating a large, low-resolution cosmological box in which a convex Lagrangian region (at initial redshift) is then defined. The region contains all particles within $\sim 5 r_{\rm vir}$ at $z = 0$ and *not* containing a halo of similar mass to that of the primary, and is then reinitialized with higher resolution. This process is repeated to refine the

Lagrangian region until the intended resolution is reached, at which point it is re-simulated with dark matter, gas, and star particles, buffered by a region of lower resolution dark matter particles. Initial conditions[4] are generated with the MUSIC code [116], which implements a second-order Lagrangian perturbation theory to $z = 99$.

Structure and substructure are identified using an updated version of the ROCKSTAR halo finder [13], which implements 6+1 dimensional phase-space analysis to determine the particles that are gravitationally bound and assign them to (sub)halos. ROCKSTAR assigns mass to halos and subhalos using spherical overdensity calculations relative to a specified threshold, such as the critical density or the average matter density of the universe. Such quantities necessarily become ambiguous and unreliable when quantifying masses of substructure, because the mass density of such embedded objects is by definition above the chosen threshold. To circumvent this ambiguity, we will mostly refer to the maximum circular velocity as an analog for subhalo mass, because it is a more robust and well-defined metric. For numerical stability, we run ROCKSTAR using only dark-matter particles, and we assign star particles in post-processing using an iterative procedure. We first select star particles within a DM halo out to 0.8 $r_{\rm halo}$ and with velocities less than 2 $V_{\rm max}$ of the (sub)halo's center of mass velocity, and we iteratively compute stellar position and velocity (making sure the star particles and halo are coincident) until the total mass of star particles, $M_\star$, converges to <1%. See [235] for a more detailed description.

2.2.1 Resolution Convergence

All simulations analyzed herein contain no low-resolution particles within $\sim 3\ r_{\rm 200m}$ from the host center. However, the 7070 $M_\odot$ resolution runs naturally use fewer particles to represent

[4] http://www.tapir.caltech.edu/~phopkins/publicICs/

objects at a given mass than do the higher resolution runs, leading to convergence issues. For this reason, we have determined a minimum value for $V_{\rm max}$, above which subhalos have $\gtrsim$200 DM particles, as listed in Table 2.2. We make this cut for all subhalos analyzed herein, and all galaxies naturally fall above this threshold. Using two different resolution runs of `m11q` (7070 $M_\odot$ & 880 $M_\odot$), we found that the subhalo populations deviate around $V_{\rm max} \sim 4$ km/s, which is below our cutoff in $V_{\rm max}$. This is shown in Figure A.1.

2.2.2 Our Sample: LMC-like centrals and dark matter cores

Our centrals are selected in the halo mass range $M_{\rm 200m} = 1.5 - 3.4{\times}10^{11}$ $M_\odot$, where $M_{\rm 200m}$ refers to the mass measured within $r_{\rm 200m}$, defined as the radius at which the mean interior halo density equals 200 times the average matter density of the universe. The stellar masses of the centrals at $z = 0$ are in the range $M_\star = 0.34 - 4.1{\times}10^9$ $M_\odot$, compared to the $1.5{\times}10^9$ $M_\odot$ of the LMC [185]. These and other properties of our centrals are listed in Table 2.2. Our choice of '200m' (as opposed to '200c' which uses the critical density of the universe, $\rho_{\rm crit}$) is motivated by its closer physical proximity to the 'splashback' radius, in which all (dark) matter that has passed through the core of the halo is enclosed [see 294, section 2, for a detailed explanation].

We analyze the highest resolution runs available for each system. There are three "low"-resolution ($m_{\rm bary}$ = 7070 $M_\odot$) runs: `m11c, m11d, m11e`; one medium-resolution run ($m_{\rm bary}$ = 2100 $M_\odot$): `m11c`; and one high-resolution run ($m_{\rm bary}$ = 880 $M_\odot$): `m11q`. For the first part of this analysis, we consider `m11d`, `m11e`, and `m11q` to be our primary focus because they have counterpart DMO simulations, allowing a comparative analysis of subhalo populations between DMO and baryonic versions of the same system. We examine all runs in Section 2.4, where we investigate

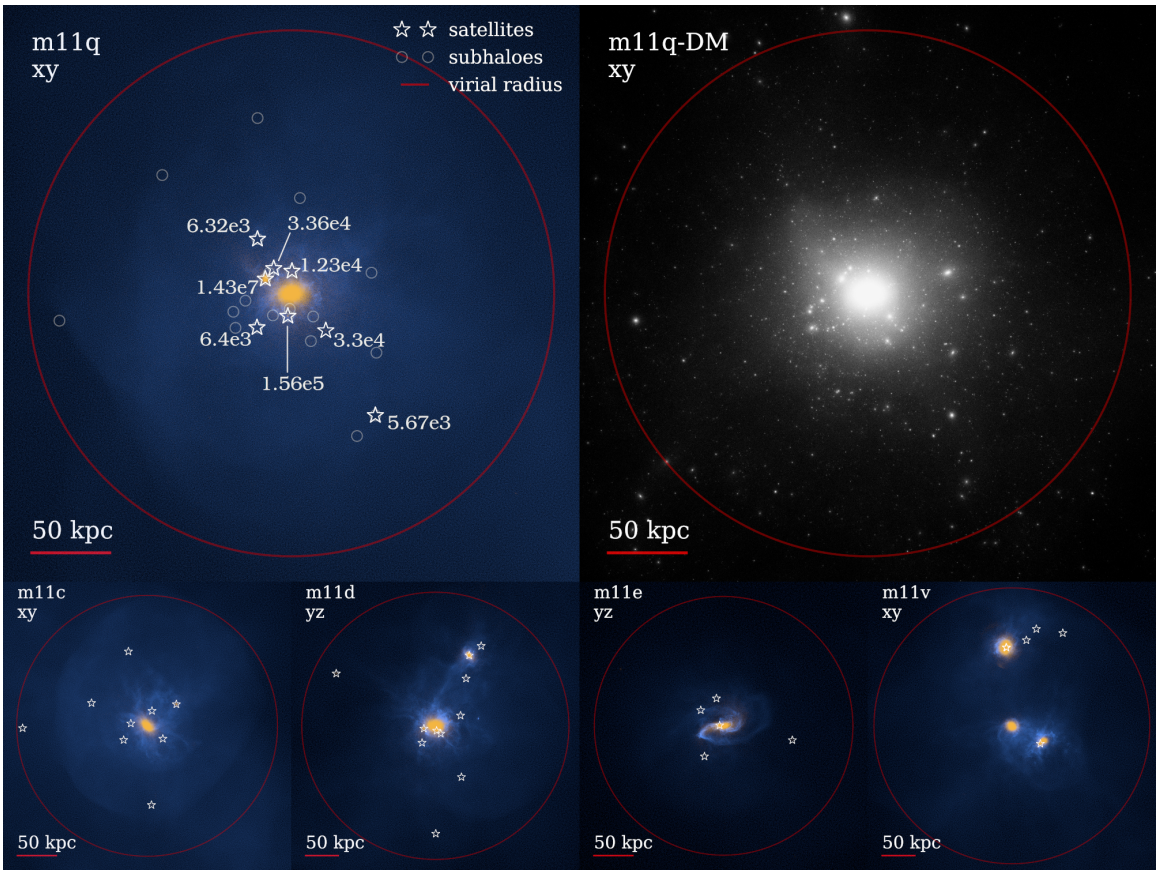

Figure 2.1: Projections of our sample of LMC-analog host galaxies in FIRE, with the virial radius (r_{200m}) of each host shown as a red circle. The top left panel shows a detailed projection of the highest resolution run, `m11q`, with stars in yellow and gas in blue. The fifteen subhalos of highest V_{max} (down to 9.6 km/s) are shown by grey circles, chosen only to give a visually representative sample of subhalos. All satellite galaxies are shown by grey star markers, with their stellar mass in solar masses ($M_\odot$) shown nearby. The dark matter content of the same simulation is shown in the top right panel - a few direct comparisons can be made between bright spots here and subhalo markers on the left. The bottom four panels show the stars and gas of `m11c`, `m11d`, `m11e`, and `m11v` with satellite galaxies located by star markers. All of our hosts are isolated in the sense that they are not within the realm of influence of a larger halo, such as the Milky Way. However, `m11v` is an ongoing multimerger, with two neighbors of stellar and virial masses $\lesssim$ that of the host. All other runs are unambiguously isolated.

the population of luminous companions around each host. All simulations were run with the core the FIRE-2 hydrodynamics and feedback models, while `m11q, m11d,` and `m11e` implemented an additional sub-grid model for the turbulent diffusion of metals in gas. By comparing `m11q` with and without this model, we have observed no difference in the mass and abundance of satellite galaxies, in agreement with [127] and [266], which quantified that including (or not including) metal diffusion physics did not change galaxy-wide properties. Phenomena sensitive to the physics of metal diffusion (such as metallicity gradients) are beyond the scope of this paper, so we proceed considering all runs equivalently.

To showcase our sample, the top panels in Fig. 2.1 show a visualization of the baryons (left) and the dark matter (right) within a region slightly larger than the virial radius of our highest resolution halo `m11q`. The dark matter component shows a large number of subhalos as expected within ΛCDM. On the left, stars (yellow) and gas (blue) have collapsed at the center of this LMC-mass halo to form the central dwarf, with $M_\star \sim 3{\times}10^8$ M$_\odot$. However, several other satellite subhalos have also formed stars giving rise to the population of dwarf satellites. We highlight them with starred symbols and annotate their corresponding stellar masses. The dark-to-luminous mapping at these low masses is complex, with only a few subhalos forming stars and the rest remaining dark companions. Circles on the left panel indicate the fifteen subhalos of highest $V_{\rm max}$ that have remained dark. The bottom row shows stars and gas for the rest of our sample and nicely illustrates the variations expected on the luminous companions of the LMC-mass halos.

Table 2.2 lists relevant properties of the LMC-analogs analyzed herein. Also listed, for comparison, is the Latte suite of isolated MW-mass hosts [see, e.g., 293, 97, hereafter GK17]. See section 2.2.3 for more details on these simulations. The selection of all LMC-like hosts was blind

with respect to satellite and subhalo population, aside from m11v, which was selected to have an ongoing merger at $z = 0$, as can be seen by its two companions, each with $M_\star \gtrsim M_\star(\mathrm{SMC}) \sim 4{\times}10^8$ $\mathrm{M}_\odot$. All were selected to be isolated from larger halos within $\sim 5\ r_{200\mathrm{m}}$.

At $z = 0$, our LMC-mass centrals all show a cored dark matter density profile (see left panel of Fig. 2.2) which contrasts with the denser and cuspy nature of the dark matter only runs (shown for halos m11q, m11d and m11e in dashed lines). This is better indicated in the bottom panel showing the ratio between the dark matter density in the dark matter only (DMO) run to the baryonic run, $\rho_{\mathrm{dmo}} / \rho_{\mathrm{hydro}}$, as a function of radius. Our LMC-mass centrals show $3 - 10$ times lower densities in the inner regions when the effect of baryons is included, an effect that is much larger than that observed in more massive $M_{200\mathrm{m}} \sim 10^{12}$ $\mathrm{M}_\odot$ hosts run with similar feedback[5] [293, 161, dot-dashed purple line showing results from Latte, e.g.].

The formation of cores in our LMC-like galaxies responds to the rapid removal of self-gravitating gas at the center of the halo due mainly to supernova explosions, which changes temporarily the potential at the center of the halos and leads to the "heat up" of the orbits of dark matter particles [196, 209, 214, 93]. This is consistent with the starbursty nature of star formation reported in FIRE simulations [198, 44, 73, 88] and also coincides with the regime where core formation due to the effect of baryons is expected to be maximal [58, 44, 271]. However, [74] showed that the degree of coring is subject to change on relatively short timescales as gas outflows and inflows change. This mass rearrangement also affects the circular velocity profiles, as shown by the right-hand panel of

[5] m11d and m11e are in the final stages of a merger at $z = 0$, making their cores seem larger due to the poorly defined center of each halo.

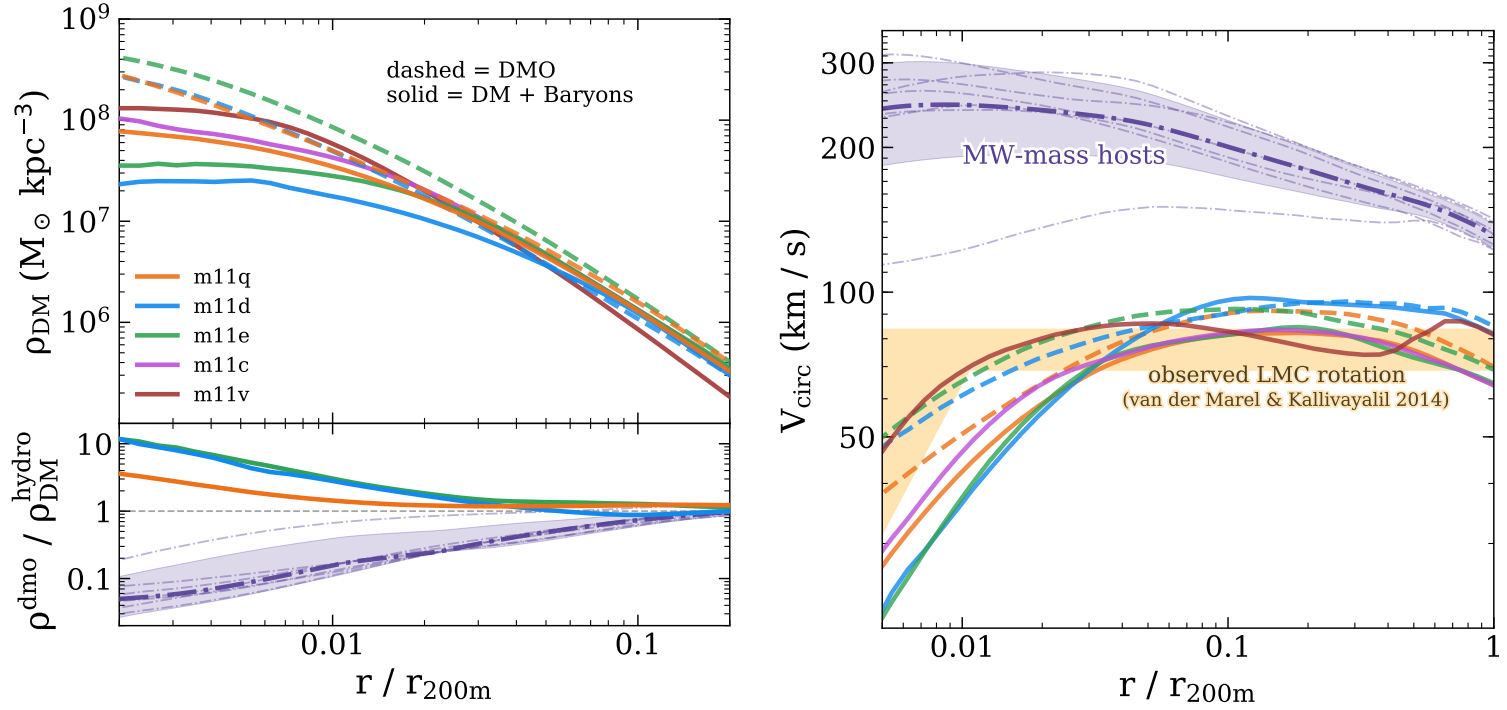

Figure 2.2: (Left) The top panel shows the DM density of FIRE LMC-mass hosts with distances normalized to r_{200m}. Dark Matter Only (DMO) runs are shown as dashed lines while the total mass density for the Hydro runs are shown as solid lines. The bottom panel shows the DMO-to-Hydro density ratio, which quantifies the degree of core-ing. This is shown for MW-mass hosts as the purple dashed-dot line, shaded for the 1σ deviation from the mean at $z = 0$. All `m11` runs are heavily cored in comparison to the MW-mass hosts. (Right) Circular velocity profiles of all hosts. V_{circ} for baryonic runs is calculated using total mass (DM + stars + gas). The observed circular velocity of the LMC is shaded in orange, representing a 1σ interval from a parameterized fit of proper motion measurements [276]. We find good agreement with our simulated LMC-mass hosts for r / $r_{200m} \gtrsim 0.04$, though all but `m11v` have somewhat lower circular velocities in the inner regions.

Fig. 2.2. Considering the effects of baryons, the maximum circular velocities of our halos are on the high end of agreement with that measured from HST proper motions of stars in the LMC [indicated by the orange shaded region 276].

2.2.3 Our Sample: MW-mass centrals

To highlight the dependence on host mass of many phenomena explored herein, we compare to the Latte suite of seven zoom-in simulations of MW-mass hosts (`m12b`, `m12c`, `m12f`, `m12i`, `m12m`, `m12r`, and `m12w`; introduced in [293]) with both baryonic and dark matter only runs, all with a baryonic mass resolution of 7070 $M_\odot$. All MW-mass hosts were blindly selected, with the exception of `m12r` and `m12w`, which were chosen to have an LMC-mass satellite at $z = 0$ in DMO [although, the LMC companion does not necessarily survive to $z = 0$ in the baryonic runs, see 235]. These simulations confidently resolve subhalos down to $V_{\rm max} \sim 4$ km/s, and luminous satellite galaxies down to $M_\star \sim 1{\times}10^5$ $M_\odot$ (galaxies with $M_\star < 1{\times}10^5$ $M_\odot$ are mostly found in the higher resolution runs). Halo masses range from (1.1 - 1.7)$\times10^{12}$ $M_\odot$, while stellar masses range from (1.5 - 10)$\times10^{10}$ $M_\odot$. The mean stellar mass to halo mass ratio is $\sim 6{\times}10^{-2}$, compared to $\sim 8{\times}10^{-3}$ for the LMC-mass hosts. As shown in Fig. 2.2, the central densities of the MW-mass hosts are much greater than those of our LMC-mass hosts, likely due to the effects of baryonic contraction [44]. This difference in host density is highly relevant to the discussion on subhalo abundances in the following section.

Any references to the names of various simulations are references specifically to the host/central galaxy of that simulation. The term 'companion' refers to a galaxy of nonzero stellar mass within $r_{\rm 200m}$ of its host, while 'subhalo' refers to the self-bound dark matter content of any object - luminous or dark - also within $r_{\rm 200m}$ of its host. 'Satellite' is a collective term for either.

As it is a common phrase, we also use the term 'vmeetingsirial radius' to refer to $r_{200\mathrm{m}}$, and 'virial mass' for $M_{200\mathrm{m}}$. Note that we do not use the Bryan & Norman [30] formulation for virial quantities.

2.3 Suppression of Dark matter subhalos in LMC-like hosts

The number of subhalos above a given V_{max}, referred to as the V_{max} function, is a useful metric to evaluate the abundance and scale of substructure hosted by a central halo. In the last decade, it has been found that the V_{max} function in MW-mass halos may be significantly suppressed when considering the increased tidal disruption due to the effect of the baryons in the central disk [63, 144, GK17]. The lower number of surviving subhalos results in a different prediction of the expected number of dwarfs around the MW and in particular for the inner regions where the suppression is maximal. This effect is critical for accurately predicting the radial distribution of satellites around the MW and M31 [235]. These and many other recent studies have primarily been concerned with massive host halos such as the MW. In this section we extend the scope of such inquiry to LMC-mass centrals, with a focus on the suppressing effect of the central baryonic galaxy, by comparing subhalo populations in dark matter only (DMO) simulations to subhalo populations of the same centrals simulated with hydrodynamics & baryonic physics.

Figure 2.3 shows the time-averaged subhalo V_{max} function of three LMC-mass hosts (orange - `m11q`; blue - `m11d`; green - `m11e`) as a cumulative count of subhalos at a given V_{max} and within different radial cuts from $r_{200\mathrm{m}}$ to 0.2 $r_{200\mathrm{m}}$ (left to right). Subhalos in each run are plotted from the highest V_{max} present to the minimum converged V_{max}, as listed in Table 2.2. Time-averaging was computed over the most recent ~1.3 Gyr, or $z \lesssim 0.1$ by sampling the V_{max} function of every host at each successive snapshot (66 in total), then computing the mean number of subhalos at

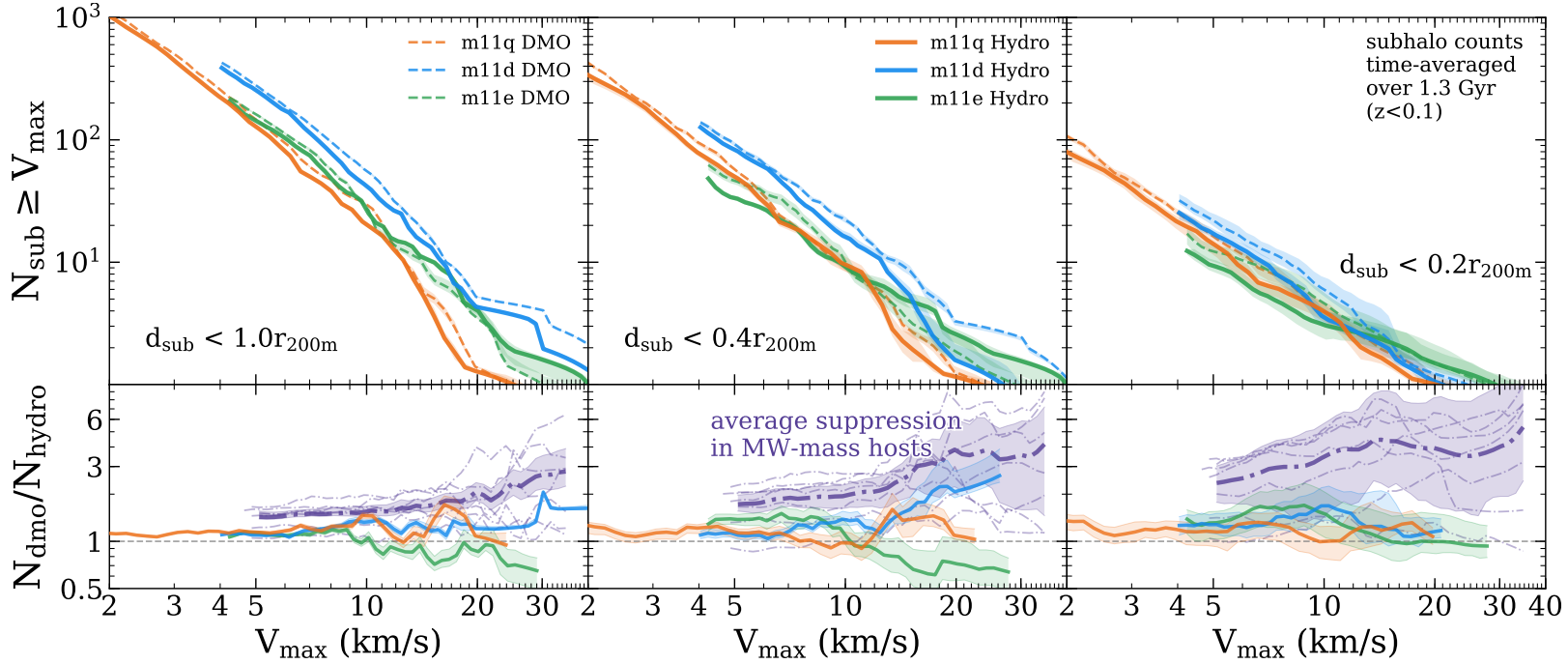

Figure 2.3: Cumulative time-averaged subhalo count above a given V_{max} within r_{200m} (left), 0.4 r_{200m} (center), and 0.2 r_{200m} (right) of the host. Counts are averaged over the last ~1.3 Gyr ($z < 0.1$) to account for fluctuations in subhalo counts as they pass in and out of each cutoff radius. Each line only extends down to the minimum V_{max} as listed in Table 2.2, and shaded regions indicate 1σ deviation from the mean count at a given V_{max}. Subhalo V_{max} in DMO simulations are normalized by $\sqrt{1 - f_b}$ to achieve a one-to-one comparison. The bottom panels quantify the magnitude of subhalo depletion as the ratio of the number of subhalos at each V_{max} in DMO to Hydro. The grey dotted line at $N_{dmo}/N_{hydro} = 1$ represents no depletion (subhalo populations are equivalent in both runs). The purple dashed lines on the bottom panel show the time-averaged depletion of subhalos in MW-mass halos at the corresponding fraction of r_{200m} for each host. We observe weaker depletion in the LMC mass halos as compared to the MW mass halos, consistent with a cored potential and lower stellar mass fraction. Table 2.2 shows the average amount of depletion for subhalos of $V_{max} = 10$ km/s for the radial cutoffs made here, for both LMC-mass and MW-mass hosts.

d_{sub} <	N_{dmo}/N_{hydro} r_{200m}	N_{dmo}/N_{hydro} 0.4 r_{200m}	N_{dmo}/N_{hydro} 0.2 r_{200m}
MW-mass	1.54±0.06	$1.98^{+0.28}_{-0.22}$	$3.51^{+1.82}_{-1.72}$
LMC-mass	$1.28^{+0.12}_{-0.1}$	$1.14^{+0.35}_{-0.23}$	$1.39^{+0.79}_{-0.58}$

Table 2.2: Average subhalo depletion (N_{dmo}/N_{hydro}) at V_{max} = 10 km/s for both MW-mass hosts ($M_{halo} \sim 10^{12}$ $M_\odot$) and LMC-mass hosts ($M_{halo} \sim 10^{11}$ $M_\odot$). Each column specifies the cutoff distance inside which subhalos are counted. Among LMC-mass hosts, we observe modest depletion ($N_{dmo}/N_{hydro} \approx 1.1 - 1.4$) of subhalos at all radii, while subhalo depletion is a strong function of distance for MW-mass hosts.

each V_{max}, including the 1σ deviation from the mean (shaded regions). Shading for the average depletion among the Latte suite of MW-mass simulations (bottom panels, purple dashed-dot lines) was calculated by adding the 1σ deviations in quadrature, for each run at each V_{max}. Within the virial radius of a $M_{200m} \sim 10^{11}$ $M_\odot$ halo, on average one can expect order 10 subhalos with V_{max} $\geq$ 10 km/s and order 10^2 above 5 km/s. We have explicitly checked that the radial distribution of those subhalos follows closely that of the dark matter in the host.

We additionally include the DMO subhalo populations of all hosts to illustrate how the additional baryonic potential and feedback effects change the distribution and total number of subhalos. This difference is quantified in the bottom panel where the number of subhalos at a given V_{max} in DMO is divided by that number in Hydro. A number greater than one represents 'suppression' or 'depletion' of subhalos in the Hydro run, while a number less than one means there are more subhalos at that V_{max} in Hydro than in DMO, or an 'enhancement' of substructure.

A close inspection of the bottom row in Fig. 2.3 shows that, on average, all subhalos with $V_{\rm max}$ < 15 km/s are only slightly suppressed (by a factor of $\sim$ 1.3) in hydro runs compared to the DMO version, an effect that increases only mildly when looking into the inner regions (middle and right panels). While time-averaging is indeed implemented to mitigate the discreteness of the sample, there are not many (<10) satellites with $V_{\rm max}$ > 15 km/s around LMC-like hosts and Poisson fluctuation may dominate. Take, for example, halo `m11e` (green). Although the middle panel seems to suggest an increase in the number of subhalos in the hydro run with respect to the DMO, the effect seems localized and it disappears for the inner regions (r < 0.2 $r_{\rm 200m}$, right panel). We interpret this as a local fluctuation that results from poor numbers statistics: only 6 subhalos exist with $V_{\rm max}$ = 10 km/s. We see that the overall trend in our LMC-mass hosts is a mild to negligible suppression of their subhalo populations by their central galaxies.

Also included in the bottom panel is the average suppression of subhalos for all MW-mass Latte hosts within the same fraction of their virial radii as our LMC-mass halos [see also GK17; 235]. In all panels we find that the level of suppression in our LMC-mass halos is significantly smaller than in MW-mass halos. This is most evident in the inner regions r < 0.2 $r_{\rm 200m}$, where subhalos are depleted by a factor $\sim 3-6$ in the `m12`'s compared to a maximum of $\lesssim$ 1.5 in our best resolved (though least cored) halo `m11q`. These results are mostly independent of the simulation method used. For example, using DMO runs with an added analytic disk [63] show that MW-mass environments suppress subhalos by a factor $\sim$ 3 at 10^7 $M_\odot$ ($V_{\rm max}$= $4-5$ km/s) within 30 kpc of the center, compared to at most a factor 2 found in our LMC-mass environments. The lower impact of baryons on the number of subhalos for LMC-mass hosts is consistent with previous arguments. Using hydrodynamical simulations and comparing to an analytic disk potential, GK17 showed that

the primary mechanism for suppression of substructure is the enhanced tidal stripping of subhalos by the gravitational potential of the central galaxy. This is due to two effects in the scale of MW-mass hosts. First, the extra component added to the gravitational forces by the presence of the disk and, second, by the dark matter halo itself becoming more concentrated in the presence of the disk leading to a steeper gravitational potential well.

We note that we find no correlation between substructure depletion and resolution. For instance, Fig. 2.3 shows that "normal" resolution (`m11d` and `m11e`) can show either more or less substructure depletion than the high resolution run `m11q`. There is therefore not an obvious systematic effect with resolution. Instead, substructure depletion may depend on the specifics of the central baryonic mass and accretion history of each halo. This is consistent with the lack of dependence in the resolution tests for $N_{\rm dmo}/N_{\rm hydro}$ in MW-mass hosts as examined in GK17 and [235].

In the case of hosts within the $M_{\rm 200m} = 10^{11}$ M$_\odot$ regime, as analyzed here, the fraction of mass in the disk is much smaller than in MW-mass objects ($\sim 1\%$ average for the LMC-analogs compared to $\sim 6\%$ for the MW-analogs) partially explaining the lower suppression of substructure. Additionally, the dark matter halos of LMC-hosts in Hydro are predicted to be less dense compared to their DMO counterparts (see Fig. 2.2) due to the effect of stellar feedback; opposite to the trend found in MW-mass hosts, which are dominated by baryonic contraction. We conclude that substructure depletion is less significant in dwarfs centrals than expected in $\sim L_*$ galaxies and that hundreds of dark matter subhalos with $V_{\rm max} > 5$ km/s are expected to be orbiting around field dwarf galaxies with mass comparable to the LMC.

2.3.1 Implications for Observational Subhalo Searches

Constraining the degree of subhalo suppression in regions near galaxies has strong implications on the viability of observational subhalo searches that are based on gaps in cold stellar streams. As noted by GK17, if all subhalos within 20 kpc of the MW are suppressed by the baryonic disk, it is less likely for surveys like Palomar-5 and GD-1 [38, 149] to detect any interaction with cold dark matter substructure (see also Chapman et al. (in prep), who detected a non-trivial infall rate of subhalos into the inner regions of FIRE MW-mass hosts, but that those subhalos are quickly destroyed). By examining the $z = 0$ radial distribution of substructures with $V_{\rm max} > 10$ km/s as seen in Figure A.3, we find that, on average, the MW-mass halos host no substructure within 30kpc (though individual halos may occasionally have a few subhalos in the range 20 kpc < $d_{\rm sub}$ < 30 kpc). On average, the LMC-mass halos are able to host substructure down to ~20 kpc, while retaining roughly a factor of two more subhalos than MW-mass hosts up to approximately 45kpc. The total number of subhalos hosted by MW-mass halos only surpasses that of LMC-mass halos at ~60-70 kpc. In addition, the overall reduced effect of host-subhalo tidal interactions make LMC-mass hosts somewhat cleaner systems to study substructure than their more strongly interacting MW-mass counterparts. We therefore argue that the study of cold streams around galaxies with $M_\star \sim 10^9$ $M_\odot$ may represent a more promising avenue to detect gaps associated to these dark subhalos.

Of course, the mass range of the substructure is also important. Previous work quantifying the sensitivity of cold stellar structures to disturbances by subhalos (e.g. [304]) suggest that streams such as Palomar-5 are sensitive to DM substructures in the mass range 10^7 to 10^9 $M_\odot$. The range of median subhalo masses with $V_{\rm max}$ present in the right panel of Figure 2.3 are 1.1×10^7 to 1.6×10^8 $M_\odot$, which, while on the lower end of the quoted sensitivity range, is still within the bounds. This

agreement supports our prediction that stellar streams near Magellanic-like systems may have more success that those in the vicinity of the MW-mass objects.

Indirectly, gravitational lensing searches are another avenue to probe dark matter substructure. Line ratio anomalies [46, 186] are strongly influenced by the degree of substructure predicted in the lens system. Novel methods using adaptive optics integral field spectroscopy to measure deviations in quasar narrow line emission [197] may require the expected correction due to the baryonic effects. Our results are highly relevant to such searches, suggesting LMC-mass hosts are more likely to maintain a significant amount of substructure in the mass ranges to which such methods are sensitive.

A core prediction of ΛCDM is that halos and subhalos act as sites of galaxy formation. We therefore expect that some fraction of the surviving dark matter subhalos discussed above in Section 2.3 surrounding our LMC-mass hosts will host a luminous component consisting of stars and gas. The fact that even faint galaxies are much easier to detect than dark subhalos makes the luminous companions of LMC-mass systems a direct and testable prediction of the galaxy formation + ΛCDM model. In light of recent results by Gaia regarding proper motions of several MW dwarfs, and under the assumption that the availability of 6D information allows one to reconstruct the previous associations of the LMC to other fainter dwarfs [233, 138], predictions are needed on the number and distribution of visible dwarf satellites expected to orbit around Magellanic dwarfs.

Fig. 2.4 highlights the mapping between the stellar mass content and the maximum circular velocities of the subhalos hosting luminous satellites with $M_\star \gtrsim 1{\times}10^4$ $M_\odot$ of our LMC-mass hosts. At $z = 0$, the relation shows significant scatter, meaning that, at a given $V_{\rm max}$, the corresponding

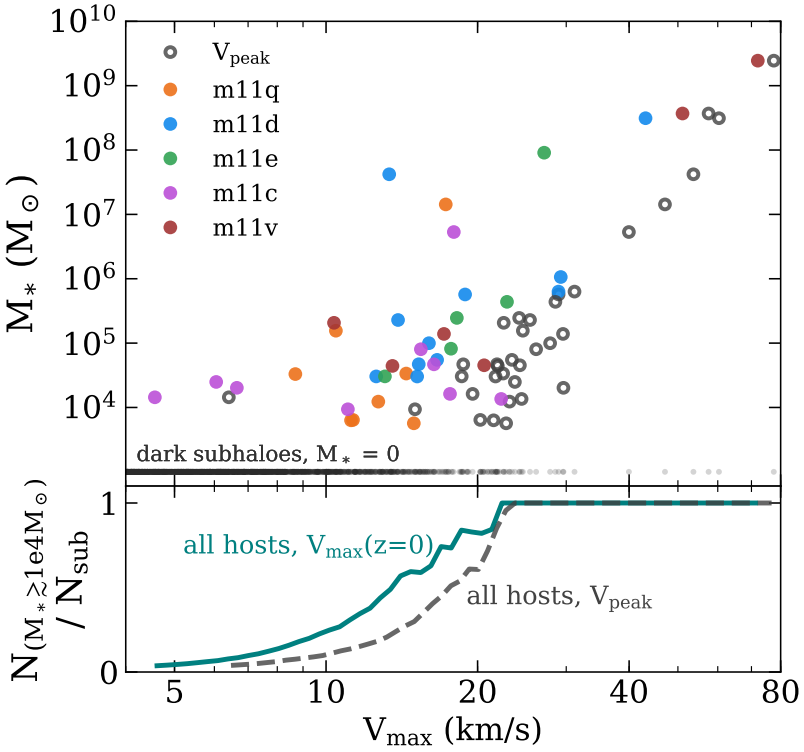

Figure 2.4: (Top) The $z = 0$ $V_{\rm max}$ (colored) and the peak $V_{\rm max}$ ever obtained (grey squares) of luminous $M_\star \gtrsim 1{\times}10^4$ M$_\odot$ companions within the virial radius versus their stellar mass. Subhalos with $V_{\rm max} \lesssim 20$ km/s show a scattered relation with stellar mass, reflecting the stochastic nature of galaxy formation at this scale. (Bottom) The fraction of luminous to dark subhalos at a given $V_{\rm max}$ or $V_{\rm peak}$, using the combined sample of all subhalos with $d_{\rm host} < r_{\rm 200m}$ of all hosts. The galaxy occupation fraction reaches unity for subhalos around $V_{\rm max} \sim 20$ km/s, though the distribution of current $V_{\rm max}$ has been shifted downwards, as expected due to tidal stripping of dark matter.

stellar content may vary by several orders of magnitude. This effect is partially explained by the tidal stripping of subhalos within the LMC-mass host. This is shown by the gray open symbols indicating the same relation but using the peak value ever obtained for the maximum circular velocity ($V_{\rm peak}$) of each satellite, roughly corresponding to its $V_{\rm max}$ at infall. A similar increase in scatter in the $M_\star$ – $V_{\rm max}$ relation has been observed for satellites in MW-mass hosts [e.g. 79], however, scatter in the $M_\star - V_{\rm peak}$ relation is lower. This could have implications for abundance matching relations at small mass scales [see e.g. 94]. We return to tidal effects in sub-section 2.4.3. Additional factors

contributing to the scatter is the stochasticity of the galaxy formation process near the low-mass end, as well as details of the assembly history of the halo and its inner dark matter density [88].

2.4 Dwarf satellites in LMC-like hosts

We note that only a small fraction of the dark matter companions host a luminous dwarf companion (defined here as a galaxy within its host virial radius that has a stellar mass $M_\star \gtrsim 10^4$ $M_\odot$ in `m11q`). The bottom panel of Figure 2.4 shows the subhalo occupation fraction: the cumulative number of luminous $M_\star \gtrsim 1{\times}10^4$ $M_\odot$ satellites at a given $V_{\rm max}$ divided by the cumulative number of dark + luminous subhalos at that $V_{\rm max}$. We have stacked the subhalos and companions of all hosts to achieve a more complete sample across all ranges of $V_{\rm max}$. To account for the different resolution in our runs, we only consider subhalos above the minimum $V_{\rm max}$ thresholds introduced in Table 2.2 for each run.

The occupation fraction for galaxies with $M_\star \gtrsim 1{\times}10^4$ $M_\odot$ quickly decreases from about unity for $V_{\rm max} \geq 20$ km/s to only a few percent at $V_{\rm max} \sim 5$ km/s. For reference, our prediction is that about half of the subhalos with $V_{\rm max} = 15$ km/s will host a luminous dwarf, the rest remaining dark or below the $M_\star = 10^4$ $M_\odot$ resolved in our runs. These variations are commonly referred to as 'stochasticity' in the galaxy formation model, as dark matter subhalos of comparable mass may vary their stellar content by several orders of magnitude, including remaining totally dark, and predicting the exact form of the occupation fraction as a function of $V_{\rm max}$ must consider many factors of the evolution of subhalos, such as their merger histories and accretion time, as well as external factors such as the onset and end of reionization and the form of the ionizing background.

Name	Time	j_x	j_y	j_z
LMC	t_{1p}	-0.97 ± 0.03	0.14 ± 0.07	-0.19 ± 0.10
	obs	-0.93 ± 0.06	-0.1 ± 0.03	-0.36 ± 0.03
SMC	t_{1p}	-0.92 ± 0.05	0.04 ± 0.10	0.35 ± 0.08
	obs	-0.87 ± 0.06	-0.4 ± 0.04	-0.27 ± 0.04
Carina	t_{1p}	-0.93 ± 0.12	0.25 ± 0.07	-0.04 ± 0.20
	obs	$-0.97^{+0.13}_{-0.14}$	0.17 ± 0.04	-0.19 ± 0.1
Fornax	t_{1p}	-0.92 ± 0.20	0.19 ± 0.11	0.20 ± 0.07
	obs	$-0.96^{+0.23}_{-0.22}$	$-0.17^{+0.13}_{-0.14}$	0.24 ± 0.07
Sculptor	t_{2p}	-0.94 ±0.06	-0.00 ± 0.41	0.04 ± 0.05
	obs	0.99 ± 0.01	$-0.03^{+0.08}_{-0.07}$	0.13 ± 0.01
Sagittarius	t_{1p}	-	-	-
	obs	0.05± 0.02	$-0.99^{+0.09}_{-0.08}$	$-0.13^{+0.08}_{-0.09}$
Ursa Minor	t_{1p}	-	-	-
	obs	-1.0 ± 0.08	-0.09 ± 0.07	-0.02 ± 0.06
Leo I	t_{1p}	-	-	-
	obs	$-0.5^{+0.4}_{-0.37}$	$-0.59^{+0.5}_{-0.48}$	$-0.64^{+0.36}_{-0.34}$
Sextans	t_{1p}	-	-	-
	obs	-0.39 ± 0.05	-0.58 ± 0.06	-0.71 ± 0.06
Leo II	t_{2p}	-0.92 ± 0.05	0.21 ± 0.21	-0.28 ± 0.15
	obs	$-0.13^{+2.26}_{-2.05}$	$0.97^{+2.24}_{-2.12}$	$0.22^{+0.88}_{-0.81}$
Bootes I	t_{1p}	-	-	-
	obs	$0.63^{+0.16}_{-0.15}$	0.71 ± 0.11	-0.31 ± 0.08
Draco	t_{1p}	-	-	-
	obs	$0.89^{+0.1}_{-0.09}$	0.36 ± 0.06	$-0.27^{+0.08}_{-0.09}$

Table 2.3: Normalized cartesian components of satellite galaxy orbital angular momenta, as predicted by S17 for the first pericentric passage of the LMC (labelled 't_{1p}') and observed angular momenta as calculated form GAIA proper motions, originally tabulated in [90] Table C.4 (labelled 'obs'). These new measurements show Carina and Fornax as being consistent with a co-infall scenario with the LMC using criteria for Magellanic Cloud system membership as defined in S17: $j_x < 0$ and $|j_x| > |j_y|, |j_z|$.

2.4.1 New proper motions from Gaia

From the observational side, determining the dwarf satellites associated to the LMC prior to infall into the MW is not straightforward. Since tidal stripping due to the MW potential has already begun, the material once associated to the LMC in the past does not necessarily cluster around it today. However, because the LMC is inferred to be most likely in its first pericenter passage [137], cosmological simulations suggest that the stripped material may still retain its phase-space coherence, opening an avenue to disentangle previous associations [232, 233, 57, 134]. This coherence means that all subhalos within the LMC at infall are therefore expected to be distributed on the sky following the projection of positions and velocities of the LMC's orbit. Note that final membership requires of a combination of position on the sky, galactocentric distance, and 3D velocity to be satisfied simultaneously.

This imposes strong constraints on the orbital poles expected for early companions of the LMC and can be used to single out possible associations. This criteria was used in [232] to conclude that, with the exception of the SMC, no other classical dwarf with available proper motions at that time was consistent with an LMC association. With the arrival of new Gaia DR2 data, proper motions are now available for many dwarfs in the MW, including classical and ultrafaint dwarfs (we assume the cutoff for ultrafaints to be a stellar mass of $M_\star < 10^5$ $M_\odot$, as in [33]). With the new 6D information, [138] confirmed a likely association for 4 ultrafaints: Car2, Car3, Hor1 and Hyd1. The authors suggest follow up measurements for the confirmation of Dra2 and Hyd2, which have incomplete proper motion information. On the other hand, several of the classical dwarfs have updated proper motion measurements and their membership needs to be re-evaluated.

We have repeated the analysis in [232, S11] but now using the Gaia DR2 proper motions presented in [90, H18]. In particular, for classical dwarfs satisfying the galactocentric distance, position on the sky, and radial velocity constraints, S11 lists predictions for the orbital angular momentum expected in case of association. Following S11, we use a Cartesian coordinate system centered on the Milky Way, with x in the sun-galactic center towards $l = 0°$, y towards $l = 90°$in the direction of Galactic rotation, and z coincident with the disk angular momentum, towards $b = 90°$. For completeness, we list in Table 2.3 the j_x, j_y and j_z (all normalized to $|\ \vec{j}\ |$) of all dwarfs included in H18 that were not part of the [138] analysis. Errors are propagated from the quoted errors in H18 based on our calculation of j_x, j_y and j_z. These calculated values are labelled 'obs' for each individual galaxy. However, of most relevance to this work are the dwarfs for which S11 had pre-determined possible association based on sky positions and radial velocity. For those cases, we also list the predicted angular momenta for the first pericentric passage ($t_{1\mathrm{p}}$). Note that Sculptor and Leo II become a possible association only on a second-pericentric passage according to S11 ($t_{2\mathrm{p}}$).

With the newest proper motions from Gaia, Carina and Fornax are also compatible with having been accreted as part of the LMC system ('obs' and t_{1p} are consistent with each other within 1 σ). With stellar masses of $3.8{\times}10^5$ $\mathrm{M}_\odot$and $2.0{\times}10^7$ $\mathrm{M}_\odot$, respectively, this newly confirmed pair of galaxies fills the classical dwarf scale ($10^5 \lesssim M_\star \lesssim 10^7$ $\mathrm{M}_\odot$) in the satellite mass function of the LMC, which was previously populated only by ultrafaint dwarfs (Car2, Car3, Hor1, Hyd1 aside from the from the relatively bright SMC with $M_\star \sim 4.6{\times}10^8$ $\mathrm{M}_\odot$).

[207] suggest the possibility of LMC co-infall for Carina and Fornax by constraining their projected 2D orbital poles to within 30°of that of the LMC. We expand on this claim by using a more

stringent criteria: matching angular momentum orientation with the one expected for and LMC-like debree at the same position on the sky of Carina and Fornax. Notice that the radial velocities for both dwarfs have been already found consistent with an LMC association in previous work [232, 233]. Also worth highlighting, the galactocentric distance of Carina is in good agreement with predictions of association whereas in the case of Fornax, the measured galactocentric distance ($\sim$ 140 kpc) places it beyond the $\sim$ 100 kpc preferred location of the debree [see for instance Fig.6 in 232]. The large distance of Fornax is more consistent with the scenario of a more massive infall halo mass for the LMC (whereas previous predictions were based on an LMC-analog with $\sim$ 10 times lower mass), which would allow for a more extended distribution of the associated material. This caveat is an important one to bear in mind, and invites further investigation.

Note that Ursa Minor seems to meet the criteria set forth by S17, ($j_x < 0$ and $|j_x| >> |j_y|, |j_z|$). However, its nearly perfect radial orbit ($j_x = -1$, $j_y \approx j_z \approx 0$) as well as its position in a completely distinct region of the sky than predicted for LMC debris (and where all currently known LMC satellites reside; see S17 Figure 1) suggest a non-Magellanic origin for Ursa Minor.

We summarize in Table A.1 a complete list of MW dwarfs with their current understanding of association to the LMC. The rightmost columns labelled 'possible' (if follow up is needed) and 'confirmed' (if enough information exists to make the claim) with the relevant references. The previously confirmed satellites of the LMC (by S17 and K18) include Car2, Car3, Hor1, Hyd1 and the SMC. No label means that a given galaxy is unlikely to be associated with the LMC given the current data. Galaxies confirmed by our calculations using Gaia DR2 are labelled 'this work'.

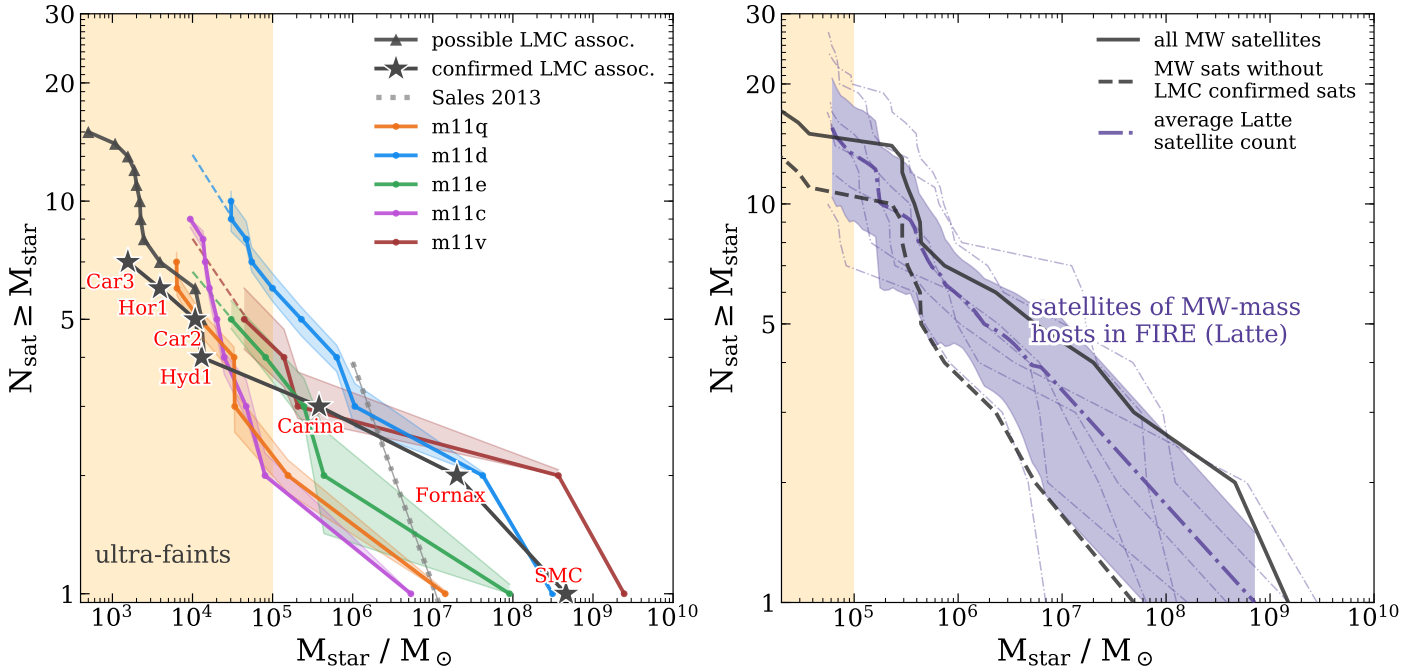

Figure 2.5: Cumulative $z = 0$ count of satellite galaxies above a given stellar mass within one virial radius of the host. (Left) The satellite stellar mass functions of LMC-mass hosts in FIRE (colored) and the real LMC (dark grey). Shaded regions show the 1σ variance from over the last ~1.3 Gyr. Confirmed LMC satellites are named in red and shown as star markers, while possible LMC satellites are cumulative with the confirmed population and shown as triangles. 'Confirmed LMC assoc.' refers to dwarf galaxies with full proper motion measurements which have angular momenta in agreement with the LMC infall direction, while those labeled 'possible' have incomplete proper motion data, but existing data is consistent. The teal dotted line is the expected satellite mass function of an LMC-mass host as predicted by semi-analytic modelling in [234], which uses the model in [114]. All error bars are Poisson noise. (Right) The solid grey line represents all satellite galaxies of the MW, while the dashed grey line represents the same satellites of the MW minus the confirmed satellites of the LMC, which are shown in the left panel and listed in Table 2.2. This shows what the in-situ satellite population of the MW was prior to the infall of the LMC and its associated companions. The purple shaded region represents the range of satellite mass functions of these MW-mass hosts in FIRE, with thin lines representing each individual host, and thick line indicating the average number of luminous satellites at each mass. The yellow vertical shaded region on the left represent the ultrafaint mass scale.

2.4.2 Simulated LMC Satellite Populations

With new observational context to the number of dwarf galaxies consistent with co-evolution and co-infall with the LMC, we can examine these results in a cosmological context. We provide this context by analyzing the satellite population of ΛCDM cosmological zoom-in simulations of isolated LMC-mass hosts. The left panel in Fig. 2.5 shows the stellar mass function of LMC satellites in FIRE (colored lines refer to the same simulations as previous figures, with the dashed lines representing an extrapolation to $M_\star \sim 10^4$ $M_\odot$ for the runs with resolution $m_{\rm bary}$ = 7070 $M_\odot$). In dark gray we show the observed stellar mass function of LMC satellties inferred from the kinematics of MW dwarfs from Gaia DR2 data, using starred symbols for the confirmed associations (SMC, Carina, Fornax, Hyd1, Car2, Hor1, and Car3) and in triangles including all 'possible' associations to the LMC, as determined by S17 and K18.

We find an overall good agreement between the inferred satellite population of the LMC and our simulated analogs. Our simulations predict between 1 and 5 classical satellites of the LMC, in agreement with the observational estimate of 3 for the LMC (SMC, Carina, and Fornax). There is an interesting mass dependence on the ability to predict relatively massive satellites for an LMC-like host. Only the two highest mass FIRE hosts (`m11d` with $M_{\rm 200m}$=2.8×10^{11} $M_\odot$, and `m11v` with $M_{\rm 200m}$=2.9×10^{11} $M_\odot$) are able to reproduce the high-mass end of the LMC's satellite mass function, in very close agreement with the halo mass estimates of the LMC (~3×10^{11} $M_\odot$) from other methods based on abundance matching [12, 191] and circular velocity measurements [276]. In fact, the average halo mass of a LMC-SMC system in the EAGLE simulations is ~3×10^{11} $M_\odot$ [244, 42]. The remaining three centrals with halo mass ~ 1.5×10^{11} $M_\odot$, tend to have lower mass companions than the SMC. On the other hand, all runs have at least one satellite within a factor of

two the stellar mass of Fornax, supporting its association to the LMC as suggested by the newly released Gaia kinematics.

One should keep in mind that the LMC-SMC association itself is rather unusual. Previous work on LMC-SMC selected pairs have showed them to be rare, though not impossible [23, 263]. For example, [19] used Illustris and SDSS to predict that the number of companions with $M_\star \sim 2\times10^8$ $M_\odot$ per LMC-mass dwarf is roughly 0.02 once projection effects have been taken into account. It is unclear how this figure changes with host mass, but following our results on the trend with virial mass, the likelihood of such a companion should increase if the LMC halo is on the massive end of the $1-3\times10^{11}$ $M_\odot$ range[6]. In general, the number of classical dwarfs in our FIRE centrals is in good agreement with earlier predictions from semi-analytical calculations in [234, light-blue dotted line] taken from the Millennium-II simulations [26]. However, the overall slope on the massive end of the FIRE runs is shallower than that in [234], probably a result of a slightly different stellar mass - halo mass relation for low mass dwarfs in the semi-analytical catalog than in our hydrodynamical runs.

For the ultrafaint regime, our two highest resolution runs, `m11q` and `m11c`, predict $5-8$ companions with $M_\star \geq 10^4$ $M_\odot$, which is in good agreement with the 5 inferred for the LMC from proper motion observations of MW dwarfs [138]. In general, if extrapolating the medium resolution runs to $M_\star \geq 10^4$ $M_\odot$ (which, according to the highest resolution runs, would be a reasonable approach) the predicted number of satellites above this stellar mass may be as high as 11 for `m11d`. Although such predictions should be taken with caution given the low number statistics and numerical resolution, the assumption that some of the LMC ultrafaint companions still await

[6] `m11v` was specifically selected to be a multimerger, and thus cannot aid a discussion of the cosmological frequency of large satellites

discovery is a reasonable one. In particular some of the brighter 'possible' associations already identified, Hyd2 with $M_\star \sim 1.4{\times}10^4$ $M_\odot$ and Dra2 with $M_\star \sim 2.5{\times}10^3$ $M_\odot$, might deserve a closer follow up to confirm or rule out their Magellanic origin.

Furthermore, our estimates for the number of ultra-faint companions can be regarded as lower limits, because of the implemented model for cosmic-ray heating in the ISM (in addition to the assumed UV background), which in these FIRE simulations induces too much heating in gas at early times ($z \gtrsim 10$) [98]. This effect has been explicitly tested with no observed impact on the population of classical dwarfs, however, the additional heating may in fact *decrease* the number of predicted ultrafaints compared to a method resulting in later reionization [for details, see 98, Section 3.3 and Appendix B]. As such, our estimates are effectively a conservative lower limit and indicate that several yet-to-be-discovered companions to the LMC may yet exist.

Lastly, on the right panel of Fig. 2.5 we show the observed stellar mass function of MW satellites (black solid) along with satellites of M31 (black dot dashed). If the LMC brought along several of the dwarfs as estimated from the previous calculations (gray starred symbols), the MW satellite mass function must have looked rather different about 1 Gyr ago right before the infall of the LMC.[7] This is shown as the gray dashed line, computed as the total MW satellites but subtracting the confirmed LMC associations. As usual, we define satellites as those within $r_{200\mathrm{m}}$ of the host. In such case, the MW halo may have hosted a significantly lower number of dwarfs than now, although still in reasonable agreement with the predicted satellite population of Latte galaxies ($M_{200\mathrm{m}} \sim 10^{12}$ $M_\odot$, shaded in purple). The similarity between the high-mass end of the satellite mass function for the MW and the LMC argues once again for a rather massive pre-infall LMC halo, likely $\sim 3 \times 10^{11}$

[7] However, exact counts of luminous satellites are subject to change over this timescale as they are disrupted into streams, e.g. Sagittarius.

$M_\odot$ and above, predicting several undiscovered ultra-faint dwarfs that were previously associated to the LMC.

2.4.3 The Predicted Dark Matter Content of LMC Satellites

Besides the number of dwarf galaxies expected around Magellanic-like systems, a further (arguably stronger) test for ΛCDM galaxy formation models is to reproduce the internal kinematics of the stars that are measured from observations. In the case of ultrafaint dwarfs, reported velocities from observations cover mostly the radius range $r < 200$ pc; with at least half of the systems having measured velocities within 50 pc [247]. Unfortunately, integrated quantities such as circular velocities are not yet converged in our simulations at such extreme small radii (typical gravitational softening $\epsilon_{\rm DM} \sim 20 - 40$ pc for all runs). We therefore analyze kinematic profiles of simulated classical dwarfs, but present a study of $V_{\rm max}$ that can guide the conclusions in the ultrafaint regime.

Fig. 2.6 shows the circular velocity profiles of all simulated classical satellites ($M_\star > 10^5$ $M_\odot$) of our FIRE LMC-analogs. Lines are dashed below the dark matter convergence radius for each resolution as listed in [127]. Individual curves are color coded according to the stellar mass content of each satellite, as indicated by the color bar. The simulation data hints to a correlation where the larger $M_\star$ dwarfs will populate larger circular velocity subhalos, at least in the regime of classical dwarfs.

Observed dwarf spheroidals are also plotted as single points assuming $V_{\rm circ}(r_{1/2}) = \sqrt{3\langle\sigma_{\rm los}\rangle}$ with $\sigma_{\rm los}$ the observed line-of-sight stellar velocity on the y-axis and the half-light radii $r_{1/2}$ on the x-axis (following [24]). Sources for the observed $\sigma_{v,*}$ are listed in the legend of Fig. 2.6. Observed galaxies presumably associated with the LMC are shown in red while other MW dwarfs are plotted

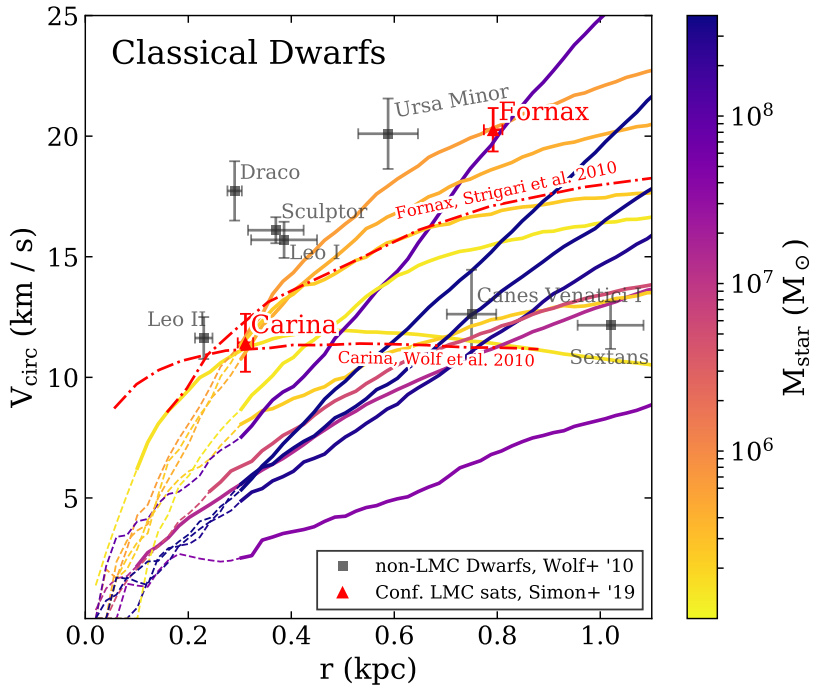

Figure 2.6: Circular velocity profiles ($V_{\rm circ}$=$\sqrt{GM(<r)/r}$) of all `m11` satellites in FIRE. Due to resolution, only satellites with $M_\star$ above (below) $1{\times}10^5$ $M_\odot$ are shown, colored according to $M_\star$. All individual points are observed half-light radii (*x-axis)* versus $V_{\rm circ}(r_{1/2}) = \sqrt{3\langle\sigma^2_{\rm los}\rangle}$ as described in [24]. Grey points (taken from [300]) are various MW dwarfs that do not belong to the LMC-system, while those dwarf galaxies presumably associated with the LMC are painted in red. The two red lines are circular velocities for Carina and Fornax as determined by [265] and [300], noted accordingly. The dark matter content of our predicted classical satellites is in good agreement with the newly deemed members, Carina and Fornax.

in gray. For completeness, we also include the full circular velocity profiles as a function of radius for Carina and Fornax from [300] and [265], respectively.

The predicted mass content for the brightest satellites of LMC-mass hosts, such as Carina and Fornax, are consistent with the observational values, supporting the possible association to the LMC inferred from their proper motions. It is important to highlight that the simulated curves in Fig. 2.6 are, if anything, lower limits to the true density of simulated dwarfs, as a smaller softening

and increased resolution would result in higher inner velocities,[8] which would still accommodate the observed values. The good agreement with observations of Carina and Fornax is therefore encouraging and highly suggestive of a possible membership to the LMC group.

For the ultrafaint regime, we turn our analysis to maximum circular velocities, as we expect them to be well converged. Following Eq. 10 in [256], the correction due to numerical effects is at most ~0.1 km/s, or $\lesssim$1%. Interestingly, a closer inspection of our simulations reveals that tidal stripping is likely to play a major role on the present-day dark matter content of LMC companions, particularly in the ultrafaint regime. This is clearly seen in Fig. 2.7, which shows a comparison between peak maximum circular velocity achieved throughout a subhalo's history ($V_{\rm peak}$) as a function of the circular velocity measured at present day ($V_{\rm max}(z = 0)$) for all subhalos in our sample of LMC-mass hosts in FIRE. Dark subhalos are indicated with gray dots, while large squares and triangles highlight the location of classical and ultrafaint simulated dwarfs, respectively. The symbols are color coded by lookback time since accretion (lower values are more recent infalls), and confirm that some of the surviving ultrafaint satellites in an LMC-system may have been accreted as early as 12 Gyr ago. The two regions of dark and light shaded gray indicate factors of 2 and 10 decrease in circular velocity.

As indicated by Fig. 2.7, the ultrafaint LMC companions are narrowly distributed at $V_{\rm peak}$ $\sim$ 20 km/s at infall but show a large spread in $V_{\rm circ}$ today, 6 $-$ 20 km/s. We find the present-day median $V_{\rm max}$ for ultrafaint LMCs to be 14.4 km/s. As expected, the latest ones to infall remain close to the 1-to-1 line, as tidal disruption has not had sufficient time to affect their properties. We find that he amount of tidal stripping experienced is not dependent on stellar mass. However, consider (i) the narrow range of $V_{\rm peak}$ predicted for ultrafaints, and (ii) their low stellar masses, at which

[8] We have tested this explicitly, see Fig. A.2. Also see [256] for an evaluation of softening effects on $V_{\rm circ}$.

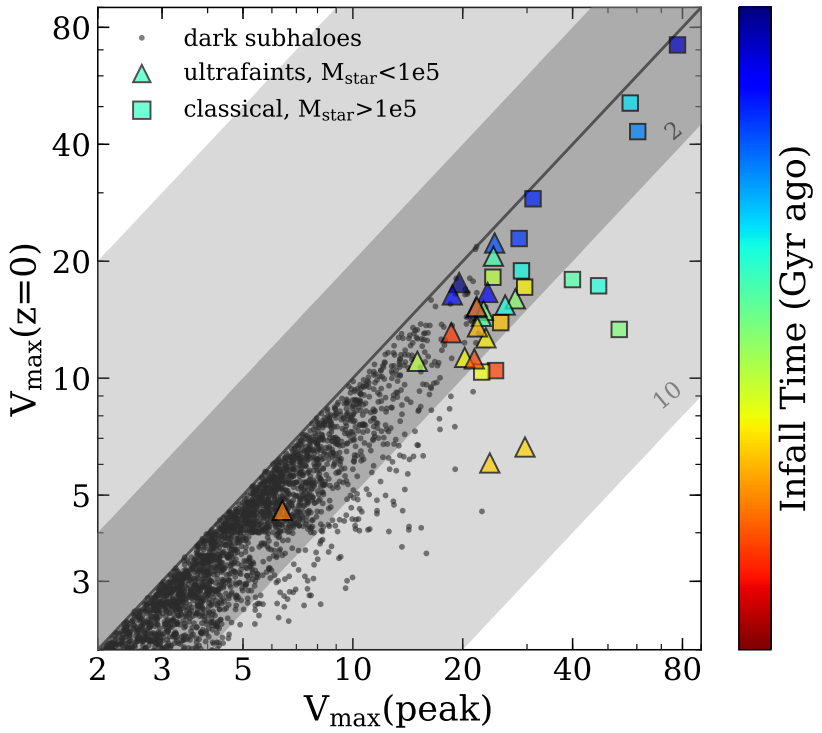

Figure 2.7: The peak $V_{\rm max}$ ever obtained by the subhalo versus its present-day $V_{\rm max}$. Squares represent subhalos which host galaxies of $M_\star \geq 10^5$ M$_\odot$, triangles host those with $M_\star \leq 10^5$ M$_\odot$, and grey dots are dark subhalos. The color bar shows the time in Gyr since a given satellite's infall to the host LMC-mass central. As expected, satellites with recent infall times ($T_{\rm inf} \lesssim 4$ Gyr) show minimal deviation from $V_{\rm peak}$. However, tidal disruption within LMC-mass systems for earlier infalling satellites may cause a factor of $\sim 2-7$ reduction in the $V_{\rm max}$ of ultrafaints at $z = 0$.

feedback is not expected to affect the inner DM distribution. Both effects combined establish an interesting correlation in ultrafaints that might be used to assess their likelihood of association to the LMC. We emphasize that low central densities are a necessary rather than sufficient condition to determine an association to the LMC since an early infall onto the MW for ultrafaints will also induce tidal stripping and associated lower inner densities. Determining which host a satellite was first associated with is a task left to orbital phase-space analysis, as in sub-section 2.4.1.

Although tidal stripping proceeds mostly outside-in, subhalos that are affected by tides also register a drop in their inner dark matter content [e.g., 117, 29]. It is therefore expected that

ultrafaint satellites of the LMC might show lower inner velocities than objects of similar mass that were accreted more recently into the MW. This prospect is interesting since Gaia DR2 data suggests that several of the ultrafaint galaxies are likely on their first infall onto the MW [246]. Identifying ultrafaint dwarfs with orbital properties consistent with that of the LMC and that simultaneously show the lowest inner densities may help to constrain the most likely LMC group members[9]. From that perspective, the likely associations for Hyd1 with $V_{\rm circ}$ = 4.7 km/s and Car2 with $V_{\rm circ}$ = 5.9 km/s, both within $r \leq 100$ pc, or the possibly associated Hyd2 with $V_{\rm circ}$ = 6.2 km/s, seem favored compared to the more dense Car3, Hor1, or Dra2 with $V_{\rm circ} \geq 8$ km/s at $r \sim 50$ pc [data from 247]. However, higher resolution simulations as well as more accurate observations are needed in order to make more definitive claims.

2.5 Summary and Conclusions

We used five ΛCDM cosmological zoom in simulations of LMC-mass hosts ($M_{\rm 200m}$ = $1 - 3 \times 10^{11}$ $M_\odot$) in FIRE to examine both the dark and luminous substructure of such galaxies, against which we compare to the Latte suite of seven simulations of MW-mass hosts. We summarize our primary findings here, and discuss our conclusions in the following paragraphs.

1. By comparing dark matter only to hydrodynamic baryonic simulations, we show that suppression of dark matter substructure is less strong for LMC-mass hosts than for MW-mass hosts, since this suppression is caused by tidal interactions with the central baryonic galaxy [97]. We therefore expect that LMC-mass galaxies are promising laboratories for subhalo detection.

[9]Note that the MW environment may also be conducive to tidal stripping such that low inner densities may be a telling but not sufficient condition for association to the LMC.

2. We calculate orbital angular momenta for 10 observed MW-dwarfs using Gaia DR2 data [90] and show that Fornax and Carina are highly consistent with predictions for tidal debris of a simulated LMC-MW infall scenario from [233]. This brings the inferred satellite mass function of the LMC up to seven members, including the SMC and the four ultrafaints identified in [138].

3. We compare this to the simulated satellite mass function of our five LMC-mass hosts in FIRE and find excellent agreement on the bright end with our higher mass halos. Our simulations suggest that more ultrafaints are expected for a halo comparable to that of the LMC. In addition, the population of MW satellites pre-LMC infall remains consistent with simulated MW-mass hosts in FIRE.

4. We find that the tidal disruption of simulated LMC satellites, indicated by a reduction in their maximum circular velocities after infall, is an important effect, even at such host mass scales. We therefore expect that dwarfs associated with the LMC should have lowered densities, though this is not sufficient criteria for association by itself as tidal effects from the MW are also expected to affect nearby dwarfs.

We have shown that LMC-mass centrals suppress much less dark matter substructure compared to MW-mass centrals, with a particularly striking difference in suppression patterns for the inner 0.2 $r_{200\mathrm{m}}$ of the halo. There, we observe a factor of ~3.5 reduction (from dark matter only to baryonic runs) in the number of subhalos at V_{max} = 10 km/s in MW mass hosts versus a factor of ~1.4 for LMC mass hosts. This suppression of substructure is mainly due to tidal interactions with the central baryonic disk. We identify two features of the LMC-mass hosts in FIRE that explains this: (i) a much lower stellar mass to halo mass ratio than that of MW-mass objects and (ii) a significantly

shallower inner density profile (larger core). The first implies that the gravitational potential of the galaxy is less significant compared to that of the halo. The second implies that the shape of the potential is much smoother than that seen in DMO versions of similar halos and that seen in halos hosting larger central galaxies. This combination provides a friendlier environment in the baryonic runs of cored $M_{200\mathrm{m}} \sim 10^{11}$ M$_\odot$ halos, leading to less suppression of subhalos due to tidal disruption on these scales compared to the harsher effects reported for 10^{12} M$_\odot$ hosts [63, 97, 235].

We compare the simulated satellite population of the LMC-mass hosts to the set of observed MW dwarfs that is consistent with an LMC co-infall scenario. We present revised calculations following [232] and using updated Gaia DR2 proper motion for classical dwarfs ($M_\star \geq 10^5$ M$_\odot$) from [90]. We find that Carina and Fornax are now compatible with a common infall along with the LMC system, and are added to the previously suggested associations to the SMC and the group of ultrafaint candidates Car2, Car3, Hor1, and Hyd1 introduced in [138]. We find generally good agreement with the satellite population inferred for the real LMC. One of our halos, `m11d` with $M_{200\mathrm{m}} \sim 3 \times 10^{11}$ M$_\odot$, is able to accurately predict the mass distribution of the three largest LMC satellites: the SMC, Fornax, and Carina, providing theoretical support to the claims of association. Furthermore, the predicted circular velocities for LMC satellites in this mass range is in good agreement with measurements of Carina and Fornax.

For fainter satellites, the LMC-mass systems in FIRE host comparable to slightly more ultrafaint companions than observed with the real LMC. On average, 7 ± 2 satellites are predicted above $M_\star = 10^4$M$_\odot$, in reasonable agreement with the 5 above that mass limit presumed associated to the LMC (Car2, Hyd1, Carina, Fornax, and the SMC). We find that ultrafaint companions of the LMC are expected to have experienced significant tidal disruption within the LMC potential, as

measured by the decrease on the subhalo maximum circular velocities since infall. As such, lower dark matter inner densities together with their orbital parameters [138], may help identify those ultra faint dwarfs that infalled onto the MW as part of the LMC group.

In summary, if the SMC, Carina, and Fornax are former satellites of the LMC, this may favor a relatively massive dark matter halo mass for the LMC prior to infall onto the MW, $M_{200\mathrm{m}} \sim 3 \times 10^{11}$ $\mathrm{M}_{\odot}$. This would push the expected ultrafaint dwarf numbers to the upper end of our predicted range, suggesting that some LMC associations still await discovery. According to our simulations, the missing dwarfs will lie roughly $30 - 80$ kpc from the LMC at infall and have $M_{\star} \sim 10^4$ $\mathrm{M}_{\odot}$ and $V_{\mathrm{max}} \approx 15$ km/s. This implies a relatively low central dark matter density that can be used as an additional membership criteria to discern from other, more recent individual infalls onto the MW. Based on their partially known orbital parameters and their low velocity estimates, the most promising candidate is Hyd2. Follow up observations are needed to confirm or dismiss the association.

In addition to LMC, this work presents the first observational and testable predictions using hydrodynamical cosmological simulations for the satellite mass function of a Magellanic-mass system down to the ultrafaint regime (semi-analytic modelling has been used for similar predictions, e.g. [64, 21]). Similar to how the study of satellite population of MW-mass hosts pushed forward our understanding of galaxy formation and cosmology in the past, the large predicted number of isolated dwarfs combined with upcoming deep surveys and wide field-of-view instruments such as WFIRST, as well as searches for satellites of LMC-mass hosts beyond the MW [e.g. MADCASH; 41], may turn the study of dwarf-dwarf systems into a valuable and essential test of the ΛCDM model.

Chapter 3

The effects of LMC-mass environments on their dwarf satellite galaxies in the FIRE simulations

Characterizing the predicted environments of dwarf galaxies like the Large Magellanic Cloud (LMC) is becoming increasingly important as next generation surveys push sensitivity limits into this low-mass regime at cosmological distances. We study the environmental effects of LMC-mass halos ($M_{200m} \sim 10^{11}$ M$_\odot$) on their populations of satellites ($M_\star \geq 10^4$ M$_\odot$) using a suite of zoom-in simulations from the Feedback In Realistic Environments (FIRE) project. Our simulations predict significant hot coronas with $T \sim 10^5$ K and $M_{\rm gas} \sim 10^{9.5}$ M$_\odot$. We identify signatures of environmental quenching in dwarf satellite galaxies, particularly for satellites with intermediate mass ($M_\star = 10^{6-7}$ M$_\odot$). The gas content of such objects indicates ram-pressure as the likely quenching mechanism, sometimes aided by star formation feedback. Satellites of LMC-mass hosts replicate

the stellar mass dependence of the quiescent fraction found in satellites of MW mass hosts (i.e. that the quiescent fraction increases as stellar mass decreases). Satellites of LMC-mass hosts have a wider variety of quenching times when compared to the strongly bi-modal distribution of quenching times of nearby centrals. Finally, we identify significant tidal stellar structures around four of our six LMC-analogs, suggesting that stellar streams may be common. These tidal features originated from satellites on close orbits, extend to ~80 kpc from the central galaxy, and contain $\sim 10^{6-7}$ $M_\odot$ of stars.

3.1 Introduction

Environment – the relative proximity to higher mass structures – has been repeatedly shown to correlate with morphology, color, and star formation rate (SFR) in dwarf galaxies [8, 143, 7, 49, 167, 9, 287], though the majority of such surveys are limited to relatively massive environments and satellite galaxies with $M_\star \gtrsim 10^8$ $M_\odot$. Studies of LG and near-field dwarf galaxies have further corroborated this trend by demonstrating the dependence of HI abundance and star formation history (SFH) on environment [109, 108, 289]. More detailed studies of the LG have shown that a majority of satellite dwarf galaxies in the LG are quenched at stellar masses below 10^8 $M_\odot$ [291, 295], while field dwarfs remain star-forming [99, though this work is mostly limited to bright dwarf galaxies with $M_\star \gtrsim 10^7 M_\odot$]. In contrast to the universally high quenching fractions found around the LG, [178] showed via the Satellites of Galactic Analogs (SAGA) survey that MW-mass systems outside the LG may have systematically lower quenched fractions, even at lower masses. This suggests that the SFHs of LG satellites might not be typical of MW-mass hosts.

Plausible physical mechanisms for the quenching of star formation have been identified. Small-scale hydrodynamic effects are known to either remove gas from a star-forming galaxy via ram-pressure stripping [112, 1], prevent the infall of cold gas that fuels star formation leading to 'starvation' [160], and/or disrupt the structure of the galaxy during close interactions with other galaxies [190, 211].

Since dwarf galaxies have shallow potentials and massive hosts such as the MW are know to host hot gaseous halos [115], much attention has been given to the effects of ram-pressure stripping in low-mass satellites. For example, [86, 295] demonstrated a mass-dependent quenching model in which satellites with $M_\star = 10^{6-8}$ $M_\odot$ have short quenching time-scales consistent with ram-pressure stripping, while the longer quenching time-scales of higher mass satellites ($M_\star \gtrsim 10^8$ $M_\odot$) are consistent with starvation. [85] further showed that a clumpy gaseous halo with local densities $\sim 2-20$ times the mean gas density increases the efficacy of ram-pressure stripping and reproduces the high quenched fraction of MW satellites. This model breaks down at the lowest galaxy masses ($M_\star \lesssim 10^5$ $M_\odot$), where ram-pressure and starvation have been shown to be unable to reproduce the universally early quenching times [76, 227], thus pointing to heating from the ionizing UV background as the quenching mechanism at such scales.

While the quenching fraction of LG satellites is known to rise as satellite mass falls [289, 185, 295], high resolution studies of nearby satellites and simulated LG-like environments have enabled the characterization of the full star formation histories (SFHs) of dwarf galaxies, and the study of their dependence on both satellite mass and environment. [291] characterized a bimodal mass-dependence for quenched fraction, with the highest ($M_\star \sim 10^{11.5}$ $M_\odot$) and lowest ($M_\star < 10^5$ $M_\odot$) mass galaxies holding high quenched fractions, and galaxies with $M_\star = 10^{8-10}$ $M_\odot$ having the

lowest, suggesting this mass range may be the most difficult to quench. Comparing to infall time estimates from [225], they also find that higher mass satellites tend to quench $1-4$ Gyr after infall, while lower mass satellites quench prior to infall. [293] used FIRE-2 simulations [127] to reproduce properties of satellites around MW-like hosts, in particular, the wide scatter in SFHs and the stellar mass dependence thereof. [98] looked at a sample of ~ 500 dwarf galaxies from the FIRE suite to investigate the effect of various environments (LG vs MW vs centrals thereof vs highly isolated centrals), finding that LG and MW-like environments quench similarly, and form their stars earlier than dwarf centrals, supporting the host-satellite interaction model for quenching. They also find that higher mass dwarf galaxies are more likely to form a higher fraction of their stars at later times, in agreement with observed LG SFHs.

Other simulations of MW and LG-like environments, such as APOSTLE [60], Auriga [249] and NIHAO [31] have demonstrated consistent findings, particularly that satellites form earlier than centrals. Recently, [5] used the DC Justice League simulation suite to show that ram-pressure is the source of short quenching time-scales for satellites of intermediate mass ($M_\star = 10^{6-8}$ M$_\odot$), as well as the diversity of satellite SFHs and the trend of increasing quenched fraction with decreased $M_\star$.

While interactions with the host environment are known to affect satellite star formation, it can also affect morphology through gravitational interactions. Such interactions can be strong enough, depending on the satellite's physical size, proximity of the host, and the mass of the host, to produce observable stellar features known as tidal streams. Tidal streams around our Galaxy have been studied extensively, starting with the Sagittarius (Sgr) dSph tidal stream [129, 16], and with dynamical models of stream kinematics revealing multiple close encounters of satellites with

the MW [136, 176, 119, 208]. Such features have also been observationally identified in galaxies beyond the LG [e.g. 177, 183, 182]. Stellar streams give insight and evidence to the hierarchical nature of galaxy assembly. Given this hierarchical nature and the confirmation of a population of satellites around the LMC, tidal streams should presumably be detectable around galaxies of lower mass than the MW. A handful of tidal streams have indeed been discovered around dwarf galaxies [184, 39], but their cosmological frequency remains unknown.

Much of the literature on satellites and the interactions with their host environments is confined to the scale of the MW/LG. This is because our highest resolution observations of dwarf galaxies exist within this volume. As next-generation surveys such as DELVE [66] MADCASH [41] and LBT-SONG [54] come online, it will be important to characterize the environments of lower-mass systems. We aim to extend the analysis of previous works listed above to the scale of the Large Magellanic Cloud (LMC), about an order of magnitude smaller than the MW. For example, [40] recently discovered two ultrafaint dwarf satellites of LMC-mass hosts approximately 3 Mpc from the MW. Previous works have characterized properties of LMC analogs [44, 45, 72] or the predicted satellite population [134, 233, 138, 132, 207, 77, 237], but limited work has been done on characterizing the influence such environments have on observable properties of the satellite population, in particular their SFHs, quenched fractions, and tidal structures.

This paper is organized as follows: the simulations and sample are presented in Section 3.2; overall trends in satellite quenching are investigated in Section 3.3.1, while we investigate the environmental quenching of individual satellites in Section 3.3.3; tidal features around our LMC-mass hosts are presented in Section 3.4.

3.2 Simulations

We analyze six cosmological zoom-in simulations of isolated LMC-mass halos from the Feedback In Realistic Environments project[1] (FIRE). These runs used the FIRE-2 model [127] via the cosmological hydrodynamics code GIZMO[2] [121], a multi-method gravity plus hydrodynamics code, in its meshless finite-mass (MFM) mode. GIZMO implements an improved version of the Tree-PM solver from GADGET-2 [257] with fully-adaptive conservative gravitational force softenings for gas [217].

Simulations are initialized[3] with second-order Lagrangian perturbation theory at $z = 99$ using the MUSIC code [116] and evolved within a low-resolution cosmological box. The intended "zoom-in" [142, 198] volume is selected as a convex Lagrangian region containing all particles within $\sim 5\, r_{200\mathrm{m}}$ at $z = 0$ with no similar or higher mass halos as the primary, and is then reinitialized with higher resolution. This procedure is iterated until convergence at the intended resolution, with a buffer of low-resolution particles surrounding the main volume. The simulation is then evolved until $z = 0$. Since our hosts are isolated LMC-mass halos that are not embedded within the environment of the LG, small deviations in the assembly history and satellite population may be expected in comparison to the real LMC. However, the physical mechanisms explored here, in particular the environmental effects of LMC-mass hosts, are expected to apply in the case of the real LMC in addition to influence from its evolution in proximity to the LG environment.

[1] http://fire.northwestern.edu
[2] http://www.tapir.caltech.edu/~phopkins/Site/GIZMO.html
[3] http://www.tapir.caltech.edu/~phopkins/publicICs/

The FIRE-2 code calculates heating and cooling rates from $10 - 10^{10}$ K, using CLOUDY ionization states for free-free, photoionization & recombination, Compton scattering, photoelectric, metal-line, molecular, fine structure, dust collisional, uniform cosmic ray heating, against a spatially uniform, redshift-dependent UV background [80].

Star particles are formed in gas that is required to be locally self-gravitating, self-shielded, Jeans unstable, and with density $n_H > n_{\rm crit} = 1000\ {\rm cm}^{-3}$; inheriting mass and metallicity from their progenitor gas particles. To calculate stellar feedback, a [154] IMF is assumed in each star particle, with feedback quantities tabulated from the STARBUST99 stellar population model [163], including supernova Type Ia, II, and stellar winds, as detailed in [127] and [126]. Radiative feedback is modeled using the Locally Extincted Background Radiation in Optically-thin Networks (LEBRON), accounting for absorbed photon momentum, photo-ionization, and photo-electric heating.

Dark matter (DM) particles are assigned to halos and subhalos through 6+1 dimensional phase space analysis via the ROCKSTAR halo finder [14], which determines gravitationally bound particles and assigns mass through a spherical overdensity calculation relative to a threshold, such as the critical density density of the universe. Stellar properties are computed for each subhalo during an iterative post-processing procedure in with star particles within 80 per cent of a halo's radius and slower than $2\times V_{\rm max}$ with respect to the halo center are selected and refined until the stellar mass converges to < 1 per cent. More details on this process can be found in [235]. Progenitors of $z = 0$ halos are traced through time using `consistent-trees` [15] to construct merger trees. We use properties generated by the above methods to initially determine the stellar mass and star formation histories of dwarf galaxies, but we make further cuts on resolution as described below.

Simulation	$m_{\rm bary}$	$M_{\rm 200m}$	$M_\star$	$r_{\rm 200m}$	$r_{50\star}$	min. $M_\star$	$N_{\rm satellite}$	$N_{\rm central}$	Reference
	($M_\odot$)	($M_\odot$)	($M_\odot$)	(kpc)	(kpc)	($M_\odot$)			
m11c	2100	1.5e11	8.2e8	167.4	2.80	5.89e4	2	10	1
m11d	7070	2.8e11	4.1e9	203.9	6.75	2.29e5	6	1	2
m11e	7070	1.5e11	1.4e9	166.0	3.31	2.46e5	3	1	2
m11h	880	1.8e11	1.1e8	174.0	1.44	1.25e4	10	5	2
m11q	880	1.5e11	3.4e8	168.7	2.71	1.23e4	5	9	1
m11v	7070	2.9e11	2.4e9	210.5	2.61	1.39e5	4	5	1
						total	30	31	

Table 3.1: Properties of the host halo of all FIRE simulations analyzed. Column 1 is the name of each run; column 2 is the minimum baryonic particle mass; column 3 ($M_{\rm 200m}$) is the mass of DM contained within $r_{\rm 200m}$; column 4 ($M_\star$) is the stellar mass of the primary central of each zoom-in region; column 5 ($r_{\rm 200m}$) is the radius at which the mean interior DM density is equal to 200 times the average matter density of the universe; column 6 ($r_{50\star}$) is the half mass radius of stars in the primary central galaxy; column 7 (min $M_\star$) is minimum stellar mass of any object examined in each run (an effective resolution limit); column 8 is the number of satellites around the primary central; column 9 is the number of resolved galaxies outside $r_{\rm 200m}$ of the primary central; and column 10 is the reference in which the simulation was first presented. The total count for satellites and centrals analyzed herein is shown in the bottom row. Satellites are luminous (sub)-halos located within the host $r_{\rm 200m}$ at $z = 0$, while centrals are located outside the host halo. We make further resolution cuts on contamination by low-resolution particles ($M_{\rm lowres}/M_{\rm 200m} < 3$ per cent) and a minimum of 20 star particles formed within the progenitor halo of each object. Naturally, the runs with higher particle mass are less capable of resolving low-mass galaxies, leading to incompleteness of the faint end. Note that m11d, m11e, and m11v are unable to resolve ultrafaints ($M_\star < 10^5$ $M_\odot$) when applying our resolution criteria. References: [1] [127]; [2] [72]

3.2.1 Selecting the Sample

Table 3.1 lists the simulations used in our sample, including the resolution, the halo and stellar masses of the host galaxies, as well as the number of satellites and centrals identified within each simulation volume. Satellites are identified as being within $r_{200\mathrm{m}}$ of the main host halo at $z = 0$, where $r_{200\mathrm{m}}$ is defined as the radius within which the mean DM density is equal to 200 times the average matter density of the Universe. We classify centrals as any galaxy that falls outside $r_{200\mathrm{m}}$ but within the high-resolution region of each simulation. Well-resolved centrals are further selected as having a maximum contamination of low resolution particles at 3 per cent of their $z = 0$ halo mass. This cut is unnecessary for satellites, because they naturally fall within the high-resolution region.

To study the SFHs and to remove spuriously assigned particles, we track the location of star particles assigned to each (sub)halo and select only the ones which were formed within half of the halo's radius (of bound DM particles, as determined by `ROCKSTAR`). We place a minimum cutoff of 20 such star particles for each galaxy analyzed. In some cases, merger events led to large amounts of stars formed outside the halo being assigned at later times, but as these are physically meaningful associations, they were retained.

We have explicitly checked for splashback galaxies – those that entered $r_{200\mathrm{m}}$ of the primary central at some point, but exited at a later time – and find that all but one such objects are satellites at present day. Note that this is in contrast with the splashback population of MW-mass hosts, which tend to be significant outside of $r_{200\mathrm{m}}$ at $z = 0$ [230, 93, 83], an effect which is likely due to the difference in halo mass and infall rates of low-mass galaxies. The splashback process can potentially affect the evolution of the object and contaminate the sample of centrals, which are intended to

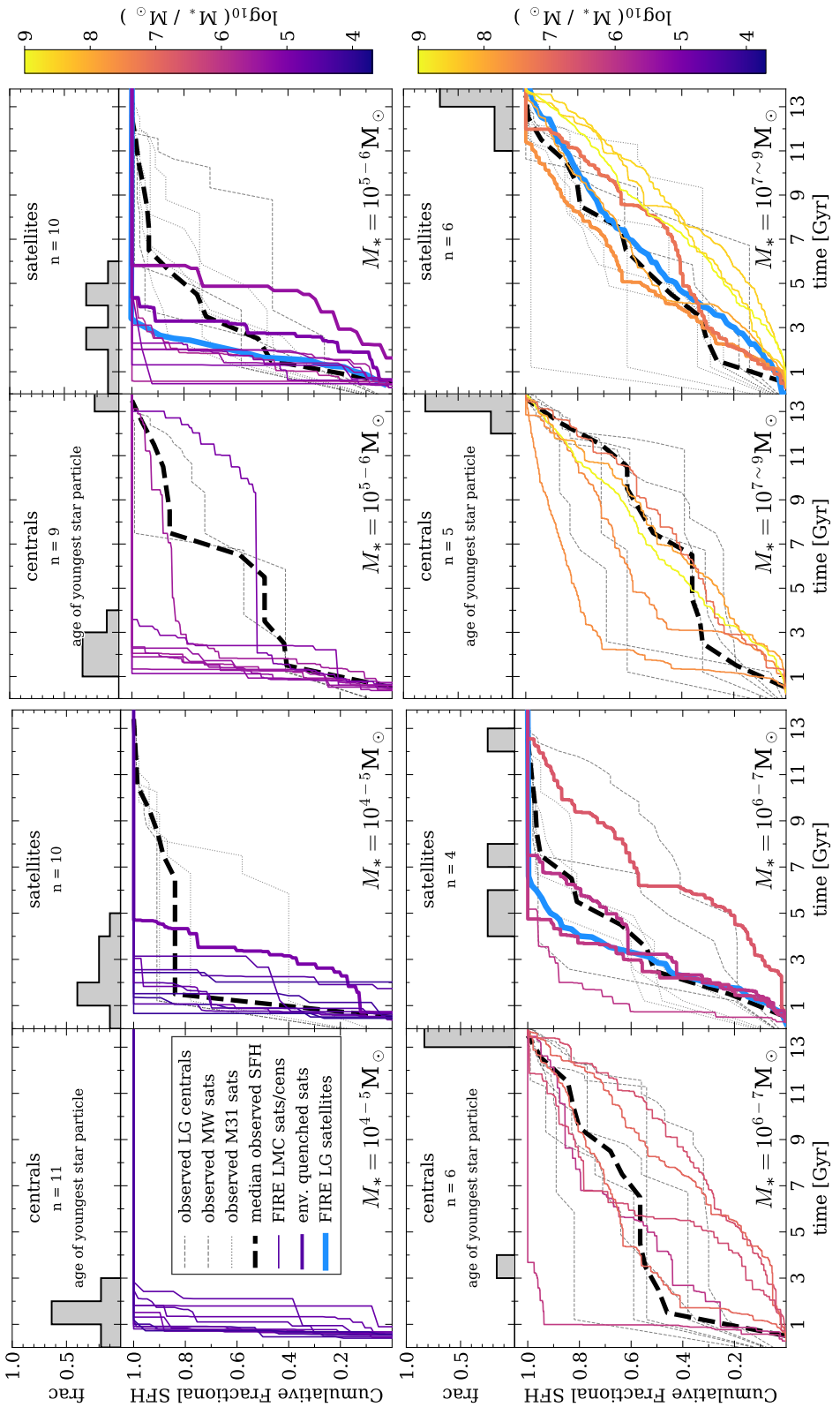
centrals
n = 11
age of youngest star particle
satellites
n = 10
centrals
n = 9
age of youngest star particle
satellites
n = 10
centrals
n = 6
age of youngest star particle
satellites
n = 4
centrals
n = 5
age of youngest star particle
satellites
n = 6
frac
Cumulative Fractional SFH
time [Gyr]
$M_* = 10^{4-5}$M$_\odot$
$M_* = 10^{5-6}$M$_\odot$
$M_* = 10^{6-7}$M$_\odot$
$M_* = 10^{7\sim9}$M$_\odot$
observed LG centrals
observed MW sats
observed M31 sats
median observed SFH
FIRE LMC sats/cens
env. quenched sats
FIRE LG satellites
log$_{10}$(M$_*$ / M$_\odot$)

Figure 3.1: Star formation histories (SFHs) of simulated LMC satellites (right sub-panels) and centrals (left sub-panels), colored and separated according to stellar mass. Satellites identified as being environmentally quenched (see Section 3.3.3) have been highlighted with thicker line styles. All colored lines are simulated data, while black/grey lines are observational data. Note that all observed data is for Local Group (LG) satellites/centrals. Individual observed SFHs of satellites of the MW/M31 [290, 250] are shown as faint dashed lines (style according to legend), with medians in each bin shown as thicker dashed black lines. Blue lines represent the median SFHs of satellites of LG-like hosts simulated using the FIRE-2 code, and as presented in [98] (see Table 1 therein for more information, including resolution). Histograms on the top of each panel represent the formation time of the youngest star particle for simulated LMC satellites or nearby centrals (i.e. they do not include observed satellites of the MW/M31, nor simulated FIRE satellites of LG-like hosts). The majority of centrals are quenched prior to $t = 4$ Gyr if they are not presently star-forming. Satellites, however, are more prone to influence by the environment of their LMC-mass hosts, and exhibit a greater diversity of quenching times. Overall, the SFHs of LMC satellites do not differ substantially from the SFHs of LG satellites. This is perhaps a counter-intuitive result given the reduced stellar mass to halo mass ratio of LMC-mass halos, and their less disruptive nature [132].

represent the evolution of similarly-massed galaxies in FIRE that are not affected by the host (or at least affected to a substantially smaller degree). The individual splashback central is a low-mass galaxy ($M_\star \approx 3\times10^5$ M$_\odot$) that was quenched at $t \approx 1.2$ Gyr while it was $\sim$1000 kpc from the central, first entering the primary halo at $t \approx 11$ Gyr, suggesting that its quenching was not environmentally induced. Our entire population of centrals is therefore unlikely to have been directly influenced by the environment of the primary LMC-mass halo.

We note that the following predictions are limited by both resolution and sample size. Only three of the runs are able to resolve galaxies with $M_\star < 10^5$ M$_\odot$, leading to a limited variety of cosmological volumes being sampled at this mass scale. Indeed, at all resolved scales, six zoom-in hosts is not a sufficient sample size to make statistically robust predictions, especially due to the relatively small number of predicted satellites of LMC-mass halos compared to that found around MW/LG-mass hosts. We consider this to be a case study in the formation of LMC satellites, rather than a statistically complete cosmological prediction.

3.3 Satellite Quenching

3.3.1 Comparison to Centrals

Figure 3.2.1 shows the SFHs of dwarf galaxies separated by association (satellites of an LMC mass host versus nearby centrals) as well as separated by stellar mass bins. All simulated data is shown as solid lines, while observed data for satellites of the MW/M31 is shown via dashed lines (these objects are shown for comparison, and are not direct analogs of our simulated satellites of LMC-mass hosts). We highlight LMC-satellites that have been identified as environmentally quenched (see Section 3.3.3) in a thicker line. In this subsection, we examine only the objects from our sample of LMC-mass hosts, with individual SFHs shown as solid colored lines. Satellites are defined as being located within its host virial radius at $z = 0$, while centrals are defined as being located outside this radius at $z = 0$ but within the high-resolution region of the simulated zoom-in volume. We combine the $M_\star = 10^{7-8}$ $M_\odot$ and $M_\star = 10^{8-9}$ $M_\odot$ bins due to the low number count, late quenching times, and general similarity of SFHs of galaxies in these bins.

In every mass bin, satellites (right panels) exhibit a wider range in quenching times than do centrals (left panels). We find that all ultrafaint (UF; $M_\star \approx 10^{4-5}$ $M_\odot$) galaxies quench early on, as expected from the heating effects of the ionizing UV background, preventing the accretion and subsequent cooling of gas in low-mass halos. The FIRE-2 simulations implement a spatially uniform UV background, so such effects would not be due to patchy reionization [127]. The latest forming UF satellite ($t_{\rm quench}\sim$ 4.6 Gyr) has been identified as environmentally quenched, and inhabiting a more massive halo than other satellites (when comparing the highest mass ever achieved by each halo to account for mass loss due to tidal stripping). This galaxy would have likely continued forming stars and be included in a higher mass bin if star formation were not shut off due to environmental

effects. Excluding this object, we find that UF satellites quench at $t = 2.0 \pm 0.8$ Gyr, and centrals quench at $t = 1.3 \pm 0.6$ Gyr, using the age of the last star particle formed as quenching time. When looking at the 90 per cent star formation time-scale, we find that satellites (again excluding those that are environmentally quenched) have $\tau_{90} = 1.8 \pm 0.7$, and centrals have $\tau_{90} = 1.3 \pm 0.5$. We therefore find the distribution in quenching times between UF satellites and centrals to be statistically indistinguishable. We also note that UF dwarf galaxies are only present in the three highest resolution runs: `m11c`, `m11h`, and `m11q`.

In the next mass bin, we find that satellites with $M_\star = 10^{5-6}$ M$_\odot$ also exhibit a wider range of quenching times than their predominantly early-quenched central counterparts. Notably, there are two late-quenching centrals, which formed stars until $t \approx 13$ Gyr. These galaxies inhabit somewhat larger DM halos ($M_{200\mathrm{m}} \approx 5.5 \times 10^9$ M$_\odot$) than most other galaxies in this stellar mass range, with the average halo mass excluded these two objects being $M_{200\mathrm{m}} \approx 2 \times 10^9$ M$_\odot$. This difference might seem small, but leads to a factor of 2 difference in their virial temperatures (4.6×10^4K versus 2.3×10^4K), increasing the temperature limit of gas that will remain bound to the halos during heating due to reionization and star formation feedback. The latest forming satellites in this mass bin, as in the previous, were identified as environmentally quenched and as possessing more massive DM halos than the rest of the satellites in this bin. Therefore, these objects are more consistent with failed versions of centrals in the next stellar mass bin.

Moving up in stellar mass to $M_\star = 10^{6-7}$ M$_\odot$, we now find that the majority of centrals are star-forming (the exception again being an outlier in halo mass, this time much lower than average), while all satellites are quenched at various intermediate times, $t_{\mathrm{quench}} \approx 4.5 - 12.5$ Gyr. *This is a*

strong indication that the environment of LMC-mass hosts is able to quench star formation in its dwarf companions.

In contrast, the highest mass dwarf satellites ($M_\star = 10^{7\sim9}$ M$_\odot$) form universally late, with all centrals and four of six satellites remaining star-forming at $z - 0$. The two quenched satellites ceased forming stars at $t \approx 11 - 12$ Gyr, and have stellar masses of $M_\star = 10^{7-8}$ M$_\odot$. All galaxies with $M_\star > 10^8$M$_\odot$ are star-forming, regardless of environment, further supporting the claim that such galaxies are the most resilient to quenching [298, 291, 295, 86].

Figure 3.2 shows the histogram of quenching times for all satellites and centrals. We define star-forming galaxies as those which have formed at least one star particle in the last ~ 500 Myr, while quenched galaxies did not form any star particles in the same time interval. Quenching times for such objects are defined as the formation time of their youngest associated star particle. We include the count of star-forming galaxies in the $t = 14 - 15$ Gyr bin to differentiate this population from those that formed their last star particle between $t = 13 - 13.2$ Gyr. We find that centrals demonstrate strongly bi-modal quenching behavior, either halting their star formation by $t = 4$ Gyr, or continuing until $z = 0$. In contrast, satellites exhibit a wider variety of quenching times, with 8 having clear signs of environmental quenching (highlighted in yellow). These galaxies were selected with 4 Gyr $< t_{\rm quench} <$ 13.2 Gyr, and $d_{\rm host}(t = t_{\rm quench}) < 2r_{\rm 200m}(t)$. That is, they are selected as having quenched late enough that reionization heating is unlikely to be the culprit, and close enough to their host halo to be influenced by its circum-galactic medium (CGM). We investigate these objects further in Section 3.3.3.

In summary, we predict that isolated LMC-mass galaxies should host a population of mostly quenched low-mass dwarf galaxies. More specifically, these galaxies should be host to $\gtrsim 3$

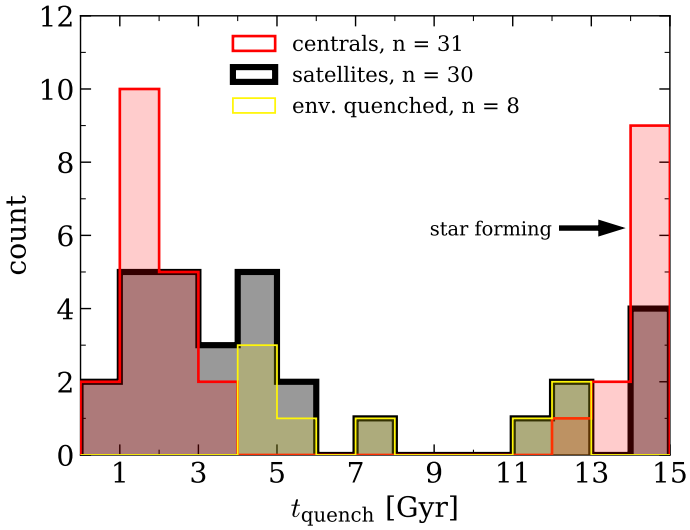

Figure 3.2: Histogram of quenching times for all centrals and $z = 0$ satellites of LMC-mass hosts. Here, we define $t_{\rm quench}$ as the formation time of the youngest star particle associated with the galaxy. Environmentally quenched satellites are highlighted in yellow and selected as having 4 Gyr $< t_{\rm quench} <$ 13.2 Gyr, as well as quenched within twice the virial radius of their host. To distinguish galaxies that were recently quenched from those that are actively star-forming, we have placed galaxies that formed a star particle within the last 500 Myr in the 14 – 15 Gyr bin, labeled as 'star forming.' While both centrals and satellites follow bimodal distributions, centrals exhibit clearly defined peaks and low scatter, while satellites exhibit a wider distribution. This indicates that the environments of LMC-mass hosts are the source of additional quenching mechanism(s), which we investigate in Section 3.3.3.

ultrafaint ($M_\star = 10^{4-5}$ M$_\odot$) satellites with ancient stellar populations, 1 – 4 intermediate mass ($M_\star = 10^{5-7.5}$ M$_\odot$) dwarf satellites with a variety of quenching times, some of which may have been environmentally quenched by the host, and lastly, one bright star-forming companion of $M_\star \gtrsim 10^{7.5}$ M$_\odot$, though not all simulations contain such an object. The number and mass distribution is in agreement with recent predictions of the LMC satellite population [134, 233, 138, 207, 132, 77].

3.3.2 Comparison to Local Group Environments

We find that satellites of LMC-mass hosts quench their satellites similarly to the LG, with simulated data from the FIRE simulations for such objects from Figure 4 of [98] shown as the blue

line in the right panel for each mass bin of Figure 3.2.1 (where $M_\star = 10^{4-5}$ $M_\odot$ is not included due to resolution limits). These simulations of LG-like environments include two MW-mass ($\sim 10^{12}$ $M_\odot$) halos, and satellites are defined as being with 300 kpc of one of those MW-like halos. For our $M_\star = 10^{7-9}$ $M_\odot$ bin, we show the mean reported SFH for the bins $M_\star = 10^{7-8}$ $M_\odot$ and $M_\star = 10^{8-9}$ $M_\odot$. In each mass bin where simulated LG-satellites are available, the overall shape of SFHs for such objects are consistent with LMC satellites.

We also compare to observed SFHs for satellites of the MW or M31 [290, 250], with individual SFHs in each mass bin shown as thin dashed/dotted lines, while the median is shown as a thicker black dashed line. We find that our simulated LMC satellites have SFHs that are broadly consistent with observed MW/M31 satellites at fixed stellar mass, especially in the two highest mass bins. The observed galaxies in the lowest bins tend to form later than their simulated counterparts. This is perhaps due to observational uncertainty, since the majority of stars in each observed galaxy are formed in early times, consistent with our simulated galaxies. Constraining the exact time of quenching can be a challenge with observational data. For example, see [291] for a discussion of the impact of blue straggler stars on the estimation of SFHs via color-magnitude diagram fitting.

The similarity of SFHs between observed & simulated LG/MW/M31 satellites and our simulated LMC satellites suggests that quenching of satellites may not be restricted to high-mass systems, and that dwarf-dwarf quenching could proceed likewise to quenching in LG-type environments, an effect that may be impactful on the interpretation of future observational missions categorizing satellites of LMC-mass hosts. There is evidence that the CGM of the MW is dense and structured enough to affect the evolution of its intermediate-mass dwarf satellites [e.g. 108, 212, 194].

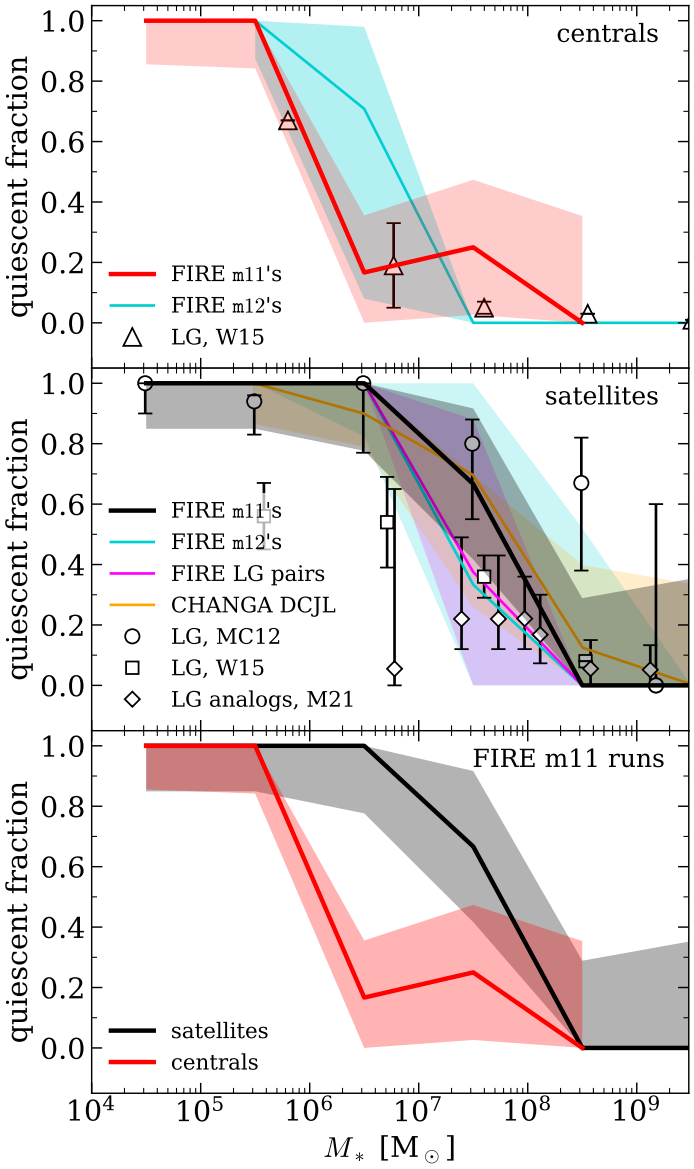

Figure 3.3: Stellar mass versus quiescent fraction in our simulations of LMC-mass hosts versus observed (points) LG galaxies and simulated (shaded regions) LG or MW-like halos. MC12 [185] and W15 [291] report data for the LG itself, while M21 [178] report data for observed MW analogs. We define the quiescent fraction as the number of galaxies in each mass bin that have $t_{\rm quench} < 13.2$ Gyr (that is, selecting all galaxies that have not formed a star particle within the last 500 Myr) to allow for variations that may arise from finite time-steps and star particle mass limits. We find that LMC-mass hosts are able to quench their satellite population to nearly the same degree as MW or LG-like hosts, perhaps a surprising result given their significantly smaller halo masses and baryonic content. References: FIRE MW+LG - Samuel et al. *in prep*; CHANGA - [5]; MC12 - [185] (as compiled by [295]); W15 - [291]; M21 - [178]

The apparent similarity in SFHs between Local Group and LMC satellites suggests this may be true of LMC-like environments as well.

Figure 3.3 shows the quiescent fraction (i.e., the portion of galaxies which have not formed a star particle within the last 500 Myr) versus stellar mass of LMC satellites and centrals along with additional observed and simulated LG satellites. Due to the fact that not all of our simulated LMC-mass systems contain satellites in each mass bin, our error bars are derived from Poisson scatter. Error bars on W15 were calculated from the difference in reported quenching fractions when considering morphological dTrans galaxies as either star-forming or quiescent.

Largely, our population of LMC satellites quenches similarly to LG satellites. Consistent with observations of satellites within the LG [185, 295] as well as with simulated MW/LG satellites [in FIRE-2 – Samuel et al. *in prep*; and CHANGA – 5], we find that LMC satellites with $M_\star < 10^7$ $M_\odot$ are universally quenched, and satellites with $M_\star \gtrsim 10^8$ $M_\odot$ are predominantly star-forming. This is also in agreement with semi-analytical models of the LG population [85, 84]. The interim region of 10^7 $M_\odot < M_\star < 10^8$ $M_\odot$ consists of satellites that are either presently star-forming or quenched within the last ~2 Gyr. In contrast, we find that 90 per cent of nearby centrals are quenched below $M_\star < 10^6$ $M_\odot$, while 91 per cent of centrals with $M_\star > 10^6$ $M_\odot$ are star-forming by $z = 0$, with outliers in quenching status also being outliers in halo mass. This indicates that satellites of $M_\star = 10^{6-7}$ $M_\odot$ are ideal probes of environmental quenching, while satellites with $M_\star > 10^8$ $M_\odot$ are difficult to quench, in agreement with previous work on the quenching of satellites of higher

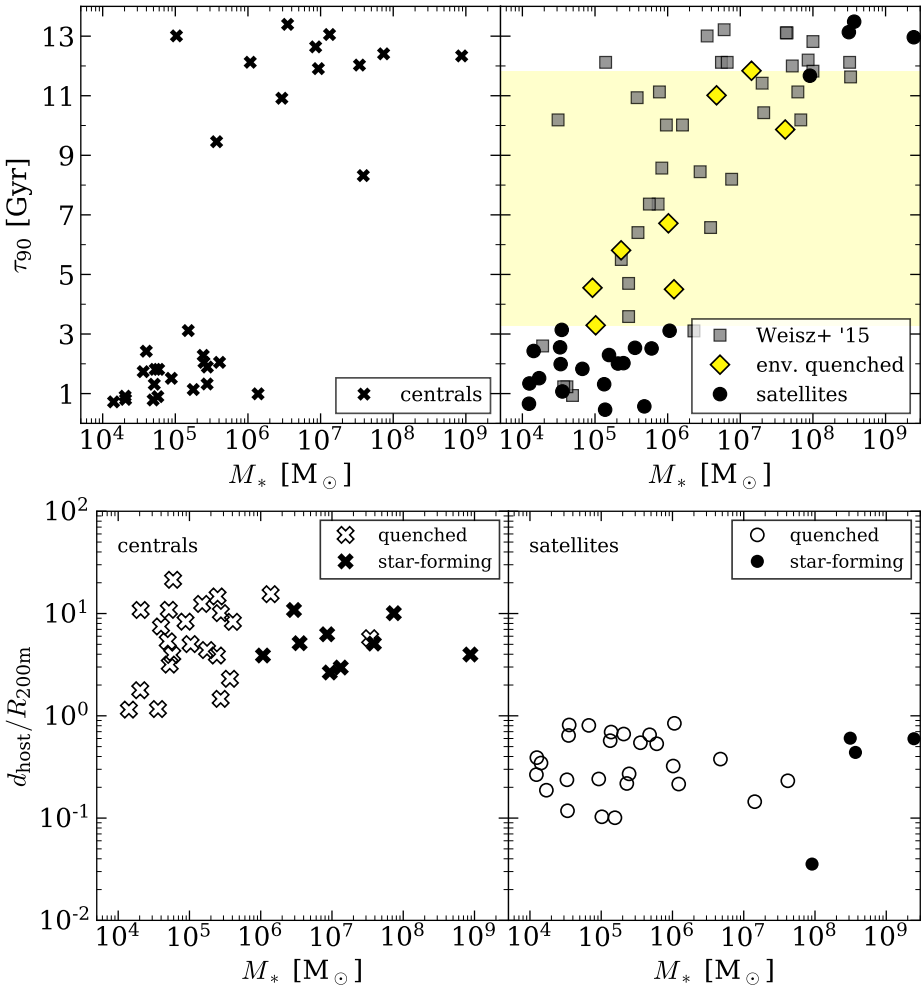

Figure 3.4: (*top panels*) Stellar mass versus the 90 per cent star-formation time-scale (τ_{90}) for simulated satellites and field galaxies, including observed local-group dwarf galaxies from [291]. We use τ_{90} here as a comparable analog to the observational data, representing the cosmic time at which 90 per cent of the present-day stellar mass was formed. The yellow shaded region denotes the range in τ_{90} for environmentally quenched satellites, which are plotted as yellow diamonds (see text for identification criteria). We find that our simulated environmentally quenched satellites fall within the distribution of observed galaxies in the local group. We find fewer low-mass late-forming satellites, though that could be due to the high variance of quenching times and our small sample size. (*bottom panels*) Stellar mass versus $z = 0$ distance to the host galaxy, normalized by $r_{\rm 200m}$. Star forming galaxies are shown as solid markers, while quenched galaxies are shown as open markers.

mass hosts [298, 291, 86, 295]. We therefore find that LMC-mass hosts, though they possess a reduced amount of substructure, may in fact be able to quench their satellites in a similar manner as MW/LG-like environments.

Figure 3.4 shows the stellar mass and 90 per cent quenching time-scale (τ_{90}) for our simulated centrals and satellites, as well as observed LG satellites as reported by [291]. The highlighted region indicates the τ_{90} range of environmentally quenched satellites (see Section 3.3.3). Note that τ_{90} and $t_{\rm quench}$ are not identical quantities; $t_{\rm quench}$ indicates the formation time of the youngest star particle, while τ_{90} represents the time at which 90 per cent of the $z = 0$ stellar mass was formed. The environmentally quenched satellites of LMC-mass hosts are consistent with the trend of observed LG satellites in their stellar masses and τ_{90}, further supporting the case that isolated LMC-mass hosts can environmentally influence their satellites similarly to the LG. The bottom panel of Figure 3.4 shows the $z = 0$ distance to the primary central normalized to its $r_{\rm 200m}$ versus stellar mass for both satellites and centrals, also marking their star-forming state. Note that there are far fewer star-forming satellites than centrals. Consistent with Figure 3.3, we define quenched satellites as those with $t_{\rm quench} < 13.2$ Gyr (i.e. not having formed a star particle in the last ~500 Myr).

3.3.3 A Closer Look at Environmental Quenching

Here we investigate the specific circumstances of quenching for the 8 identified environmentally quenched satellites (EQSs). Satellites were identified as being environmentally quenched by requiring intermediate to late quenching times such that $4\ {\rm Gyr} < t_{\rm quench} < 13.2\ {\rm Gyr}$, and proximity to the host halo $d_{\rm host}(t_{\rm quench}) < 2r_{\rm 200m}(t_{\rm quench})$. We allow for objects to be located outside the host virial radius at quenching time due to previous works highlighting the consistency of galaxies within

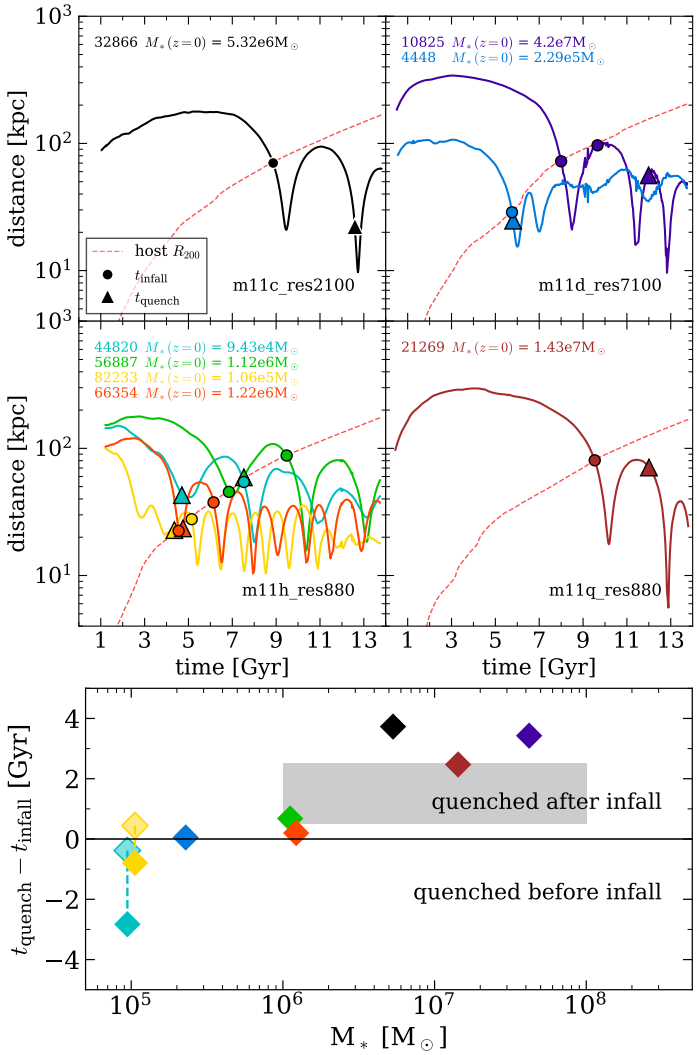

Figure 3.5: (*top panels*) Orbits of environmentally quenched satellites (EQSs), with the virial radius of the host shown as a red dashed line, infall times marked as circles, and quenching times (i.e. the formation time of the youngest star particle) marked as triangles. This population of satellites was selected as having been quenched between 4 and 13 Gyr, and that were quenched at a distance of less than twice the virial radius of their host at that time. Five of the eight galaxies were quenched before th,eir first pericenter, suggesting the gaseous halos of these simulated LMC-mass hosts are rich enough to affect satellite evolution as far away as their virial radii. (*bottom panel*) Quenching time-scales for EQSs, defined as $t_{\rm quench} - t_{\rm infall}$ such that galaxies which were quenched after infall appear above the horizontal line. The grey bar indicates the quenching time-scale due to stripping and feedback predicted for satellites of MW-like hosts [85]. In addition, we plot the time-scales corresponding to the time of closest approach for subhalos 44820 & 82233 (partially transparent cyan & yellow markers) of `m11h` due to the fact that they come within the vicinity of the host halo around their respective quenching time, but splash back on wider orbits before later falling into the host halo.

$2r_{200\mathrm{m}}$ of the MW with environmental quenching [83], indicating that the sphere of influence of the primary central is not strictly limited to such a radius. Three satellites quench outside their host $r_{200\mathrm{m}}$: 44820 at $1.7r_{200\mathrm{m}}$, 56887 at $1.06r_{200\mathrm{m}}$, and 82233 at $1.05r_{200\mathrm{m}}$.

Figure 3.5 shows the orbits of these objects, as well as the evolution of the host virial radius, whose intersection with each orbit defines the infall times (marked as circles). Halo ID numbers are shown on the figure in corresponding colors, and consistent coloring will be used in further plots that highlight this sample. Five of the eight EQSs were quenched at or near the host virial radius, often with infall times shortly before or after their quenching times, suggesting that the circumgalactic medium (CGM) of the hosts are dense enough to influence satellites of this mass. These galaxies are lower mass, with stellar masses of $M_\star \approx 10^{5-6}$ $\mathrm{M}_\odot$ and peak halo masses of $M_{\mathrm{halo,peak}} \approx 2\times10^9$ $\mathrm{M}_\odot$. The other three EQSs are more massive, with $M_\star \approx 10^7$ $\mathrm{M}_\odot$, and $M_{\mathrm{halo,peak}} \approx 10^{10}$ $\mathrm{M}_\odot$. These satellites fell into their host halos later, and quenched after first pericenter.

This trend can be seen in the bottom panel of Figure 3.5, which shows the stellar mass of EQSs compared to their quenching time-scales, defined as $\tau_{\mathrm{quench}} = t_{\mathrm{quench}} - t_{\mathrm{infall}}$. The three most massive EQSs have $\tau_{\mathrm{quench}} \approx 2-4$ Gyr, while the lowest mass EQSs have -1 Gyr $\lesssim \tau_{\mathrm{quench}} \lesssim 1$ Gyr. Objects 44820 (cyan) & 82233 (yellow) undergo a pericentric passage around the host before falling within $r_{200\mathrm{m}}$ (note the difference between quenching time and infall time markers on Figure 3.5, and the orbital minima that occur near quenching time). We therefore include a secondary τ_{quench} based on the time of this pericenter rather than the infall time, as the boundary of the DM halo is somewhat arbitrarily defined, especially when considering the baryonic effects of the central galaxy. These points are shown as partially transparent markers connecting to the original point based on t_{infall} via

a dashed line, and bring them into stronger agreement with the other low-mass EQSs, with faster quenching time-scales such that $t_{\rm infall} \approx t_{\rm quench}$.

The distinction in quenching time-scales and infall times of low-mass versus intermediate-mass satellites suggests that there may be further stellar-mass dependence within the quenching model of [85]. We have indicated their predicted quenching time-scales due to feedback and ram-pressure/turbulent stripping for satellites of MW-mass hosts in the bottom panel of Figure 3.5 as a grey bar. We find that intermediate-mass ($M_\star \approx 10^{6.5-7.5}$ M$_\odot$) satellites of LMC-mass hosts have somewhat longer quenching time-scales than predicted for satellites of MW-mass hosts. This makes sense in light of the lower stellar-mass to halo-mass ratio for dwarf galaxies like the LMC, and the predicted lower level of disruption for such systems when compared to MW-mass hosts [132]. We also find that low-mass satellites ($M_\star \lesssim 10^6$ M$_\odot$), which are not resolved in the analysis of [85], have somewhat lower quenching time-scales than predicted for intermediate mass satellites. This is likely due to the lower binding energy of their less massive DM halos, leading to higher susceptibility to ram-pressure stripping and therefore quenching earlier in the infall process from less dense gas in the outer parts of the parent halo. In principle, this mechanism should apply to hosts of any mass, suggesting fast quenching time-scales (perhaps within -0.5 to 0.5 Gyr) for low-mass satellites of MW-like hosts. It is unclear at this point whether these two subtypes (i.e. $M_\star \approx 10^{6.5-7.5}$ M$_\odot$ with $t_{\rm infall} > 8$ Gyr and quenching time-scales of $2-4$ Gyr versus $M_\star \lesssim 10^6$ M$_\odot$ with $t_{\rm infall} < 7$ Gyr and quenching time-scales of -0.5 to 0.5 Gyr) lie on a continuous distribution of satellite quenching behavior, or if there is a stellar mass cutoff between distinct populations.

The top panels of Figure 3.6 show the total and cold gas mass within $2r_{50\star}(t)$ for each EQS as a function of time. We find universally steep drop-offs in gas content near the quenching

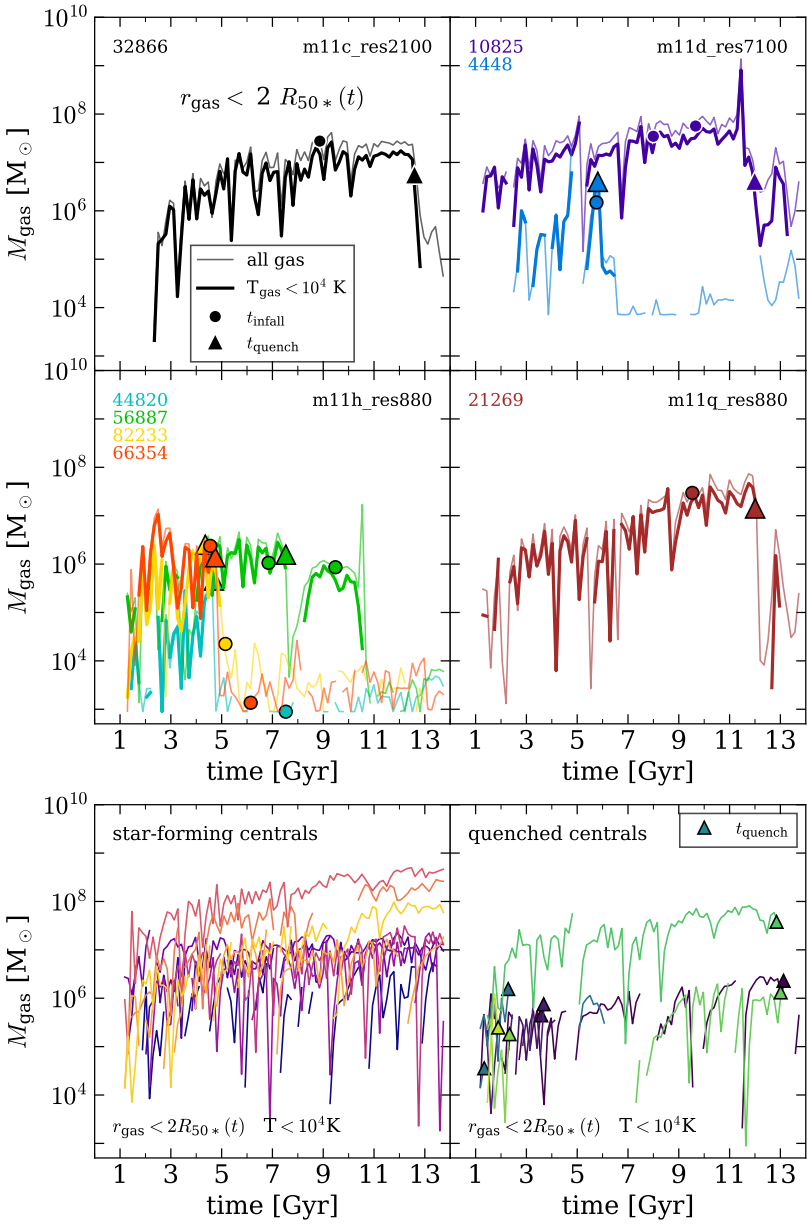

Figure 3.6: (*Top 4 panels*) Total (thin) and cold (thick) gas mass within $2R_{50\star}(t)$ for each EQS, excluding gas with high relative velocity to the satellite such that $|v_{\rm gas} - v_{\rm sat}| < 10\times\texttt{max}[v_{\rm circ}, \sigma_v]$, all measured within the satellite. Each galaxy experiences a steep drop in $M_{\rm gas}$ at or near its quenching time, indicating a removal of gas through either star formation bursts or ram pressure (or both) rather than starvation or gravitational stripping, which are characterized by slower reductions in $M_{\rm gas}$ (on the order of several Gyr or longer). (*Bottom 2 panels*) Cold gas mass within $2R_{50\star}(t)$ for star-forming (left) and quenched (right) centrals. We find a consistent presence of cold gas throughout the history of centrals that are star-forming at $z = 0$, while quenched centrals cease to contain cold gas after their quenching times.

time for each galaxy, suggesting some form of hydrodynamic gas removal, which operates on much faster time-scales than gravitational stripping or starvation [86, 76].

While some galaxies retain or even re-accrete some amount of gas, none re-ignite their star formation after the initial gas-loss event. Take, for example, the `m11h` satellite 56887 (bottom left panel, green line), which is on a splashback trajectory before settling permanently in an orbit within the virial radius of the host halo at $t \sim 9$ Gyr. This satellite loses its gas and quenches after first infall, but is able to regain some gas on its trajectory back out of the host halo. It is possible that some or all of this gas is not tightly bound to the satellite, as our velocity cuts are somewhat liberal, but $\sim 10^6$ $M_\odot$ of gas remains within that radius during the object's splashback orbit for another few Gyr before it infalls again and fully loses all remaining gas content. Interestingly, the re-accretion of gas to pre-quenching levels is not sufficient to reignite star formation in the satellite. The correlation of multiple infall and subsequent gas removal events is an encouraging suggestion that the environment of the host halo is responsible for stripping away any gas bound to the satellite. We therefore turn our attention to the CGM properties of the LMC-mass host galaxies.

The bottom 2 panels of Figure 3.6 show the history of cold gas within star-forming and quenched centrals. There are no obvious signatures in this data that distinguish the gas content of centrals from EQSs. We therefore look into further details of the gas content of EQSs in Section 3.3.3. For now, we turn our attention to the gas content of the host halos.

Characterizing the Gaseous Halos of LMC analogs

Figure 3.7 shows the temperature and density projection for each LMC-mass host in out sample, as well as the phase diagram, with each pixel colored according to the total mass of gas

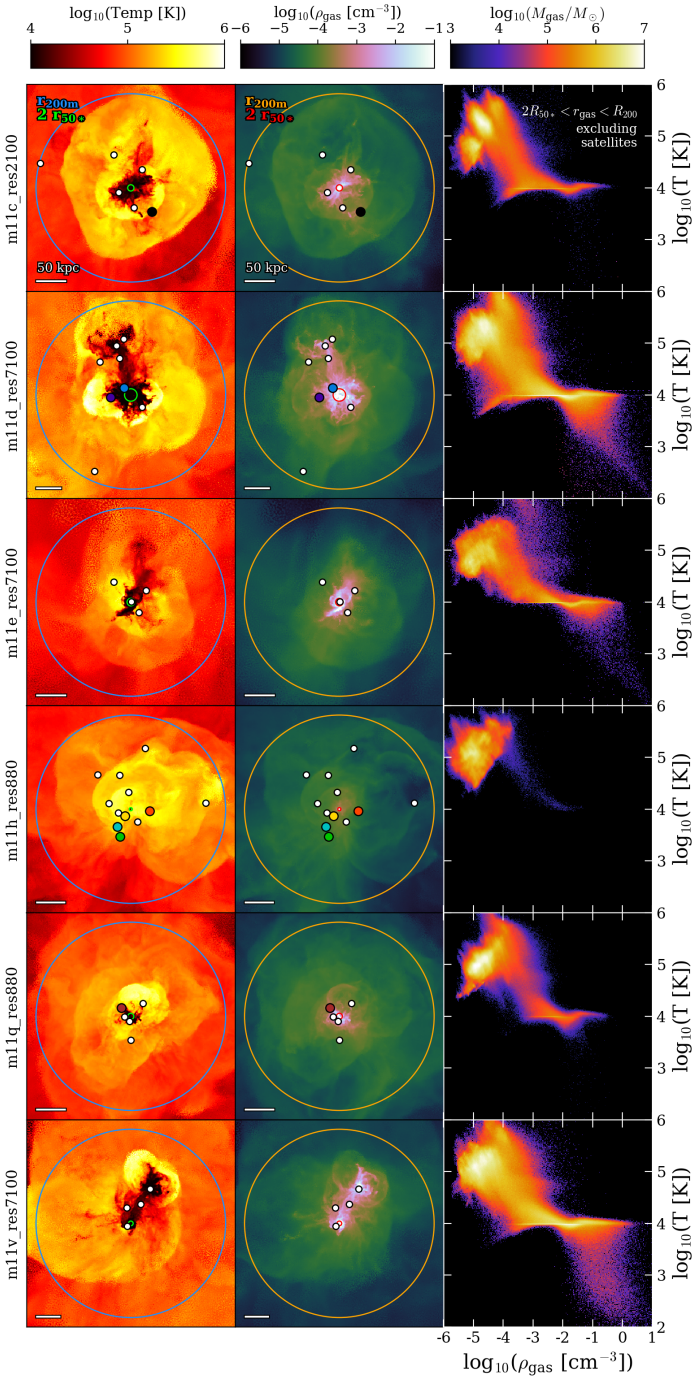

Figure 3.7: Properties of the gaseous halos of all LMC-mass halos at $z = 0$. The left column shows a projection of gas temperature, the second column shows a projection of gas density (with points marking the locations of satellites), and the right column shows the phase-space diagram for halo gas, defined as $2R_{50\star} < r_{\rm gas} < R_{\rm 200m}$ and outside $2R_{50\star}$ of luminous satellites. Each host exhibits a significant mass in a hot (T= $10^{4.5-6}$K) corona with $M = 3 - 6{\times}10^9$ $M_\odot$, with highly structured regions of hot (rarefied) versus cold (dense) gas, with visible shock fronts.

contained within it. Projections are constructed by selecting gas with $|x| < 1.1r_{200\mathrm{m}}$, $|y| < 1.1r_{200\mathrm{m}}$, and $|z| < 0.2r_{200\mathrm{m}}$, where z is perpendicular to the plane of the figure. We choose no particular orientation with respect to the host galaxy. This gas is then divided into evenly spaced 2-D (x, y) pixels, giving a column of gas with length $0.4r_{200\mathrm{m}}$. The pixel is then colored according to the median physical value of temperature or density for all particles within its boundary. If there are no particles within the pixel, it is colored according to the median value of nearest non-empty pixels.

We find that a hot, richly structured gaseous halo is present around all LMC-mass hosts to varying degrees. While not all centrals are host to EQSs, the ubiquity of the rich gaseous halo suggests that the presence of such galaxies relies more on varying cosmological abundances of structure than it does on the ability any particular LMC-analog to quench its satellites. We identify two primary components of the CGM based on features in the phase diagrams: the hot corona, found in the upper left quadrant, and the horizontal feature of T $\sim 10^4$ K gas with $10^{-4} \lesssim \rho/\mathrm{cm}^{-3} \lesssim 10^0$. Some runs also contain a small component of cold, dense gas in the lower right quadrant. Star-forming gas in FIRE is restricted to densities above 10^3 cm^{-3}, and is not abundant enough outside of $2R_{50*}$ compared to the halo gas to appear on this figure.

Quantifying the hot corona as gas with $10^{4.5} < \mathrm{T/K} < 10^6$, and $10^{-6} < \rho/\mathrm{cm}^{-3} < 10^{-4}$, as well as being located outside $2r_{50\star}$ of the host galaxy and all satellite galaxies, we find that LMC-mass halos have $3{\sim}6{\times}10^9$ M$_\odot$ of gas in their hot coronas. Additionally, we find mean gas densities of ${\sim}5{\times}10^{-4}$ cm^{-3} and mean temperatures of ${\sim}1{\times}10^5$ K, both quantities volume-weighted. These predictions are in good agreement with the detection of a hot ionized component in the LMC [284, 162] suggesting the presence of hot gas around the Magellanic clouds as well as with recent theoretical arguments of a need of a hot corona in the LMC to fully explain the morphology of the

Magellanic stream [168]. While there are differences in the presence and radial distribution of hot and cold CGM components between LMC and MW-mass galaxies in the FIRE-2 simulations [262], the existence of a relatively massive hot component out to $\gtrsim 100$ kpc is consistent between host mass scales.

Quenching via Ram-Pressure and Feedback

There are many possible sources for gas removal in satellites, for example, energetic feedback from star formation which can be induced by the increased pressure of the host environment, interactions with other galaxies, or ram-pressure stripping from the ambient halo gas. The time-scale of gas removal seen in Figure 3.6 is short enough to rule out starvation, which occurs on longer time-scales as gas reservoirs within the satellite are depleted [86]. Interactions such as fly-by events and ram-pressure stripping are functions of environmental properties (abundance of satellites, density of gas), while feedback-driven, self-induced quenching only depends on the star formation history of each galaxy (though the SFH may also be dependent on host environment). It is likely that a combination of these effects simultaneously occurs in orbiting satellites.

Although the energetic feedback of the FIRE simulations is certainly enough to strongly affect the ISM of dwarf galaxies [73, 74, 72, 127], the general lack of isolated dwarfs with $t_{\rm quench}$= 4 – 13 Gyr and $M_\star = 10^{5-7}$ M$_\odot$ makes self-quenching alone an unlikely cause for the halting of star formation in these satellites. However, one could not rule out environmentally induced starbursts (i.e. from compression of gas at orbital pericenters), or removal of low density gas blown out by feedback, which may have cooled and fallen back into the satellite if it were in isolation, but is easily swept away by the high density of the host's ISM. Such effects, which may not neatly be described

as strictly environmental or strictly self-induced, seem to drive the evolution in some of the satellites in our sample, as illustrated by the two case studies presented here.

Figure 3.8 shows a series of density projections at four sequential time stamps of two low-mass satellites of `m11h` that were quenched near its virial radius. Also shown is the normalized gas velocity field in the reference frame of each satellite. Time stamps were chosen simply to highlight the state of the gas in and around each satellite as it is quenched, with the first panel being chosen as the snapshot immediately prior to the formation of its last star particle. The stellar half mass radius of each satellite is also shown as a red circle. Each frame is centered on the satellite's position at the given time.

The top row shows a satellite with $M_{200\mathrm{m}}(t_{\mathrm{quench}}) \approx 3 \times 10^9$ M$_\odot$, $M_\star(t_{\mathrm{quench}}) \approx 2 \times 10^6$ M$_\odot$, and $M_{\mathrm{gas}}(t_{\mathrm{quench}}) \approx 10^6$ M$_\odot$, where $t_{\mathrm{quench}} = 4.75$ Gyr. It demonstrates trails characteristic of ram pressure in the first panel, but the gas is sufficiently dense in its core as to resist stripping. The velocity field reveals turbulence around the galaxy as well, though there is a clear front of gas moving downwards from the top of the figure. The second panel shows a burst of star formation that moves this gas out of the central region, heating and rarefying it. This enables the gas to be pushed out of the halo by the pressure from ambient halo gas in the third panel, resulting in no clear gaseous component to the halo in the fourth panel, where the velocity field has become more uniform. This process is generally consistent with ram pressure stripping, though it requires sufficient stellar feedback to 'loosen' the gas within the satellite before the ambient halo pressure is capable of stripping and quenching it.

The bottom row shows a second similar mass satellite, with $t_{\mathrm{quench}} \approx 4.5$ Gyr, this time with a much more uniform velocity field. This object demonstrates a more standard picture of ram

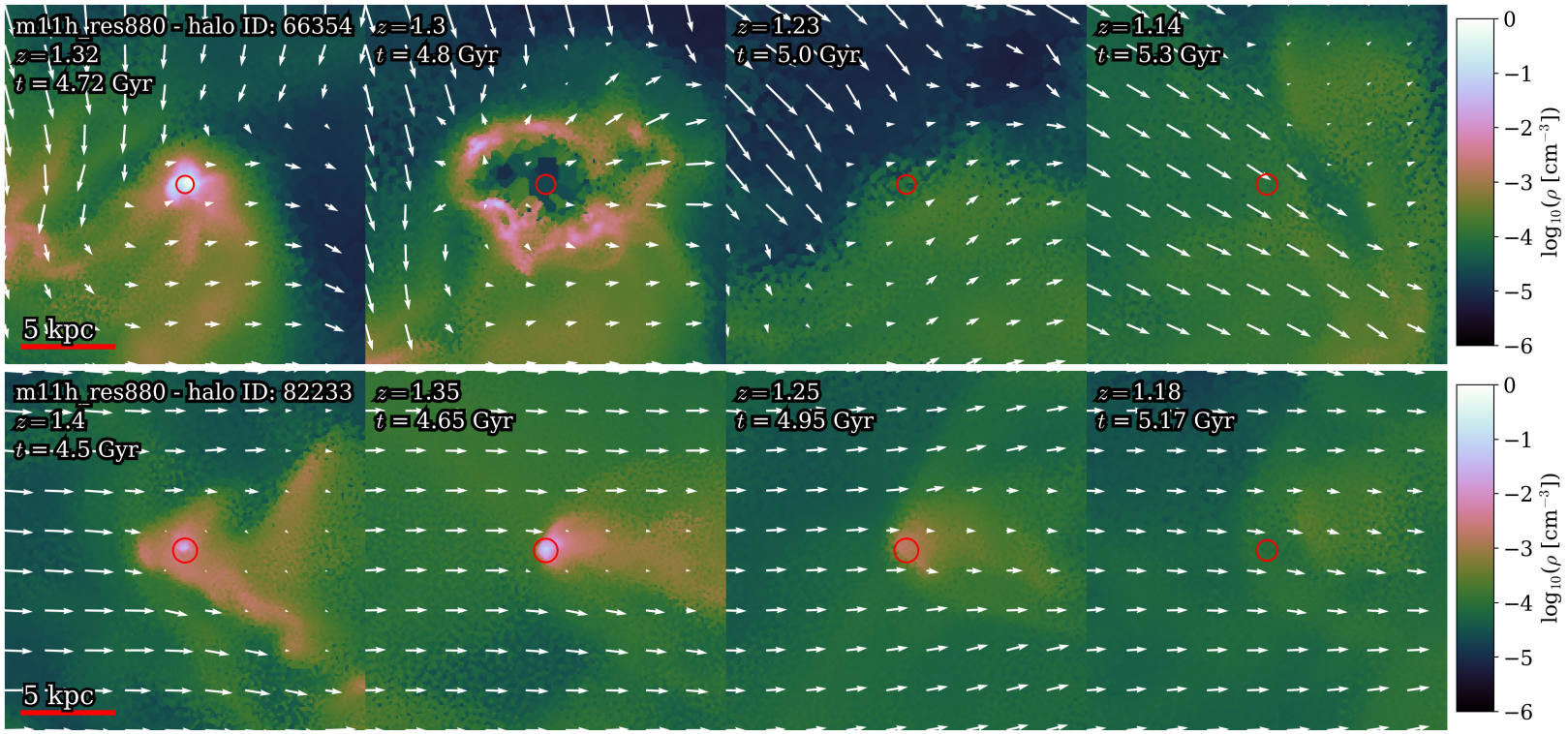

Figure 3.8: Gas density (color) and velocity (arrows; in the reference frame of the satellite) projection of two satellites of `m11h` as they fall into the host halo, demonstrating two primary modes of quenching: SF-driven stripping (*top*) and standard ram pressure stripping (*bottom*). Each image is centered on the halo location as provided by `ROCKSTAR` at the shown snapshot, despite the lack of obvious structure in later panels. The satellites are similar in size, with $M_{200\mathrm{m}}(t_{\mathrm{quench}})2{\approx}3{\times}10^9$ M$_\odot$ and $M_\star(t_{\mathrm{quench}})1{\approx}2{\times}10^6$ M$_\odot$, and they both quench around $t \sim 4.5$ Gyr. The first panel of both rows shows the satellite near t_{quench}, with visible tails due to its motion through ambient halo gas. The top row demonstrates quenching due to a combination of feedback and ram pressure, which is a common mechanism among our population satellites. The bottom row demonstrates a classic example of ram pressure stripping of a satellite.

pressure characterized by a gas stream extending from the satellite opposite the direction of motion. There is no feedback event that processes the gas prior to stripping - the pressure from ambient halo gas is sufficient to strip away the dense, bound gas within the satellite. Note that the second panel shows an increased amount of dense gas within $r_{50\star}$ due to compression via the ambient velocity field. The time-scale for each galaxy to go from possessing dense, concentrated, star-forming gas to possessing virtually no gas is $\sim$ 300 Myr in both cases, though it is slightly faster in the case where feedback is involved.

An important qualification to this analysis is that both satellites come from the same parent halo – `m11h`. This halo is host to an unusual abundance of satellites: 10 in total (12 including all subhalos with assigned star particles, forgoing the cuts described in Section 3.3.1). As seen on the left side of the first panel of the top row in which an additional locus of dense gas is present, satellite-satellite interactions can also be a source of environmental quenching. This particular event seems to have compressed the gas in the satellite shown, leading to a strong burst of star formation, rarefying the gas and making it more susceptible to ram-pressure stripping via the halo gas. These objects were chosen for the case study due to their high resolution and obvious visual features. We have done a similar analysis of all EQSs and find ram-pressure alone or in combination with feedback from star formation to be the quenching mechanism for all EQSs.

Interactions can also be seen in the orbits of the above objects in Figure 3.5 which appear to have pericenter with some object other than the host prior to final infall. We have checked this explicitly, though the other satellites are not shown on the figure for visual clarity. We include this type of interaction under the umbrella of environmental quenching, though it does require the presence of sufficiently many companion galaxies for satellite-satellite interactions to take place. It

is unclear how cosmologically common this is for LMC-mass hosts, but in our set of 6 centrals and 30 satellites, we identified 1 host with 2 instances of interactions.

The pre-processing of satellites prior to infall is a natural prediction of ΛCDM [166, 292, 17], with part of the aim of this study to understand how the environment of the LMC could have affected its satellites prior to the group's infall into the halo of the MW. We expect that pre-processing – whether due to prior group association or individual fly-by events – before to infall into LMC-mass halos will perhaps be less common than for systems like the MW, simply due to the relative abundance of structure in each. However, this example demonstrates that pre-processing on much smaller scales than the MW is indeed possible, and perhaps contributes to the relatively high amount of environmentally quenched satellites within `m11h`.

3.4 Effects of Tides on Satellites of LMC Analogs

It has been shown that MW-mass galaxies are hosts to rich tidal features including coherent stellar streams and kinematically mixed stellar halos [118]. These features result from interactions between dwarf satellites on close orbits with their more massive hosts that tidally strip mass (both dark and luminous) from their companions. Similar processes are expected to occur also for satellites of lower mass hosts, with a handful of observations confirming the presence of tidal streams in satellites of dwarf-mass centrals [e.g., 184].

To investigate the tidal stripping of simulated satellites around LMC-mass hosts, the top panel of Figure 3.9 shows the dark matter mass of satellites as a function of time, with the previously described population of environmentally quenched satellites (EQSs) highlighted. We find that the majority of satellites experience tidal stripping of their dark matter halos, beginning at or near their

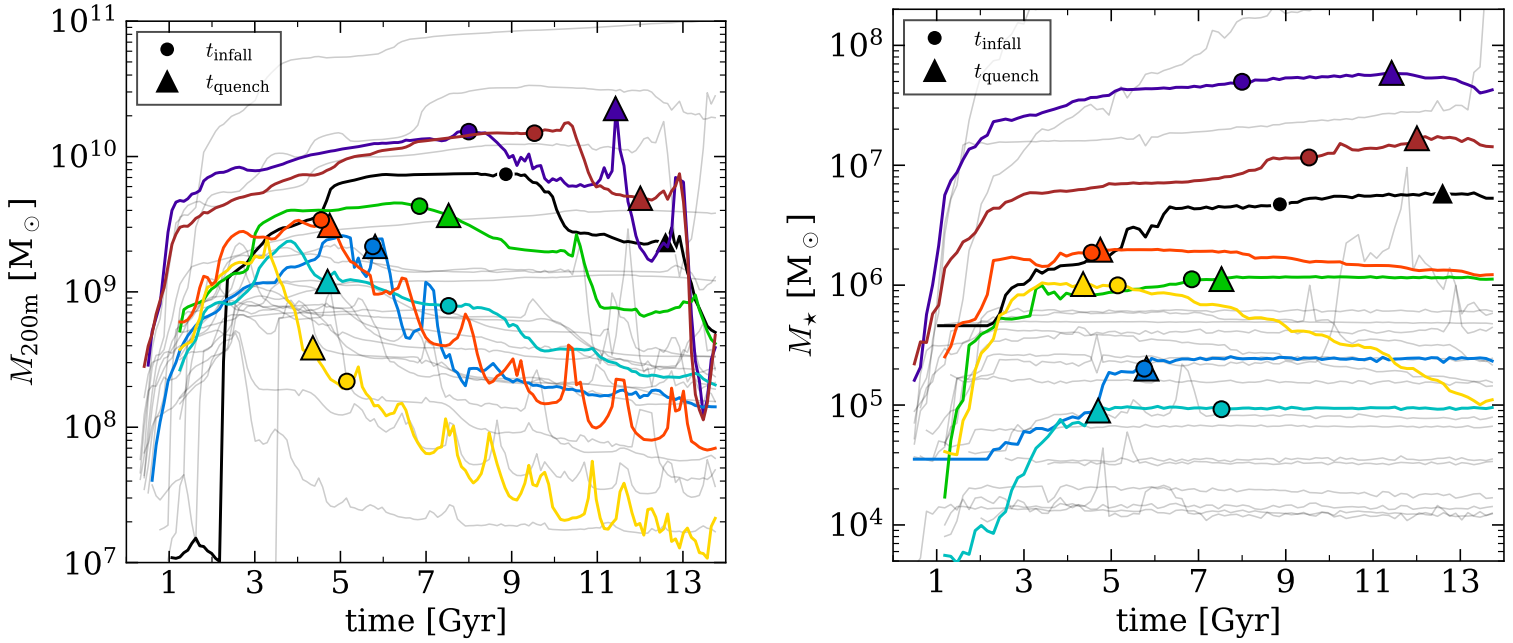

Figure 3.9: (*Top*) Dark matter and (*bottom*) stellar mass of all satellites versus time, with environmentally quenched satellites highlighted in color. All such satellites experience significant tidal stripping of their DM halos after infall, with anywhere from 82 – 99.9 per cent of the DM mass being lost by $z = 0$. Stellar masses shown here are from ROCKSTAR, and do not necessarily reflect all stellar mass loss due to stripping as streams are not detected and removed. However, stripping of the stellar component can still be seen in objects 82233 & 66354 (yellow and orange, respectively).

infall times onto the host, with EQSs generally experiencing the largest decreases in halo mass, losing 82 – 99.9 per cent of the peak halo mass ever obtained.

In one case (halo ID 82233, yellow), the satellite appears to have its halo mass reduced by a factor of $\sim 5\times$ prior to quenching, and by $\sim 10\times$ prior to first infall. This is the galaxy shown on the bottom panel of Figure 3.8. It is clear from our previous analysis that ram-pressure plays an important role in its quenching, but here we demonstrate that it is also subjected to severe tidal stripping. This object also experiences the highest magnitude of halo mass loss by $z = 0$ due to its short orbital period, early infall time, and apparent interaction with other satellites prior to infall, as seen in Figure 3.5.

The bottom panel of Figure 3.9 shows the evolution of stellar mass of all satellites. Most satellite galaxies do not experience significant stripping of their stellar components as they are deeply segregated in the inner regions of their dark matter subhalos [210], but we do find a handful of objects that appear to have had various degrees of stellar mass loss due to stripping. Significant halo mass loss is not necessarily a guaranteed indicator of stellar stripping, but the two halos which lost the highest fraction of halo mass also lost the highest fraction of stellar mass (82233 & 66354). This makes sense as the DM component is far more extended than the stellar component, and would therefore be first to be stripped away when tidal forces begin to take hold.

Since gravitational interactions with satellites are known to be a source of stellar tidal streams in MW-mass galaxies, we plot the $z = 0$ locations of star particles that were assigned to any satellite galaxies at their infall times in Figure 3.10. Streams were then identified by examining the evolution of the spatial distribution of such star particles. Streams became apparent when star particles were pulled from their original locations within satellites as they made close approaches to

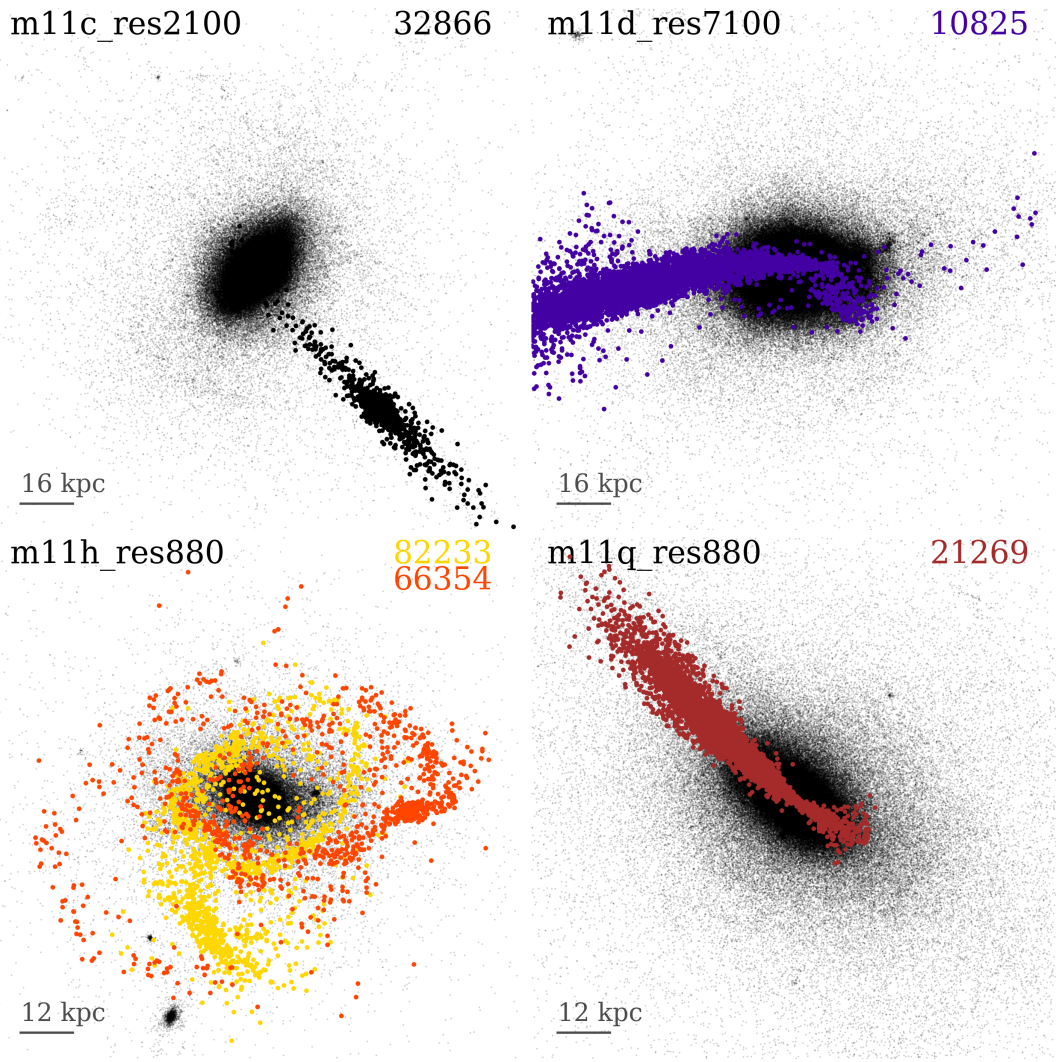

Figure 3.10: Tidal streams at $z = 0$ originating from stripped satellites around LMC-mass hosts. Small, black dots are star particles belonging to the host galaxy at $z = 0$, while thicker dots are the present-day locations of star particles belonging to satellites of the corresponding color at their first infall times. We find coherent stellar streams in all hosts with EQSs (Environmentally Quenched Satellites), and none in hosts without EQSs. It is unlikely that the quenching is a direct result of this tidal stripping, but these could be correlated as a result each effect's individual dependence on satellite mass (coherent tidal streams require sufficiently many stars to strip - as well as late(r) infall times - while environmental quenching requires sufficiently high mass as to not by quenched by reionization heating).

the host, forming extended stellar structures. We find four hosts with tidal streams originating from five satellites.

We find no tidal features that arose from any satellite galaxy that was not environmentally quenched, be it a low-mass early quenched galaxy, or a high mass star-forming galaxy. This may be a result of mass selection: low-mass satellites, while occurring frequently and infalling early, do not possess a large population of stars that can be striped with a well-resolved stream in our runs, meanwhile, high mass satellites, while having an abundant stellar component, are less common and infall late, thus not having sufficient time to interact with the host. Tidal stripping is not the dominant factor in quenching these galaxies (see the location of triangle symbols in Fig. 3.9 mostly not correlated to stripping events). It is simply that satellites that were quenched due to ram-pressure stripping seem to be also those experiencing significant tidal stripping not only of their dark matter but also of their stars.

The streams depicted in Figure 3.10 are highly extended, containing stars located within ~1-4 kpc of the primary host galaxy out to ~80 kpc. All stripped stars are on highly radial orbits, in agreement with previous theoretical predictions [2]. The amount of stellar mass contained in the streams ranges from 10^{6-7} $M_\odot$, with a median value of 2×10^6 $M_\odot$. The streams around our simulated LMC-mass galaxies are quite substantial, and may be observable around dwarf centrals through deep photometry.

We find that tidal structures result from the highest mass environmentally quenched satellites, having a stellar mass range of $M_{\star,\mathrm{max}} = 10^{6\sim7}$ $M_\odot$. Most satellites in this mass range though are star-forming and late-infallers. The tidal structures from later-infalling satellites (such as those around `m11c`, `m11d`, and `m11q`) are morphologically distinct from those formed by early-infalling

satellites, as they have not experienced enough dynamical times to become kinematically mixed. The streams around `m11h` originate from satellites that fell in around 9 Gyr ago, and have undergone many pericenters as seen on Figure 3.5. This results in streams that are more diffuse, though still retaining clear spatial cohesion along the orbital path.

We note that we only investigate stellar streams that form directly as the result of tidal forces that strip stars from satellite galaxies as they orbit the central. Extended stellar structures also exist in the form of in-situ stellar streams and stellar halos, which have been investigated in the FIRE simulations [e.g. 306]. [73] showed that galaxies with $M_\star = 10^{6.3-10.7}$ M$_\odot$ experience radial migration of stars on both short and long time-scales due to star-forming clouds that are driven to high radial velocities from bursty feedback, as well as due to energy transfer from the fluctuation of the galactic potential. This migration can result in stars located $\gtrsim 10$ kpc from the radial position of their formation, contributing to wide variations in half light radius over time. They note that the stellar mass range $M_\star = 10^{7-9.6}$ M$_\odot$ is optimal for maximizing the physical effects that cause stellar migration, suggesting that LMC-mass centrals may have a significant in-situ stellar halo as well.

Recently, [206] investigated the formation of stellar streams around MW-mass galaxies in the FIRE-2 simulations. They find that present-day satellites are good proxies for the progenitors of stellar streams. They further show that low mass ($M_\star < 2.25 \times 10^6$ M$_\odot$) stream progenitors are likely to have their star formation quenched prior to infall, while progenitors above that stellar mass threshold are quenched by the host environment. This is consistent with our analysis of EQSs, though we find that low-mass stream progenitors may be environmentally quenched as well.

While tidal features arising from satellite interactions have been observed around dwarf galaxies [184, 39], their frequency in as of yet unknown. The presence of resolved stellar streams in configuration space around four of our six LMC-mass hosts is an encouraging sign that satellite-host interactions may result in observable tidal structures in a substantial fraction of LMC-mass dwarf galaxies in the field.

3.5 Summary & Conclusions

We investigate various properties of the satellite population of six LMC-mass hosts in the FIRE simulations. By comparing their star formation histories (SFHs) to those of other centrals of similar stellar mass in Figure 3.2.1, we find that LMC satellites have more diverse SFHs and quenching times than central galaxies, which are strongly bimodal – either forming all their stars before $t = 4$ Gyr, or continuing active star formation at $z = 0$. We further compare to simulated satellites of Local Group pairs from [98] (also in the FIRE simulations), and find that satellites of LMC-mass hosts have similar SFHs to LG-satellites at fixed mass. LMC satellites retain the general mass-dependence of quenching times: low mass satellites ($M_\star < 10^6$ M$_\odot$) quench early, while high mass satellites ($M_\star > 10^7$ M$_\odot$) quench late or continue forming stars, as shown in Figure 3.3. Intermediate mass satellites have the greatest diversity of quenching times (Figure 3.4).

We identified 8 environmentally quenched satellites, selected as having intermediate quenching times ($t_{\rm quench}$= 4 − 13 Gyr) and located within twice the virial radius of the host at the time of quenching. By examining their orbits and quenching time-scales (Figure 3.5), we identify two subtypes: higher mass, late infalling satellites that quench after first pericenter; and lower mass, early infalling satellites that quench near the host virial radius. It is unclear whether these

subtypes are distinct populations, or if quenching time-scale and infall time are continuous functions of stellar mass. Encouragingly, early data from the LBT-SONG survey also hints at environmental quenching occurring in satellite dwarfs of two observed LMC-like hosts, NGC 628 [54] and NGC 4214 [92].

All our simulated galaxies experience a stark drop in their gas content after quenching (Figure 3.6), indicating hydrodynamic rather than gravitational effects. We find that the LMC-mass hosts contain hot, richly structured gaseous halos, with $3 \sim 6 \times 10^9$ $M_\odot$ of gas in their hot ($T = 10^{4.5-6}K$), diffuse ($\rho = 10^{-6} - 10^{-4} cm^{-3}$) coronas, as shown in Figure 3.7. We further demonstrate that this rich environment is able to strip gas from satellites via ram-pressure, halting their star formation. This process can be made more efficient through internal burst of feedback within the satellite, moving its gas to a higher energy state and expediting the effects of ram-pressure. Case studies of two satellites that illustrate quenching due to SF-aided ram-pressure stripping versus pure ram-pressure are shown in Figure 3.8

By examining the evolution of the dark and stellar mass components of satellites, we find that all 8 environmentally quenched satellites have lost 82 – 99.9 per cent of their peak DM mass via tidal stripping, with other satellites undergoing varying amounts of DM loss, some losing almost none due to their late infall times, as shown in Figure 3.9. Stellar mass loss greater than ~10 per cent due to tidal stripping is rare, happening in only 2 satellites in our sample.

We investigate vestigial structures of host-satellite interaction by identifying the $z = 0$ location of stars that were assigned to satellites at their infall times, and find extended stellar streams around 4 of 6 LMC-mass hosts, seen in Figure 3.10. All originated from environmentally quenched satellites. Three formed from $M_\star = 10^{6.5-7.5} M_\odot$ satellites infalling within the last ~2 Gyr, while

the two streams around the fourth host originated from (pre-infall) $M_\star \approx 10^6$ $M_\odot$ satellites with infall time ~8 Gyr ago, around $z \sim 1$.

Our findings have strong implications for current and upcoming observational missions targeting LMC analogs in the field. We suggest that such objects may be host to 1-4 intermediate mass ($M_\star = 10^{5-7}$ $M_\odot$) satellites which are likely to be environmentally quenched at intermediate – late times ($t_{\rm quench}= 4 - 13$ Gyr), depending on mass. This satellite population would be present along side a potential bright, star-forming satellite, as well as $\gtrsim$3 ancient ultrafaint satellites with $10^4 \leq M_* \leq 10^5$ $M_\odot$, though not all of our runs resolve this scale. LMC-mass galaxies in the field can additionally host tidal streams due to past interactions with their satellites.

Chapter 4

Real and counterfeit cores: how feedback expands halos and disrupts tracers of inner gravitational potential in dwarf galaxies

4.1 Introduction

The difference between the structure of dark matter (DM) halos as predicted by the Lambda-Cold Dark Matter cosmological model (ΛCDM) and that which is inferred by observations of gas rotational profiles in galaxies is a long-standing problem in modern cosmology [188, 89] with a wide range of postulated solutions. The structure of DM halos as predicted by DM-only simulations [e.g. 299, 256] is characterized by steeply rising density profiles ('cusps') in the inner

regions of halos, parameterized by the NFW profile [196] which gives a power-law slope α of this inner profile of -1. Early measurements of rotation curves in dwarf galaxies have shown regions of constant density known as 'cores' with power-law slopes of $\alpha \sim 0$ [e.g. 36, 55, 56, 156]. While there is substantial evidence for the existence of cores in dwarf galaxies [e.g. 102, 152, 199, 200, 164], there is debate over the reliability of certain techniques for the inference of the true dark matter potential [101, 202].

Another complication to this dilemma is that observed rotation curves in dwarf galaxies exhibit a wide variety of behavior, including rotation curves that rise more rapidly than the NFW profile, consistent with a contraction of the halo, and those that rise significantly more slowly, consistent with expansion. Despite their success in reproducing many observed properties of galaxies, both local and statistical, [280], hydrodynamical simulations of galaxy formation have consistently predicted a uniform shape for rotation curves, posing a problem in replicating the observed diversity [203, 202, 220, 236, 238].

A theoretically appealing solution to these discrepancies is that the nature of DM is more complex than proposed in ΛCDM. Proposed models include warm dark matter [61, 20] and self-interacting dark matter [SIDM, 305, 255, 281, 226, 274]. SIDM has been fairly successful in reproducing diverse rotation curves [e.g. 51, 222, 140] and explaining the diversity of MW satellites [307]. It is worth noting, however, that results for SIDM can depend strongly on the adopted cross-section. Another interesting proposal includes a new hypothetical ultra-light scalar particle with a de Broglie wavelength on astrophysical scales, forming a Bose-Einstein condensate the size of the DM halo, known as fuzzy dark matter [128, 187, 159, 37]. While these models prove viable alternatives

to ΛCDM with testable predictions [224, 27], they may remain difficult to distinguish from CDM on small scales, especially when the effects of galaxy formation are taken into account [75, 87].

It has also been proposed that the feedback-driven motion of baryons within the halo can gravitationally perturb the dark matter potential, leading to expansion [195]. The repeated outflow of gas following bursts of star formation (SF) has been demonstrated to be a more realistic mechanism for core formation than single, highly violent outbursts [219, 104]. This framework was theoretically quantified by [214] who introduced an analytical model for core formation in which dark matter particles acquire energy and migrate to more distant orbits via repeated oscillations in the central gravitational potential, driven by supernova (SN) feedback.

Since the physics of star formation and feedback have not been fully physically constrained, different effective models of ISM physics implemented across the literature have produced different physical outcomes. For example, the Illustris simulations have been successful in reproducing many properties of galaxies [100, 279, 277], but have not been able to produce DM cores [47]. The EAGLE simulations [242] have also been shown to not produce DM cores under their fiducial model [241, 18]. Zoom-in simulations using the same prescriptions as EAGLE and Illustris have been performed and similarly demonstrate an inability to induce expansion in the DM halo [e.g. 22], indicating that resolution is not responsible for this effect in these models. Meanwhile, other simulations, including [308], the FIRE project [122, 127, 44, 293, 88], and NIHAO [286, 271, 70], have been able to produce cores in dwarf galaxies that more closely match observations, indicating that the prediction of DM cores is model-dependent to some degree.

Differences in the modeling of baryonic physics have long been quantified by the SF density threshold, which is the minimum gas density required to form a star particle. [214] showed that

cosmological zoom-in simulations run with the GASOLINE code were unable to induce core formation when using a value of $\rho_{\rm th} = 0.1$ cm^{-3}, but cores did indeed form when increased to $\rho_{\rm th} = 100$ cm^{-3}, a value consistent with the observed densities of molecular clouds [82]. Recent work has therefore focused heavily on this parameter, arriving at similar conclusions within the EAGLE simulations [18], and NIHAO [69]. It has long been reported that 'bursty' SF drives repeated outflows, thereby expanding the DM halo by driving mass to the outer regions [29, others?]. [18] conclude from their numerical tests on the density threshold that rapid fluctuations in gas content resulting from bursty SF are insufficient to alter the inner DM halo, but that gas must accrete to high levels of density, dominating the inner gravitational potential before being blown away in order to induce core formation. They also make note that there is no simple relation between SF history and core formation. [69] also find that a higher value of $\rho_{\rm th}$ induces cores in the NIHAO simulations, but their analysis suggests that fluctuations in SF feedback (and therefore gas content) must occur on *sub-dynamical* timescales in order to induce core formation. Both authors agree that SF burstiness is insufficient to fully explain halo expansion, and that the density threshold is strongly indicative of a resulting flattened inner DM distribution.

The energetics of core formation discussed in [214] require rapid motion of sufficiently dense gas clouds in the inner regions of galaxies in order to perturb the gravitational potential and transfer DM to larger orbits. High resolution simulations that lack detailed physical modelling are unable to capture the small-scale effects of energetic coupling between SF and the ISM due to the use of low star formation threshold, often with $\rho_{\rm th} = 0.1$cm^{-3}, as well as effective equations of state rather than explicitly implemented cooling physics. Meanwhile, detailed ISM models that self-consistently treat a multiphase, structured ISM are relatively new and have not been directly

applied to the problem of core formation. In short, the majority of models that have been used to study this problem are empirically calibrated to reproduce scaling relations of populations of galaxies and implemented in large-volume simulations. These models have been adapted to high resolution zoom-in simulations, with mixed results [18, 22]. Fewer studies have focused on studying core formation as a thoroughly small-scale problem, requiring both high resolution zoom-in simulations and models that capture the local details of physical processes relevant to the state of the ISM. More details of the varying approaches to galaxy modeling are given in a recent review of cosmological simulations [280].

While there is broad agreement in the literature that high thresholds induce cores [e.g. 104, 174, 268, 59, among the previously listed] and low thresholds do not do not [203, 241, 22], there have been limited systematic investigations of the physical outcomes of modeling choices, including comparative analyses of parameters within the same overall modeling scheme. The consistency of models with similar $\rho_{\rm th}$ does not rule out the possibility that other modeling choices contribute to halo expansion, including ones that cannot be neatly quantified by a single parameter.

Beyond the physical effects of baryons, difficulties in observing and modeling gas rotation curves in galaxies have led to speculation that large uncertainties might be partially responsible for the observed diversity of galactic rotation curves. While extensive work has been done to improve observational techniques for estimating velocity profiles [157, 156, 4], techniques based on alignment of metallicity populations [e.g. 285] and tilted-ring modeling [e.g. 228, 131] have been recently been demonstrated via application to the APOSTLE simulations to predict DM cores when none actually exist [101, 202]. This, combined with the large degenerecies in modeling rotational velocities in the

presence of non-circular motions [179, 238] suggest that the observed diversity of rotation curves might not be solely a result of physical processes within galaxies, be they baryonic or dark.

In this study, we compare the novel Stars and MUltiphase Gas in GaLaxiEs (SMUGGLE) feedback model [181] to the classic [260] (SH03) model, as they represent two paradigms of galaxy formation modeling (i.e. top-down – SH03, and bottom-up – SMUGGLE) while implementing the same method of solving gravity+hydrodynamics [AREPO, 258]. We aim to investigate the differences in and relationship between galaxy formation and DM distribution within these two modeling paradigms in a controlled environment through the use of idealized simulations of a single dwarf galaxy. We also implement variations in model parameters (density threshold and local SH efficiency) within SMUGGLE to shed light on their relevance to core formation within this model, and how their differential effects within this model compare to previous numerical experiments.

The paper is organized as follows: in Section 4.2, we discuss the set up of our isolated dwarf galaxy simulations; in Section 4.3, we compare the phenomenological differences between an isolated dwarf galaxy ($M_\star \sim 10^8$ M$_\odot$, $M_{200\mathrm{m}} \sim 10^{10}$ M$_\odot$) run with each model, and then introduce variations in the SMUGGLE model to investigate the physical nature of core formation in Section 4.4. We conclude in Section 4.5 by examining the morphology of each run, including an investigation of the variation of rotational velocity curves of gas. We summarize our findings in Section 4.6.

4.2 Methods

We analyze a set of high-resolution, idealized simulations of isolated dwarf galaxies of $M_\star \approx 10^8$ M$_\odot$ in halos of mass $M_{200\mathrm{m}} \approx 10^{10}$ M$_\odot$ run with the moving mesh code AREPO [258, 288].

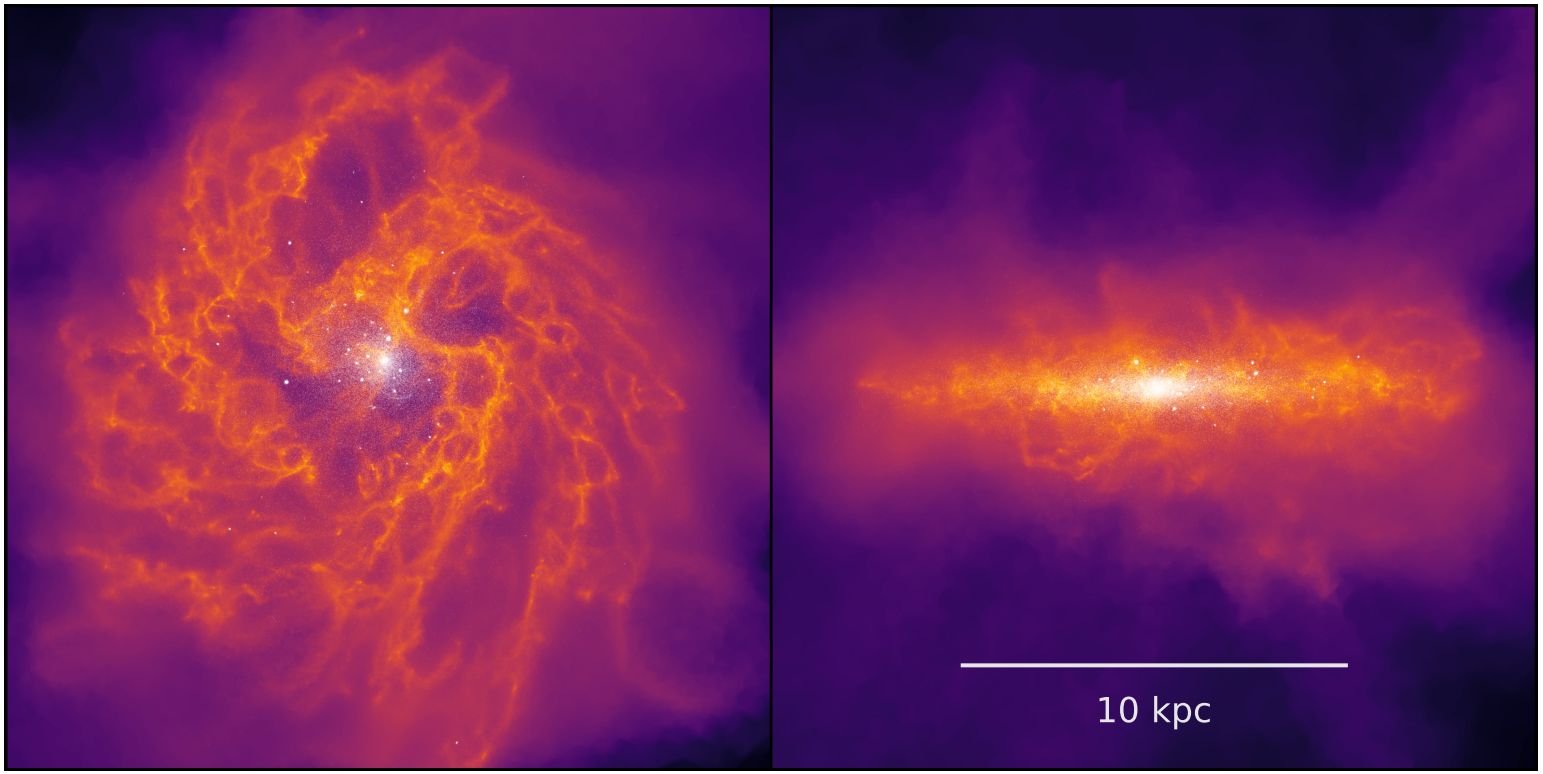

Figure 4.1: Face-on and edge-on surface density projections of the isolated dwarf galaxy on the fiducial SMUGGLE model generated with the Cosmic Lyα Transfer code [COLT, 252, 251]. Stars formed during the duration of the simulation are shown in white, with gas color-weighted according to surface mass density. The width of each frame is 20 kpc. The richly structured ISM is a result of the detailed ISM physics included in the SMUGGLE model.

This scale of stellar mass to halo mass has been demonstrated to form feedback-driven cores in other simulation codes [e.g. 59, 271].

Initial conditions were generated via the method described in [259], while star formation and feedback were subsequently enabled via the SMUGGLE model [181]. SMUGGLE implements a wide variety of sub-resolution processes, including gas heating and cooling from which a detailed, multiphase inter-stellar medium (ISM) emerges, a stochastic formation process for stars, and feedback via supernovae (SNe), radiation, and stellar winds.

Previous work with SMUGGLE includes [165], who study the formation of giant molecular clouds (GMCs) in Milky-Way mass galaxies, in particular the response of GMCs to various choices of the local star formation efficiency - a parameter we study here as well. They find that SMUGGLE is able to regulate star formation through feedback, with a 3-fold increase in star formation rate (SFR) in runs with no feedback processes enabled. This result is encouraging as it enables self-consistent prediction of kpc-scale galaxy properties. Further, they demonstrate that SN feedback disrupts the spatial correlation of GMCs on scales > 0.2 kpc, which is relevant to our discussion on core formation later on. In addition, the SMUGGLE has been further refined with the development of a state-of-the-art model for the treatment of radiation fields, dust physics, molecular chemistry, and metal cooling by [139]. This model is able to produce a more complex picture of the ISM of galaxies while maintaining consistent global properties, such as SFR.

4.2.1 The SMUGGLE ISM Model

In this work, we implement the standard SMUGGLE model as described in [181]. Here we summarize the main physical modeling choices. The primary processes include gravitational

hydrodynamics, which is solved by AREPO [258], gas heating and cooling which produce an emergent multiphase ISM, the stochastic formation of star particles, and feedback from stars and SNe.

Heating and cooling

One of the biggest differences in SMUGGLE compared to previously implemented ISM models in AREPO [e.g. 260, 279, 213] is its ability to explicitly model a cold gas phase with temperatures falling below $T_{gas} \sim 10^4$ K. First, a primordial mix of Hydrogen and Helium is modeled by a network of two-body processes including collisions, recombination, Compton cooling via CMB photons [130], and UV-background photoionization [80].

Cooling has two main regimes, metal-line cooling driving the gas temperature down to the warm phase ($T_{gas} \sim 10^4$ K) – which was included in previous ISM models – while fine structure and molecular cooling implemented in SMUGGLE allows the gas to further cool to $T \sim 10$ K. Cooling rates are calculated in a UV background with the [127] fit as a function of temperature, metallicity, gas density, and redshift, with self-shielding taken into account at $z \leq 6$ as in [218]. The calculated rates are then scaled to the metallicity of the gas cell. By default, metallicities are updated self-consistently as the simulation evolves in AREPO. However, for idealized set-ups metallicity can be fixed to offset the lack of replenishment of pristine gas from cosmological infall. For simplicity, in this paper we fix the metallicity of our idealized runs to the solar value.

Star formation

Star particles representing single stellar populations with a [43] initial mass function are formed probabilistically in cold, dense gas. Gas is determined to be eligible for star formation based on several criteria. The first is the gas density threshold, below which no gas can be converted into a

star particle. SMUGGLE adopts a value of 100 cm^{-3}, in line with observations of giant molecular clouds [82]. Star formation is also restricted to gravitationally self-bound regions [see 127]. Additionally, star formation rates may be computed according to the H_2 fraction, though it is usually ~ 1 in sufficiently dense gas.

The probability of an eligible gas cell to be turned into stars is determined via $\dot{M}_\star = \varepsilon_{\rm sf}\ M_{\rm gas}/t_{\rm dyn}$, where $t_{\rm dyn}$ is the gravitational dynamical time of the gas and $\dot{M}_\star$ its star formation rate. In its default mode, the local SF efficiency parameter $\varepsilon_{\rm sf}$ is assigned a value of 0.01 to match the low efficiencies measured in observations [253], although [127] showed that the exact level of feedback-regulated star formation is independent of $\varepsilon_{\rm sf}$. We explore in Section 4.4 the effect of $\varepsilon_{\rm sf}$ on our SMUGGLE simulations.

The star formation timescale, defined as $t_{\rm sfr} = M_{\rm gas}\ /\ \dot{M}_\star$, can be parameterized in the variable efficiency model via Eqn. 4.1 below [205, 243], where α is the virial parameter, representing the ability of a cell to resist gravitational collapse through thermal support and gas pressure.

$$t_{\rm sfr} = \frac{M_{\rm gas}}{\dot{M}_\star} \min\Big(\exp\left(1.6\sqrt{\alpha/1.35}\right), 10^{30} \Big) \tag{4.1}$$

This model prioritizes star formation efficiency in highly dense regions. In Section 4.4.1, we investigate both a variable efficiency model, and one that maximizes the local star formation efficiency. Note that since $t_{\rm sfr} = t_{\rm dyn}/\varepsilon_{\rm sf} = M_{\rm gas}/\dot{M}_\star$, a parameterization on $t_{\rm sfr}$ is equivalent to a parameterization of the efficiency $\varepsilon_{\rm sf}$, all other quantities being the same for a given cell.

Feedback

Stellar feedback is modeled locally according to several sources including stellar winds, radiation from young stars and supernovae (SNe). Stellar winds due to massive OB and AGB stars contribute to the mass return to the ISM and are taken into account during the pre-processing of the gas. Cumulative mass loss from OB stars, as well as energy and momentum returned from both OB and AGB stars are determined via the parameterizations presented in [127], while AGB wind mass transfer is given by [278]. All of which are then injected with corresponding metallicity to the surrounding gas in the rest frame of the star. Stellar winds are a continuous process, and are thus treated continuously across each time step for each star particle.

Radiative feedback from young stars change the ionization, thermal, and dynamical state of the ISM, pre-processing the media where later SNe will go off. `SMUGGLE` includes a treatment of photoionization aimed at capturing the formation of HII regions by young, massive stars. Ionizing photon rates from young stellar particles are calculated by choosing a mass-to-light ratio and average ionizing photon ($> 13.6\,\mathrm{eV}$) energy to correspond with a $T = 4 \times 10^4\,\mathrm{K}$ blackbody spectrum, consistent with OB type stars. The number of available photons in a given timestep is used to stochastically photoionize neighboring gas cells after accounting for the expected number of recombinations. Photoionized cells are then updated to be fully ionized and placed at a temperature $T = 1.7 \times 10^4\,\mathrm{K}$. In addition to photoionization, young stars exert radiation pressure on neighboring gas cells, which is calculated according to their optical depth and position within the kernel. Multiple IR scattering is included, by assuming an average opacity $\tau = 10\,Z/Z_\odot\,\mathrm{cm^2\,g^{-1}}$ [127]. In the regime of small mass galaxies explored here, photoionization is expected to dominate among the radiation effects on the ISM, lowering the density of gas in the neighborhood of massive stars [229, 127].

Lastly, we stochastically model the injection of energy and momentum by discrete SN events onto neighbouring gas cells. It is important to note that SMUGGLE resolves individual SN explosions, and as such, the injected rates of energy and momentum are not continuous. The temporal distribution of individual Type Ia events is found by integrating the delay time distribution, which accounts for the approximate lifespan of an 8 $M_\odot$ main sequence star, with rates and energetics consistent with observations [110] as well as previous implementations in Arepo [278], with each event releasing the same mass of ejecta [269]. The total number of Type II SNe is found by integrating the Chabrier IMF of each stellar particle. If necessary, we account for PdV work in the (unresolved) Sedov-Taylor phase by applying a momentum boost to match the terminal momentum per SN, which depends primarily on local density and metallicity [e.g. 48]. Energy and momentum are distributed to surrounding gas cells following a kernel weighting and a maximum coupling radius, as described in detail in [181].

Variations on the fiducial SMUGGLE model

We will explore in Section 4.4 the effect of changing some of the default choices in SMUGGLE and how this affects the formation of dark matter cores and the properties of our simulated dwarfs. The changes will be inspired by results presented previously in the literature, including [220, 18, 22]. More specifically, we choose to vary the star formation gas density threshold $\rho_{\rm th}$ and the local star formation efficiency $\varepsilon_{\rm sf}$.

Table 4.1 summarizes our runs, which include the fiducial SMUGGLE run, SH03, and three variations on SMUGGLE as discussed in Section 4.4.1: (i) `rho0.1`, using a reduced star formation density threshold of $\rho_{\rm th} = 0.1$ cm^{-3}; (ii) `eSF100`, which maximizes the local star formation efficiency

Name	$r_{\rm core}$ [pc]	α	$M_\star$ [$M_\odot$]	Model description
`SMUGGLE / fiducial`	431.3	−0.13	7.76×10^7 $M_\odot$	default `SMUGGLE` model
SH03	160.2	−0.52	4.29×10^7 $M_\odot$	[260] model
`rho0.1`	324.2	−0.05	9.69×10^7 $M_\odot$	`SMUGGLE` with reduced gas density threshold, $\rho_{\rm th} = 0.1$ cm^{-3}
`eSF100`	490.7	−0.03	8.39×10^7 $M_\odot$	`SMUGGLE` with maximized local SF efficiency, $\varepsilon_{\rm sf} = 1$
`vareff`	528.3	−0.03	9.12×10^7 $M_\odot$	`SMUGGLE` with the variable efficiency model, see Sec. 4.2.1

Table 4.1: List of simulations used in this study. All initial conditions were generated according to [259] and run for 2 Gyr h^{-1}, where we take $h = 0.7$. Our standard resolution initializes a 2.17×10^{10} $M_\odot$ halo with 3×10^7 dark matter particles, and 10^6 gas particles, corresponding to a baryonic mass per cell of ~850 $M_\odot$ and DM mass per cell of ~7200 $M_\odot$. We adopt a gravitational force softening of $\epsilon = 16$ pc for all particle types. Also listed are the core radius (measured as described in Section 4.3.1), inner DM power law slope α, and stellar mass formed (i.e. not including the disk & bulge from initial conditions), all taken at final time.

to 100 per cent, $\varepsilon_{\rm sf}$= 1; and (iii) `vareff`, a variable efficiency model which chooses a value between $\varepsilon_{\rm sf}$ = 0.01 and $\varepsilon_{\rm sf}$ = 1 depending on the density of the surrounding ISM. The fiducial `SMUGGLE` model implements these parameters with values of $\rho_{\rm th}$ = 100 cm^{-3} and $\varepsilon_{\rm sf}$ = 0.01.

4.2.2 The Springel and Hernquist Model

In addition to the fiducial `SMUGGLE` model, we run a simulation with the SH03 model [260], which forms the basis for the ISM treatments in Illustris [279, 277], Auriga [106] simulations, EAGLE [242], APOSTLE [239], HorizonAGN [67], SIMBA [52], and others. The SH03 model, also run with the Arepo gravity and hydrodynamics solver, uses an equation of state treatment of cold gas modelled with a two-fluid approach (cold clouds embedded in a lower density hot gas bath) to describe the gas physics. This approach, which has been demonstrated to be successful at modeling the kpc-scale properties of galaxies, has been found to not form dark matter cores [282, 22].

We explicitly include stellar winds in the SH03 run with the wind velocity calculated directly from the energy and momentum summation of all SN in a given timescale and independent of halo properties. This is different from, for instance, the Illustris or Auriga projects, where the wind velocity is scaled to the dark matter velocity dispersion of the subhalo. Although such scheme is *de-facto* closer to the scalings expected for momentum-driven winds [193] and shown to more accurately reproduce some galaxy and CGM observables [e.g. 53], we choose a simpler wind model where no pre-assumptions are made with respect to the properties of the host halo, in an attempt to establish a fairer comparison with the `SMUGGLE` runs where no input information is required about the galaxy host. Ultimately, the impact of the exact modeling of the winds in our SH03 run is subdominant to the differences imprinted by the modeling of the ISM itself. As is the case in Illustris, Auriga, and other projects mentioned above, the wind particles in the SH03 model are

artificially decoupled from the hydrodynamics for a short period of time, while such a treatment is not necessary in our new SMUGGLE prescription where outflows naturally arise from the kinematics and thermodynamics of stellar winds and SN explosions.

4.2.3 Isolated Galaxy Setup

Throughout this paper, we analyze simulations run with different ISM models applied to the same initial conditions (ICs). We initialize an isolated, idealized dwarf galaxy with $M_{200\mathrm{m}} = 2.17 \times 10^{10}\,\mathrm{M}_\odot$ using the method outlined in [259]. The distribution of dark matter is initialized according to a Hernquist profile [120],

$$\rho_{\mathrm{dm}}(r) = \frac{M_{\mathrm{dm}}}{2\pi}\frac{a}{r(r+a)^3}\,, \tag{4.2}$$

where a is a concentration-dependent scale length. This model is identical to the widely used NFW profile [196] at small radii ($\rho \propto r^{-1}$), while the power law exponent differs at large radii: $\rho_{\mathrm{NFW}} \propto r^{-3}$ versus $\rho_{\mathrm{Hernquist}} \propto r^{-4}$. Both models have been shown to accurately describe the distribution of DM for halos in a cosmological context.

The galaxy itself is initialized with an exponential disk of scale length h for both stars and gas, in addition to a spherical stellar bulge modeled by the Hernquist profile. See Section 2 of [259] for more details on the model galaxy setup. We choose parameters for our model galaxy consistent with the 'Dwarf/SMC' setup described in [124], which gives a DM dominated dwarf galaxy similar to the pre-infall Small Magellanic Cloud with total baryonic mass $M_{\mathrm{bary}} = 8.9 \times 10^8\ \mathrm{M}_\odot$, gaseous disk with $M_{\mathrm{gas}} = 7.5 \times 10^8\ \mathrm{M}_\odot$, and DM halo with $M_{200} = 2 \times 10^{10}\ \mathrm{M}_\odot$ and concentration parameter $c = 15$.

The partitioning of cells in the initial conditions is done by setting the number of gas particles, $N_{\rm gas}$, with $N_{\rm DM} = 30N_{\rm gas}$, $N_{\rm disk} = 0.2N_{\rm gas}$, and $N_{\rm bulge} = 0.02N_{\rm gas}$. For the runs analyzed herein, we choose $N_{\rm gas} = 10^6$, resulting in a particle mass of $m_{\rm bary} \approx 850\ {\rm M}_\odot$. We choose the same value of gravitational softening for all particle types, with $\epsilon = 16$ pc. We have also run a set of simulations with an order of magnitude lower resolution ($N_{\rm gas} = 10^5, \epsilon = 32$ pc) for convergence testing. We find excellent agreement between the two resolution levels tested, as shown in Figure B.1 in the Appendix.

4.3 Forming Dark Matter cores in SMUGGLE

We explore the evolution of the dark matter density profile in our simulated dwarf galaxy in Figure 4.2, where each panel corresponds to different times, as labeled. The results of the default `SMUGGLE` model are shown in the solid black line, which demonstrates a clear flattening in the inner regions corresponding to the formation of a dark matter core in our initially cuspy halo. For reference, we include the initial dark matter distribution in each panel with a solid gray line.

4.3.1 A consistent method for core size measurements

Caveats & numerical effects

Figure 4.2 shows density profiles for various runs implementing the same ICs. We find the best fit NFW profile to the outer ($r > r_{\rm fit} = 3$ kpc) dark matter distribution. The bottom panels in Figure 4.2 show the ratio between the analytic NFW fit and the measured DM density in the fiducial `SMUGGLE` simulations (solid black lines). Although in the outskirts the simulated profiles are very well described by the NFW fits ($\rho_{\rm NFW}/\rho_{\rm dm} \sim 1$), in the inner regions the analytic profile clearly

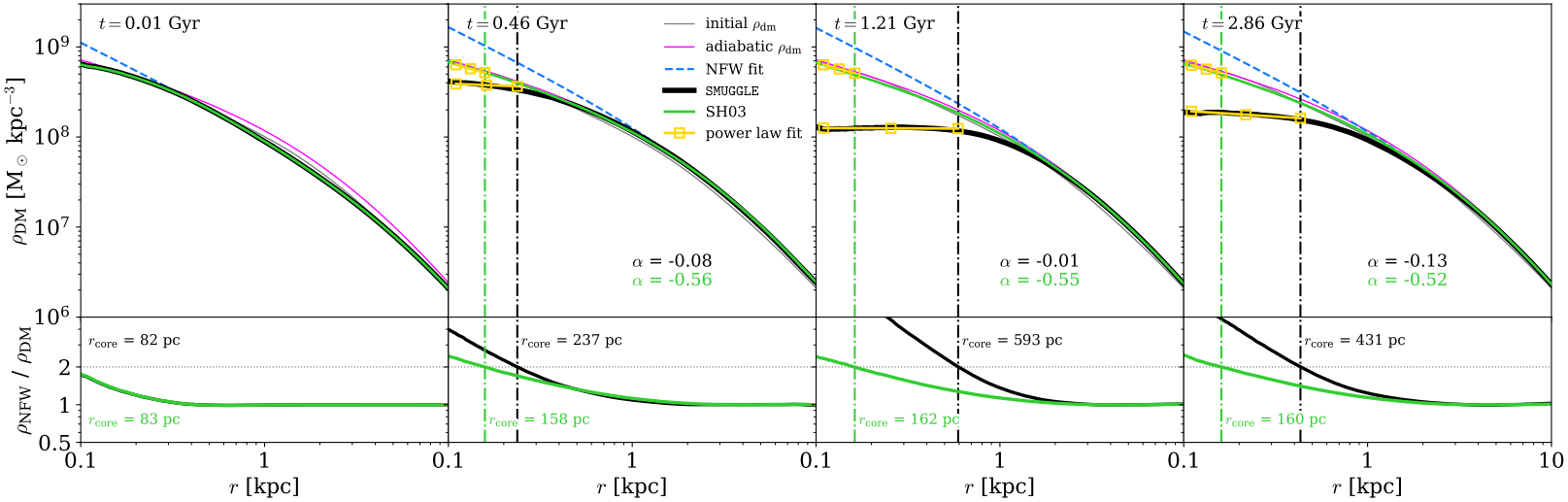

Figure 4.2: Dark matter density profiles of the isolated dwarf galaxy run with the fiducial SMUGGLE feedback model (black) and the SH03 feedback model (green) at selected times. The top row shows the DM density at each labeled time. Light grey lines represent the DM density profiles at $t = 0$, and the blue dashed line is the NFW profile fit to $r > 3$ kpc to account for variations in the inner region. The core radius $r_{\rm core}$ is defined as the radius where $\rho_{\rm NFW} / \rho_{\rm DM} = 2$, and which can be seen in the bottom panels, including the horizontal line at 2. The vertical dashed-dot lines in each panel represented our measured $r_{\rm core}$, which consistently capture the changes in DM density. In addition, power law slopes ($\rho \propto r^{\alpha}$) are shown in yellow, and are fit for $r_{\rm DM}^{\rm conv} < r < r_{\rm core}$. Values for the convergence radius $r_{\rm DM}^{\rm conv}$ are typically around 50 pc.

overestimates the dark matter density in all cases. This is partially due to adiabatic contraction, demonstrated by the magenta line. In the case of SH03, feedback is not capable of producing further changes in the DM distribution, resulting in a profile almost identical to the adiabatic run, while the SMUGGLE model is able to produce an extended region of constant density by later times. Additionally, the shape of the galaxy can affect the resultant DM distribution. In the case of disks, this can lead to shallower central profiles [35].

Additionally, we note that numerical effects can spuriously transfer kinetic energy between particles of different masses, such as our gas and DM particles [171]. A thorough investigation of the effects of gravitational softening and 'numerical feedback' have been presented in [169, 170]. While we adopt softening on the order suggested by [275] – approximately three times lower than the convergence radius $r_{\rm dm}^{\rm conv}$ – it is possible that spurious energy transfer between DM and baryonic particles via 2-body interactions contributes to the observed halo expansion. However, our tests are designed to isolate the effects of feedback. Numerical effects will be present in all our simulations, including the adiabatic and SH03 runs, but the methods of feedback coupling to the ISM vary. As such, our claims are about the differential effects between feedback implementations, not predictions of the absolute core sizes expected within dwarf galaxies in a cosmological context.

Core size measurement

Following [18], we define $r_{\rm core}$ as the location where the simulated dark matter density is a factor of 2 lower than the extrapolated best-fit NFW profile, $\rho_{\rm NFW}/\rho_{\rm dm} = 2$. However, we note that the authors compare against a low-threshold run rather than an NFW. Hydrodynamic relaxation may lead to a difference in predicted core radius. The measured $r_{\rm core}$ is indicated with a vertical dashed line and listed in the lower panels.

This definition is robust to variations on $r_{\rm fit}$ in the range $1-10$ kpc (see Figure B.4 in the Appendix). Figure 4.2 shows that the density profile within $r_{\rm core}$ for the fiducial SMUGGLE run is nearly flat at later times. We quantify this by finding the slope α of a power-law fit to the dark matter density between the convergence radius $r_{\rm dm}^{\rm conv}$ and $r_{\rm core}$, where $r_{\rm dm}^{\rm conv}$ is defined as the radius containing 200 DM particles [as in 147, 127], and is typically around 50 pc in size. For reference, the measured slopes α are quoted in each panel.

While the initial DM distributions of our simulations follow a Hernquist profile, we find no difference in measured core radius when using Hernquist or NFW parameterizations, consistent with the intended similarity between the fits for $r \ll r_{200}$. While some choices of our methodology are arbitrary, we find that it consistently produces an accurate characterization of the physical extent and slope of the constant density inner regions. We show in the Appendix that core formation is well converged and robust to numerical choices, such as resolution and $r_{\rm fit}$ (see Figs. B.1 and B.4).

4.3.2 Halo response to SMUGGLE versus SH03 models

Interestingly, and in contrast to previous results of model implementations within Arepo [e.g. 180, 47, 22], we find that the new SMUGGLE model develops a well-defined constant-density core with radius $200-600$ pc in our idealized $M_{200} \sim 10^{10}\,{\rm M}_{\odot}$ dwarf halo. In comparison, the same initial setup run with the SH03 model does not robustly form a core.

In practice, our method suggests $r_{\rm core} \approx 175$ pc (see bottom panels) for the SH03 run, although this is more consistent with a relaxation effect than a true dark matter core achieved by repeated perturbation of the potential. This is further supported by the inner slope α, which is far from being a flat constant density distribution ($\alpha \sim 0$) as found for our fiducial SMUGGLE run and instead remains steep ($\alpha \sim -0.55$), consistent with that of the initial condition over a similar distance

range. In addition, we have run an adiabatic (i.e. no star formation or feedback) version of the same initial setup for $t \sim 0.7\,\mathrm{Gyr}$. By our methods, we calculate time-averaged values of $r_{\mathrm{core}} = 150\,\mathrm{pc}$ and $\alpha = -0.57$ for the adiabatic run, indicating that the behavior seen in SH03 is consistent with relaxation and is not representative of a feedback-induced core. Note the similarity between the green SH03 and magenta adiabatic curves in Figure 4.2.

We therefore find that the SH03 ISM treatment does not create a core, in agreement with previous studies implementing similar models [e.g. 180, 22] while the new ISM treatment SMUGGLE results in clear halo expansion. The measured core extends over several hundred pc, which is well beyond the gravitational softening for the dark matter $\epsilon = 16\,\mathrm{pc}$ or the convergence radius $r_{\mathrm{DM}}^{\mathrm{conv}} \approx 50\,\mathrm{pc}$.

A more detailed description of the time evolution for the core is shown in the panels (a) and (b) of Figure 4.3, showing the core radius r_{core} and the power law slope α of the inner region $r_{\mathrm{conv}}^{\mathrm{DM}} < r < r_{\mathrm{core}}$ of the dark matter density profile. In SMUGGLE, the core radius grows during the first Gyr, after which it settles on an average $r_{\mathrm{core}} \sim 400\,\mathrm{pc}$ with fluctuations. The slope flattens from $\alpha = -0.55$ to -0.09 in the first half Gyr, where it remains for the rest of the simulation. In contrast, SH03 relaxes into a stable density distribution with $r_{\mathrm{core}} \sim 160\,\mathrm{pc}$ and no significant change in slope, resulting in a cusp rather than a core.

Panel (c) of Figure 4.3 compares the star formation histories in the SMUGGLE and SH03 runs. The rapid fluctuations in the SMUGGLE run are sustained throughout the $\sim 3\,\mathrm{Gyr}$ of run time, though with decreased burstiness after $t \sim 1\,\mathrm{Gyr}$. This contrasts the smoother SFR from the SH03 ISM model. In fact, SH03 shows a declining SFR, likely due to the lack of cold inflows and depletion of all eligible star forming gas. The cooling implementation of SH03 results in an effective

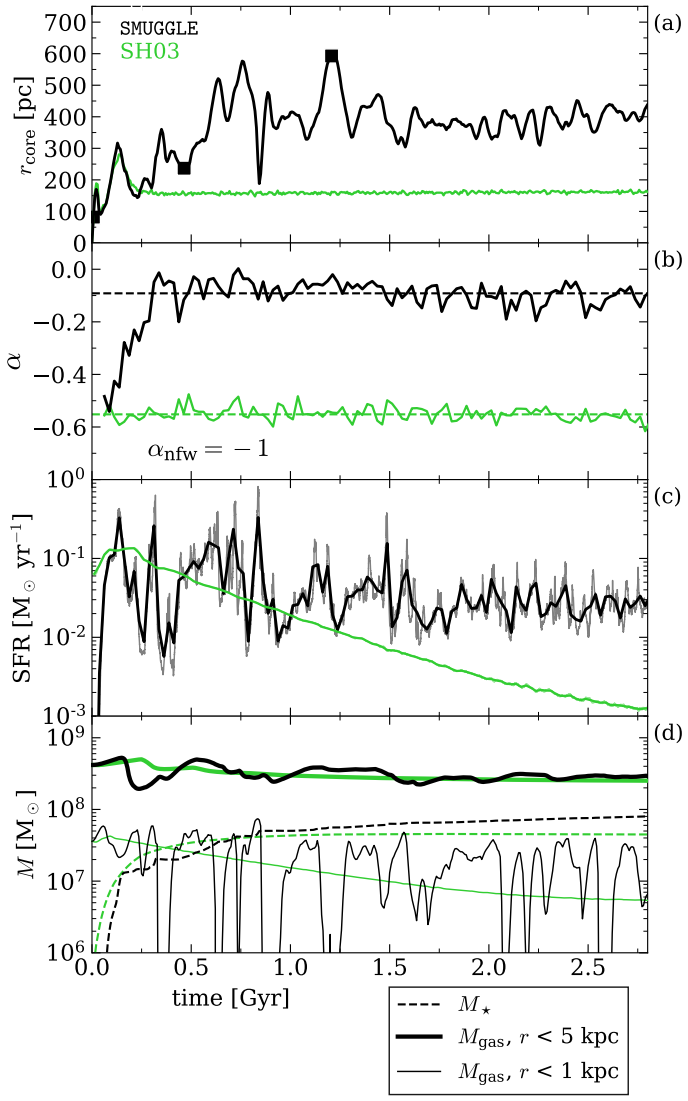

Figure 4.3: Time-evolving properties of the simulated isolated dwarf galaxy run with the fiducial SMUGGLE model in black and the SH03 feedback model in green. (*a*) Measured core radius $r_{\rm core}$ versus time. Black squares indicate timestamps of density profiles shown in Figure 4.2. See text for definition of $r_{\rm core}$. (*b*) Power law slopes α fitted to $r_{\rm DM}^{\rm conv} < r < r_{\rm core}$, binned with Δt = 25 Myr. Dashed lines indicate the average slope for $t > 0.5$ Gyr to account for initial relaxation effects. The SMUGGLE model results in a very flat inner profile ($\alpha \sim -0.1$) which extends over a larger portion of the galaxy with $r_{\rm core} \sim$ 400 pc, in contrast to the steeper ($\alpha \sim -0.6$), more concentrated ($r_{\rm core} \sim$ 150 pc) profile formed by SH03. (*c*) Star formation rate (SFR) versus time. The SFR is smoothed over Δt = 25 Myr bins. We find that `fiducial` produces a substantially burstier star formation history (SFH) than SH03, and that the average magnitude of SFR for SH03 agrees with that of `fiducial` in early times, but declines to much smaller levels after $t \approx 1.5$ Gyr. (*d*) Stellar mass ($M_\star$, dashed), gas mass within $r < 5$ kpc (solid, thick), and gas mass within $r < 1$ kpc (solid, thin). SMUGGLE results in frequent and significant changes in gas mass in the inner regions, while the gas mass < 1 kpc in SH03 smoothly decreases.

temperature floor of $\sim 10^4$ K, such that, with the lack of cold inflows, no new gas is able to condense to sufficiently high densities to fuel star formation. As a result, the final stellar mass formed in SMUGGLE is $\sim 50\%$ larger compared to SH03.

Note that this burstiness in the star formation of SMUGGLE is associated to fluctuations on the gas mass in the inner 1 kpc (Figure 4.3, panel d), while SH03 simply depletes the gas content in this region. As discussed in [214], such mass fluctuations in short timescales can cause the local gravitational potential to non-adiabatically change resulting in the expansion of dark matter orbits and, consequently, on the formation of a lower density core. In the case of SMUGGLE, although the gas content is changing very abruptly in the very inner regions (thin) and less so outwards, the mass fluctuation can be discerned quite far out into the main body of the galaxy, $r \sim 5\,\mathrm{kpc}$.

What is driving these differences between the ISM models? Discussions in the literature have cited rapid fluctuations of the potential in the inner regions [195, 214], burstiness of star formation rates [175, 44, 271, 69], and high gas densities such that it dominates the central potential [18]. These features are all present in the SMUGGLE treatment but not in the SH03-like models, explaining why core formation is achieved in SMUGGLE but not in previous ISM treatments in Arepo.

Figure 4.4 shows the time-averaged gas density distribution within 1 kpc for each run. This distribution is calculated with equal logarithmically spaced bins between $\rho_{\mathrm{gas}} = 10^{-6}\,\mathrm{cm}^{-3}$ and $\rho_{\mathrm{gas}} = 10^{6}\,\mathrm{cm}^{-3}$ at each snapshot. The median gas density is then calculated for each bin to construct the final gas density distribution, with standard deviation about the median shown as shaded regions.

As a result of the molecular cooling and other physics modeled in SMUGGLE, the typical gas densities achieved in SMUGGLE can be several orders of magnitude higher than in SH03. This run results in very few gas particles denser than $\rho = 1\,\mathrm{cm}^{-3}$ (green curve) while about half of

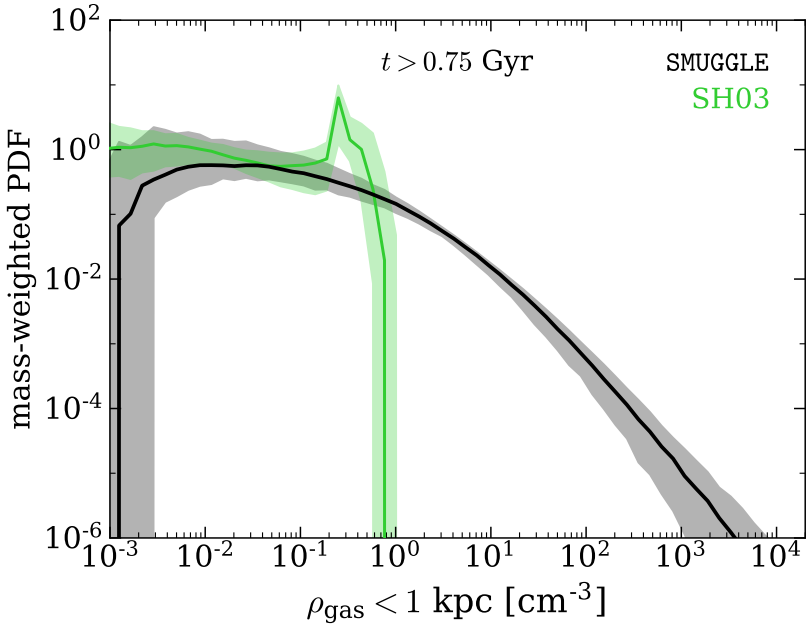

Figure 4.4: Median mass-weighted probability density function of gas density for $t > 0.75$ Gyr for the inner 1 kpc, with shaded regions representing the 68 per cent confidence interval in each ρ bin. The fiducial SMUGGLE run is able to achieve gas densities of $> 10^3$ cm^{-3}, while SH03 is unable to obtain densities > 1 cm^{-3}. The higher densities achieved by SMUGGLE allow its gas to gravitationally influence the DM to a stronger degree than in SH03.

the gas in the SMUGGLE run is above that threshold and up to $\sim 10^4$ cm^{-3}. The high gas densities achieved by SMUGGLE are instrumental in gravitationally perturbing the dark matter to create cores, while the wide range of densities reached in the inner 1 kpc indicates repeated disruption of dense gas from feedback in central star forming regions, maintaining a multi-phase nature that compares well with observations of real galaxies. While models based on an equation of state ISM treatment might be able to reproduce and predict statistical properties of galaxy populations as well as large-scale structure with remarkable success [e.g. 279, 180, 242, 239, 106, 213], they cannot capture the interplay between DM and baryons on small scales, where the contribution of baryons to the gravitational potential is significant.

4.4 The Effect of the ISM Model Parameters

4.4.1 Variations on SMUGGLE

In addition to the fiducial SMUGGLE model and SH03, we have run three simulations using the same initial conditions with variations on key parameters in the SMUGGLE ISM model: (i) rho0.1 reduces the star formation gas density threshold[1] from the fiducial value of $\rho_{\rm th}$ = 100 cm^{-3} to $\rho_{\rm th}$ = 0.1 cm^{-3} to mimic the value used in simulations such as SH03 and EAGLE [278, 50, respectively]; (ii) eSF100 increases the star formation efficiency from the fiducial value of $\varepsilon_{\rm sf}$ = 0.01 to $\varepsilon_{\rm sf}$ = 1 to compare with FIRE [127]; and (iii) vareff, which parameterizes $\varepsilon_{\rm sf}$ (see Section 4.2.1, Eqn 4.1) to maximize star formation in dense, self-gravitating gas clouds. Table 4.1 summarizes these runs and their key features.

Figure 4.5 shows time-dependent properties of the variations on SMUGGLE, with the original two runs shown in faded, thin lines. The core radius and slope are shown in Panels (a) and (b). We find that all SMUGGLE runs form clearly defined cores, with shallow slopes and core sizes larger than demonstrated in SH03. We find that time-averaged ($t > 0.75$ Gyr) values of $r_{\rm core}$ vary from $275 - 400$ pc in extent, with slopes of $\alpha = -0.07 \pm 0.06$. This is within the range of core sizes observed for dwarf galaxies in the literature, with typical values of $\alpha = -0.2 \pm 0.2$ [55, 199, 200].

We find variation between the different SMUGGLE runs. The low threshold rho0.1 forms the smallest $r_{\rm core}$, as expected, though much more of a robust core than the mild expansion seen in SH03. Interestingly, the high efficiency run eSF100 appears to form its core slower than fiducial, but ends up with a larger core by the final time. The variable efficiency run vareff forms its core

[1] The H_2 star formation requirement discussed in Section 4.2.1 was lifted to allow the density threshold to take full effect.

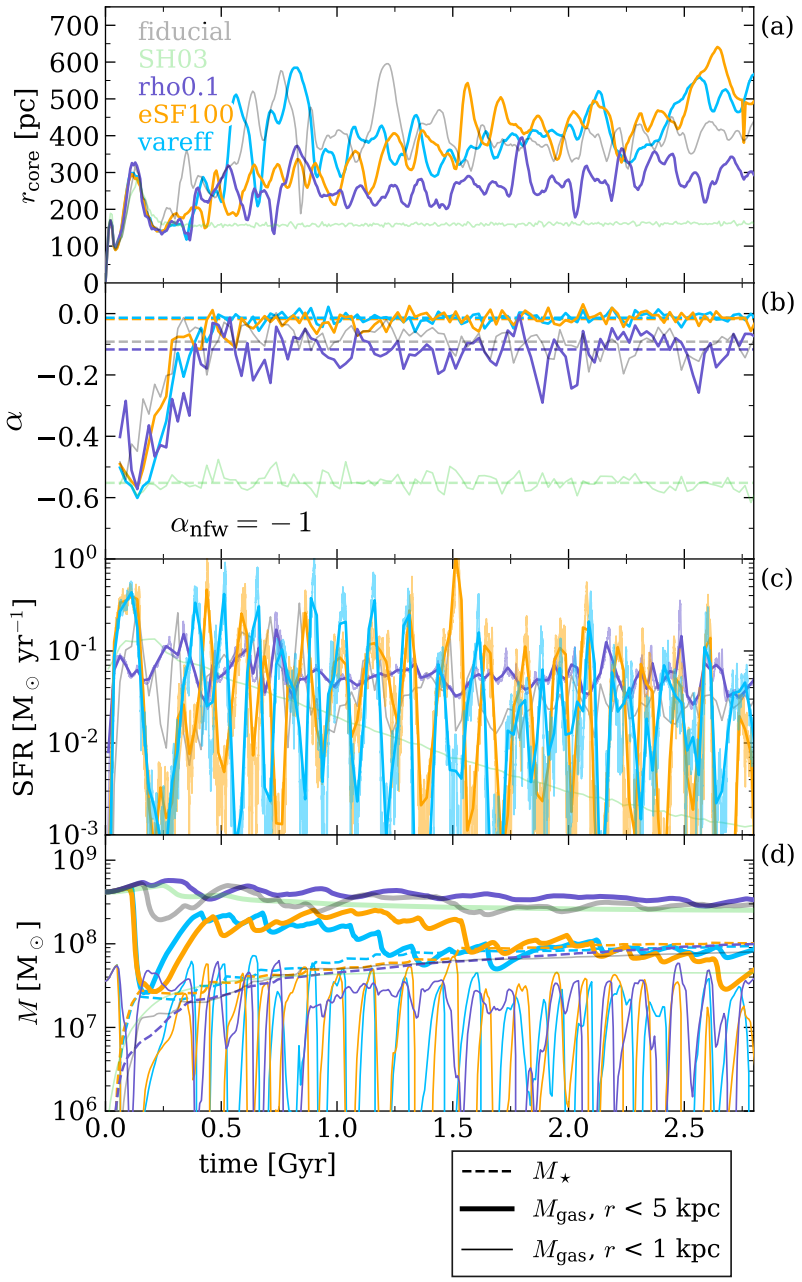

Figure 4.5: Select properties for `rho0.1` (purple), `eSF100` (orange), and `vareff` (blue), as in Figure 4.3, including faint lines for `fiducial` and SH03. All variations on the `SMUGGLE` model are able to form flattened DM cores between approximately 250–400 pc in extent and with $\alpha \sim -0.1$–0. `rho0.1` shows the least bursty SFR of the `SMUGGLE` runs, while both `eSF100` and `vareff` have SFRs that are significantly burstier than the fiducial `SMUGGLE` model. Remarkably, all `SMUGGLE` runs converge in $M_\star$ within ~20%, despite differences in SFR and gas content. The effect of different SFRs can be seen in the bottom panel as sharp jumps in $M_\star$ and decreases in $M_{\rm gas}$ (outflows), or the lack thereof. We see that the high efficiency runs undergo repeated outflows, slowly depleting their gas reserves, while `fiducial`, `rho0.1`, and SH03 retain a majority of their original gas content.

early on – similar to `fiducial` – but continues to grow at later times. These variations, however, are relatively minor. The primary distinction between the fiducial `SMUGGLE` model and its two increased efficiency variations appears to the continued growth of the core over time as a result of the sustained burstiness of their star formation. This is likely due to the increased energy injection into the ISM via the efficient star formation and SN feedback. That is, a much higher fraction of gas that is eligible to turn into star particles is converted. For contrast, the fiducial `SMUGGLE` model only turns ~ 1 per cent of the eligible gas into stars (on an average, not per-particle basis), in accordance with observations of GMCs [253]. These strong blow-outs represent a somewhat different, more violent mode of core formation than exhibited in the fiducial run, which experiences smaller, more frequent outbursts. Convergence among runs to universally shallow slopes is notable. However, we do still observe that the higher efficiency runs `eSF100` and `vareff` form slightly shallower cores with $\alpha \sim -0.03$, while `rho0.1` and `fiducial` form cores with $\alpha \sim -0.1$.

Panels (c) and (d) of Figure 4.5 show the SFR, stellar mass, and gas mass versus time for all runs. The SFRs we observe in the new `SMUGGLE` models are within expectation. The `rho0.1` run maintains a higher average SFR due to a lower $\rho_{\rm th}$, which effectively increases the amount of gas that is eligible for SF at any given timestep. Meanwhile, the higher efficiency runs see extremely bursty star formation histories due to a cycle of intense star formation, feedback that blows gas out of the inner regions, and re-accretion of gas to eligible SF densities. Despite these differences in star formation, we find excellent convergence in $M_\star$ for all `SMUGGLE` runs, with all runs reaching a final value within $\sim$20% of one another.

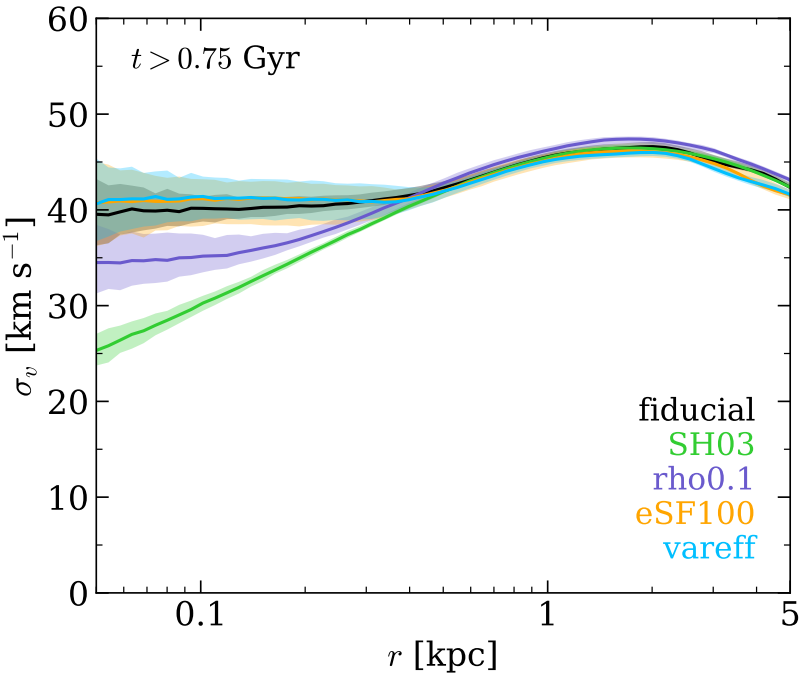

Figure 4.6: Time-averaged dark matter velocity dispersion profiles for each run. We find that the high efficiency variations on SMUGGLE approximately reproduce an isothermal (constant σ_v) core in the inner regions, while the SH03 run produces a decreasing profile similar to an NFW.

However, we do find differences in gas content and nature of outflows between these runs. We see that `rho0.1` retains more of its gas within 5 kpc than `fiducial` while also undergoing fewer and shallower outflows (seen as dips in the gas mass). In stark contrast, the highly efficient runs lose a majority of their initial gas content by the end of the simulation, undergoing frequent and larger outflows than either `rho0.1` or `fiducial`, retaining only ~20% of their original gas mass by t = 2.0 Gyrh^{-1}.

Figure 4.6 shows the DM velocity dispersion for all runs, averaged over the final 0.5 Gyr of the simulations. We find results roughly as expected: the velocity dispersion of SH03 is consistent with a cuspy NFW profile, while the SMUGGLE runs form ever-flatter inner profiles, approaching the constant-σ signature of an isothermal profile with the higher efficiency runs, as expected from

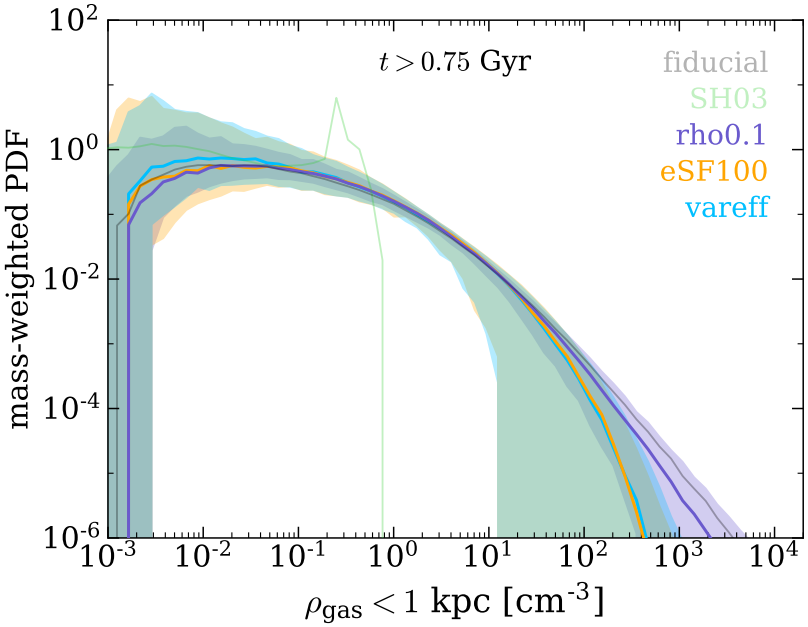

Figure 4.7: Median gas density distribution for each run over the run time of the simulation after t = 0.75 Gyr, with shaded regions representing the 68 per cent confidence interval in each ρ bin. Both `fiducial` and `rho0.1` are able to produce an ISM with a substantial fraction of the gas above their star formation thresholds, while the median gas densities achieved by `eSF100` and `vareff` demonstrate a more rapidly decreasing high density tail. This is a result of different star formation efficiencies: in the high efficiency runs, gas that reaches $\rho_{\rm th}$ is quickly turned into stars, while low efficiency preserves a component of highly dense gas.

self-interacting dark matter models [281, 226, 274, 34]. While it is interesting to see isothermal velocity dispersion profiles generated as a result of baryonic feedback, these results are not identical with expectation from SIDM. For example, profiles in SIDM are isothermal to much larger radii, then immediately decline, whereas the contribution from baryons results in a sizable bump at intermediate radii with a smoother tail. This may a possible avenue to distinguish SIDM from baryonic feedback [87]. Additionally, the isothermal profiles seen in the `SMUGGLE` runs demonstrate that they are not in dynamical equilibrium, an effect we discuss in Section 4.5.2.

As discussed previously, examining average gas densities can be a useful exercise to understand the behavior of both the DM and the baryons. Figure 4.7 shows the same time-averaged

gas density calculation as Figure 4.4, but for all runs, including shaded regions for standard deviations. Interestingly, we find that `rho0.1` is able to produce gas densities well above its star formation threshold of $\rho_{\rm th}$= 0.1 cm^{-3}, with an almost identical distribution to `fiducial`, though slightly favoring lower densities. In contrast, the runs with higher efficiencies (`eSF100` and `vareff`) are limited to gas densities at or near the standard value of $\rho_{\rm th}$ = 100 cm^{-3}, with slightly lower values in the fully efficient `eSF100` than in the selectively efficient `vareff`. The changes in the high-density tail between fiducial `SMUGGLE` model and `eSF100` are consistent with results from [165], who investigated the effects of this parameter on GMCs in MW-mass galaxies.

4.4.2 The role of modeling parameters

As discussed in Section 4.3, we find that the same isolated galaxy setup run with the SH03 feedback model [260] does not form cores due to its relatively low density gas and its lack of bursty star formation. It is generally claimed that these features are governed by the choice of $\rho_{\rm th}$ in the model [214, 22, 18], however, the clear differences between SH03 and `rho0.1`, both of which implement a low density threshold of $\rho_{\rm th}$ = 0.1 cm^{-3}, demonstrate that the physics of core formation is dependent on factors beyond this parameter.

The physical differences between these runs is clear: `rho0.1` has somewhat bursty star formation, dense gas, and SN-driven outflows of gas from the central regions, while SH03 has monotonically decreasing SFR, sparse gas, and no discernible feedback-driven outflows. If both runs implement $\rho_{\rm th}$ = 0.1 cm^{-3} yet achieve such different outcomes, other differences in subgrid physics must be to blame. The unstructured ISM of the SH03 feedback model is a result of its conception as a model for large-scale structure simulations, and is not particularly well suited for studying small-scale structures of galaxies and their halos, such as DM cores. The detailed ISM

model implemented in SMUGGLE is able to achieve much higher gas densities, resolving multiple physical gas phases at smaller scales, as well as achieving the bursty star formation necessary to form cores.

The difference in density achieved by these two runs (Figure 4.7) therefore points to two facts: (1) the physical gas density achieved by a simulation is not solely governed by $\rho_{\rm th}$, especially when using local star formation efficiencies lower than 100 per cent and (2) gas density and star formation burstiness (which drive outflows and subsequently core formation) are a product of the subgrid physics model as a holistic enterprise, including processes such as cooling physics and self-shielding, as well as resolution to the extent that such processes are resolution-dependent, rather than any individual parameter. However, changes in relevant parameters, as demonstrated here and in many other works, [e.g. 214, 18, , Burger et al. *in prep.*] do indeed produce observable differences within the same overall modeling scheme.

In their seminal work, [214] compare cosmological zoom simulations run with the SPH GASOLINE code [283, 264] run with two different value of $\rho_{\rm th}$, corresponding to our fiducial value of $\rho_{\rm th}$= 100 cm^{-3} and a low threshold run with $\rho_{\rm th}$= 0.1 cm^{-3}, as in our `rho0.1` run. They find that the low threshold run does not form a core, yet the high threshold run does, comparing the same overall ISM model in both cases. They point out that fluctuations in potential result in the expansion of the orbits of DM particles in the inner halo. We emphasize in this discussion that it is the ability of a model to create these physical density fluctuations that matters in producing DM cores.

As noted by [18], it is indeed surprising that few systematic tests of the star formation density threshold have been conducted by this time. The authors investigate the effect of a variety of values for $\rho_{\rm th}$ spanning 0.1 cm^{-3} up to 640 cm^{-3} for cosmological halos in the EAGLE simulations

[50]. They find that core formation is maximized for values between 1 cm^{-3} and 160 cm^{-3}, but find smaller cores for smaller values of ρ_{th} due to the lack of gravitationally dominant gas, and also for larger values due to the inefficiency of EAGLE's feedback model in this regime. They identify that core formation in dwarf galaxies is not sufficiently explained by either burstiness of star formation or strong outflows of gas within the EAGLE model. Instead, they point to features in the SFH of different halos that produce differences in outcomes of core sizes.

A similar investigation, though over a smaller range of threshold values, was conducted by [69, 68] for the NIHAO simulation project [286]. They find that, of their halos run with ρ_{th}= 0.1 cm^{-3}, 1 cm^{-3}, and 10 cm^{-3}, only those with ρ_{th}= 10 cm^{-3} and stellar mass to halo mass ratio of 0.1–1% underwent strong expansion, in agreement with the trend pointed out in [59]. Further, they identify that variability in star formation feedback must occur at sub-dynamical time-scales to produce expansion of the DM halo.

In the case of GASOLINE, a change in density threshold was able to predictably alter the outcome of core formation. The picture is somewhat more complex for EAGLE and NIHAO, which find that core formation, while increasing with ρ_{th}, is further dependent on SFH, timescale of burstiness, and halo mass, among other things. All these studies examined cosmological simulations. Our idealized numerical experiments seek to eliminate the complexities of cosmological runs, which produce substantial halo-to-halo variations in $M_\star/M_{200m}$, SFH, merger histories, gas fractions, etc. These are all important factors in understanding the diversity of observed galaxies, but can serve to obscure the impact of modeling choices.

Our idealized `SMUGGLE` runs produced cores for both the fiducial threshold of ρ_{th} = 100 cm^{-3} and the lowered threshold of ρ_{th} = 0.1 cm^{-3}, though `rho0.1` did produce a somewhat smaller

core radius ($\sim$ 300 pc, versus $\sim$ 400 pc for the fiducial run). When compared to the cuspy profiles of SH03, the core size within these two variations of SMUGGLE can be considered quite similar. This similarity in core size and shape between the two SMUGGLE variations makes sense in light of their achieved physical gas density distributions (Figure 4.7) versus the highly truncated distribution of SH03, which is incapable of producing $\rho_{\rm gas} \gtrsim 1 {\rm cm}^{-3}$. With an initial mean DM density of ~ 4 $m_{\rm p}{\rm cm}^{-3}$ within 1 kpc, it is clear that, even if SH03 produced fluctuations in gas mass within this region, it would be insufficient to perturb the DM potential.

Another factor that impacts the physics of core formation is the ability of the gravity solver to resolve the free-fall timescale of gas in the centermost star-forming regions of the galaxy. When larger softening lengths are used, the collapse of gas into dense clouds is delayed, and the resulting star formation process will be smoothed out. This leads to fewer discrete star formation events, and a reduction in both the burstiness of star formation and maximum gas density achieved in star forming regions, limiting the growth of cores.

We emphasize that it is the ability of a model to produce both sufficiently dense gas and sufficient variation in baryonic mass in the inner regions of a halo that will allow it to form cores. The ability of $\rho_{\rm th}$ to affect these physical phenomena depends (i) on how the chosen modeling prescriptions modulate the effect of that parameter on star formation, (ii) on how energy injection and dissipation distribute energy throughout the ISM, and (iii) on the interplay between resolution and all of the above. In short, the precise role of $\rho_{\rm th}$ in core formation is model-dependent. For example, SMUGGLE produces similar inner gas density distributions regardless of the adopted value of $\rho_{\rm th}$, and forms a feedback-induced core in all our explored variations. While the density threshold parameter is a commonly used parameter in ISM models, making it an appealing avenue for study,

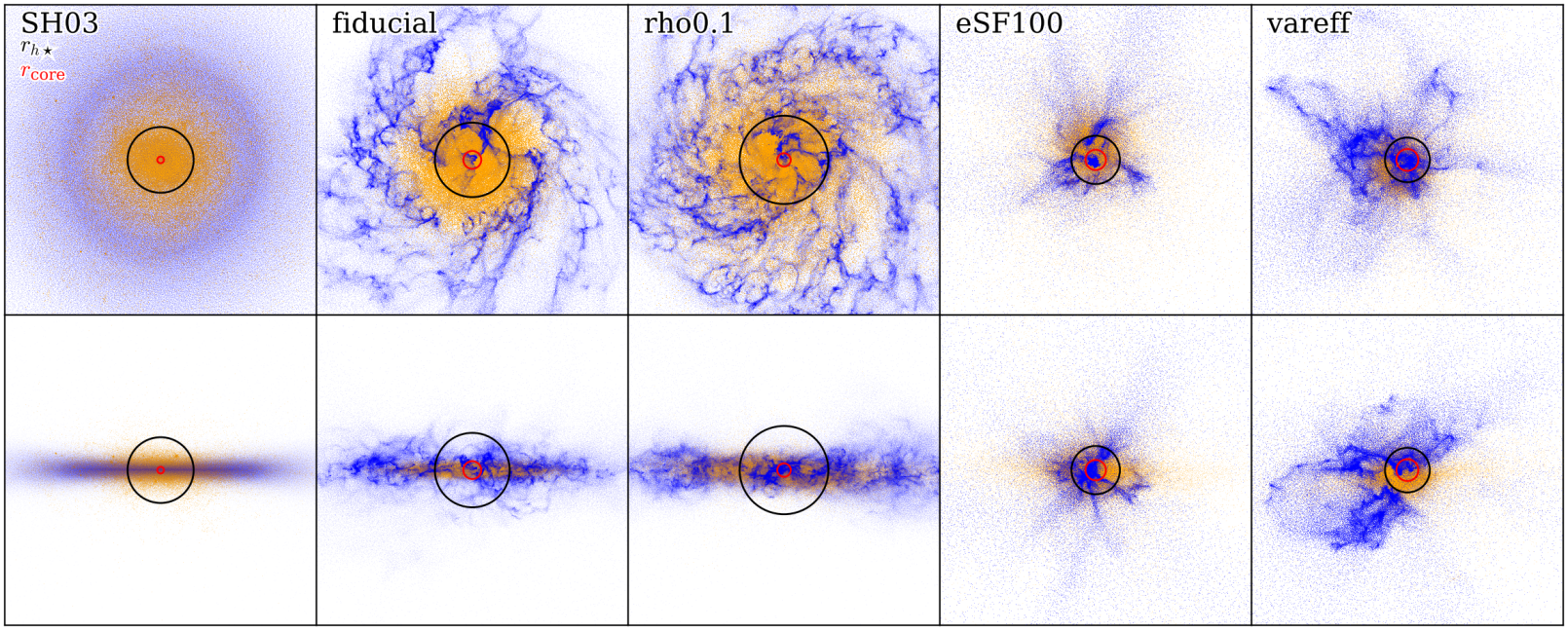

Figure 4.8: Face-on (top row) and edge-on (bottom row) projections of stars (orange) and gas (blue) for all runs. We only include star particles that were formed after the simulation began, not the old disk & bulge components from the initial condition. Each panel edge is 15 kpc in length, with the half stellar mass radius $r_{h\star}$shown in black (again, only new stars), and the core radius $r_{\rm core}$ shown in red. Both the fiducial run and `rho0.1` maintain fairly well behaved disks, though with somewhat more disturbance and fragmentation in `fiducial` as well as a more compact distribution of stars, while `rho0.1` has a more extended stellar distribution with a smaller core radius. Both `eSF100` and `vareff` show a highly disturbed ISM, with gas extending much further in the z-direction (perpendicular to the disk). Both galaxies have more compact stellar distributions than the fiducial run.

more attention must be given to the differences between modeling prescriptions with respect to their resulting physical properties (such as the gas density distribution and fluctuations in baryonic mass) before the effects of individual parameters can be understood in proper context.

For example, most treatments of star formation use relatively low values when implementing fixed local star formation efficiencies: $\varepsilon_{\rm sf}$= 0.01 − 0.1 [264, 286]. As in our `rho0.1`, the density threshold is therefore not necessarily an accurate tracer of the actual density achieved by the gas. The actual distribution of gas density will depend more complexly on modeling prescriptions (i.e. realistic versus effective cooling treatments) when using $\varepsilon_{\rm sf} \ll 1$. For this reason, comparing simulations run with distinct modeling treatments but similar $\rho_{\rm th}$ does not make sense when considering the dependence of core formation on $\rho_{\rm th}$, as the resulting distribution of gas density and its sensitivity to feedback can vary substantially between models.

4.5 Galaxy Structure

Figure 4.8 shows face-on and edge-on projections of the four alterations of the `SMUGGLE` model we consider, with the stellar half-mass radius ($r_{h\star}$) shown in green and $r_{\rm core}$ shown in magenta. The SH03 model shows a uniform disk with an unstructured ISM, along with large $r_{h\star}$ and small $r_{\rm core}$, while `fiducial` and `rho0.1` show a much more structured ISM, with clear fragmentation containing regions of both dense and rarefied gas. In addition, small pockets representing SN shock fronts can be seen in the face-on image. The disk remains well-behaved, with clear rotation and a roughly even distribution of gas throughout the disk. The ISM of `fiducial` is somewhat less evenly distributed than `rho0.1`, resulting in larger pockets of dense and rarefied gas, with an overall more centrally concentrated ISM (as seen in the edge-on projections), though it does maintain a

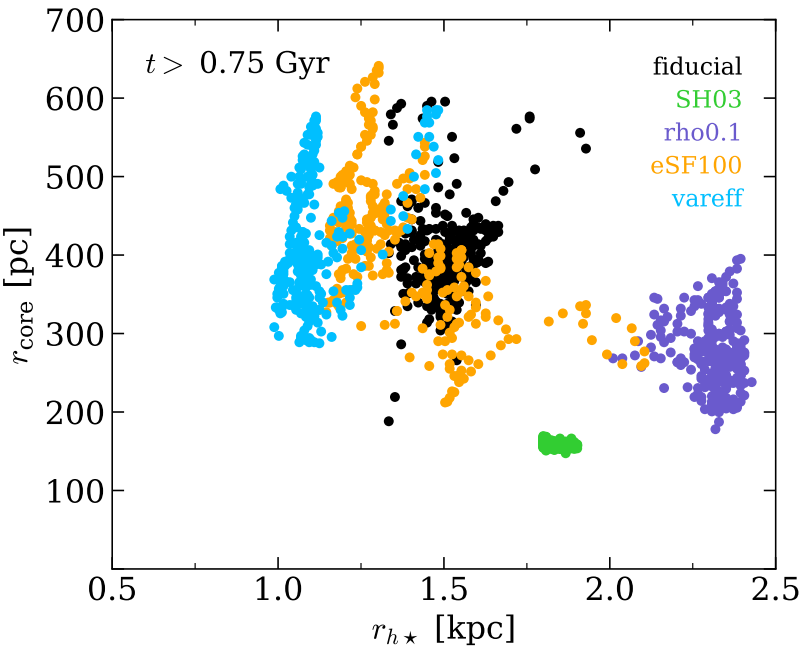

Figure 4.9: Core radius versus stellar half-mass radius for each run, with each point indicating a different snapshot after t = 0.75 Gyr. As in Figure 4.8, $r_{h\star}$ only includes star particles that were formed after the simulation began. Naturally, SH03 forms the tightest grouping, while the SMUGGLE runs are stratified according to galaxy size. It is a clear consequence of `vareff`'s prioritization of star formation in dense gas that it forms the most compact galaxy, while the global high efficiency of `eSF100` produces large fluctuations in galaxy size (and core radius). The low threshold of `rho0.1` allows for less dense gas in the outer regions to form stars, resulting in a more extended galaxy.

disk morphology with clear cohesive rotation. Conversely, both `eSF100` and `vareff` have highly disturbed gaseous components with no clear rotation and strong radial outflows from more energetic SN feedback. Even the edge-on projections show little traditional disk structure, with the galaxies appearing irregular in structure. In addition, they are much more compact, with $r_{h\star}$ roughly half the size of those of SH03 or `rho0.1`. The core radii of the three SMUGGLE models are larger than that of the SH03 model (as shown previously).

4.5.1 Morphology and cores

Figure 4.9 shows the core radius versus the half stellar mass radius for each run at $t > 0.75$ Gyr. We find a fair degree of stratification of the runs with $r_{h\star}$, indicating the effects of different modeling choices on galaxy structure. The variable efficiency run demonstrates the most compact galaxy size overall, mostly hovering aroung $r_{h\star} = 1$ kpc. This concentrated morphology is a result of the maximized star formation efficiency in dense regions (which tend to be near the center of the galaxy) used in this model. The globally maximized star formation efficiency in `eSF100` produces a more concentrated galaxy than the fiducial `SMUGGLE` model, though it also has more variation. This run experienced a large burst of star formation at early times, expanding the initial galaxy, only contracting at later times. This expansion and contraction is seen in the orange dots that extend to the right of $r_{h\star} = 1.5$ kpc, overlapping somewhat with our largest galaxy, `rho0.1`.

Interestingly, the large core sizes and compact galaxies seen in `eSF100` and `vareff` are contrary to the observed trend in which large cores are expected in low surface-brightness galaxies [238]. This may indicate that cores can form in high surface brightness galaxies, but have not yet been detected (either due to incompleteness or the disruption of gas kinematics in systems that may mimic these runs), or it may indicate that high star formation efficiency is not an empirically consistent modeling choice. The latter may be more likely, since most ISM treatments that calibrate this parameter to observed data choose values in the range 0.01 – 0.1 [264, 286], while models that implement such high efficiencies have other strict criteria on star formation [122]. Again, the effect of this parameter is indeed model-dependent. At least within `SMUGGLE`, an increased local SF efficiency parameter produces a trend counter to what is currently expected from observational data.

The large extent of `rho0.1` is a result of the reduced density threshold, which allows more rarefied gas in the outskirts of the galaxy to form stars, rather than concentrating star formation to the dense gas which collects near the center. The fiducial `SMUGGLE` model balances each of these effects, producing an intermediate-size galaxy, with $r_{h\star} \approx 1.5$ kpc throughout its evolution. Each `SMUGGLE` model produces variation in both the core size and stellar half-mass radius. The SH03 model on the other hand maintains the same core radius and galaxy size throughout its evolution, forming a tight cluster of points. We note again that SH03 did not form a robust feedback-induced core. We include the data here only for contrast with our `SMUGGLE` runs which did form robust cores.

The variation in both core size and half stellar mass radius is worth noting. Observed galaxies can effectively only be measured at one point in their evolution. While a large sample of observed galaxies helps to sample the variation, it is still impossible to take into account the variation in these properties over a given galaxy's lifetime. It is certainly possible that extreme values of inner DM density from highly overdense cusps to underdense cores represent local maxima or minima in their fluctuations. We emphasize that a given observation is not necessarily representative of the property's expectation value. Numerically constraining the predicted fluctuation in such properties like DM core sizes may be a worthwhile addition to the discussion on diversity of rotation curves.

To quantify differences in the kinematic structure between our runs, Figure 4.10 shows time-averaged (for $t > 0.75$ Gyr) stellar velocity dispersion profiles in cylindrical coordinates, with σ_R (radial direction) on the top panel, σ_ϕ (direction of disk rotation) in the center, and σ_z (direction perpendicular to the disk plane) on the bottom panel. We see that all four `SMUGGLE` runs have higher σ_R than SH03. The grouping of models echos that of their density distributions in Figure 4.7: `fiducial` and `rho0.1` have similar σ_R profiles, and smaller than both `eSF100` and `vareff`, which

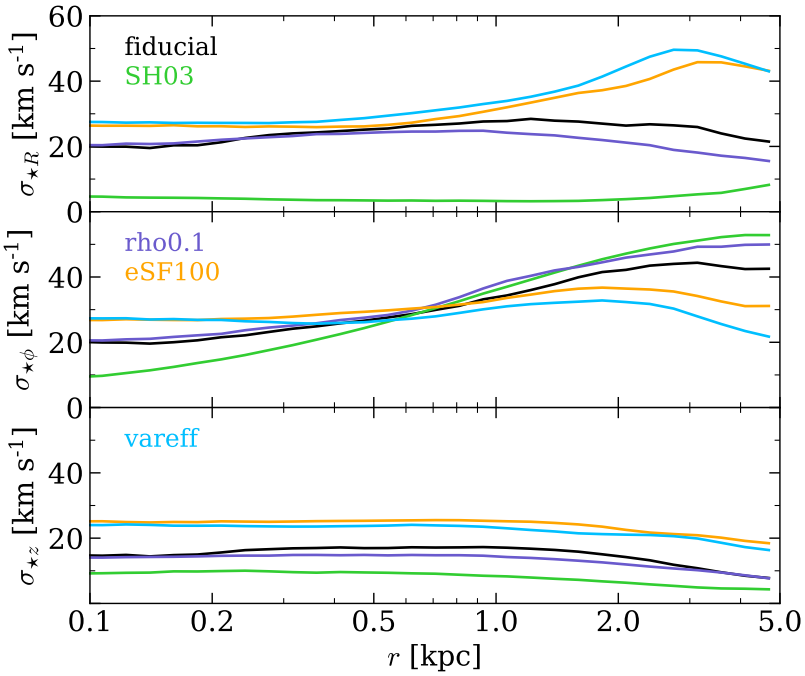

Figure 4.10: Time-averaged ($t > 0.75$ Gyr) stellar velocity dispersion $\sigma_\star$ profiles in cylindrical coordinates. Standard errors are shown but appear smaller than the width of the lines. We find that SH03 preserves disk coherence better than the SMUGGLE models, which all produce stronger feedback that disrupts the rotational structure of the galaxy. The high efficiency variations distribute stellar motion more evenly between all three cylindrical components, indicating a dispersion-dominated galactic structure.

are also similar to each other. This is a natural result of their higher star formation efficiencies, which results in stronger feedback, disturbing the ISM and causing increased radial motion into the gas due to increase SN activity. The center panel shows σ_ϕ, representing the rotation of the disk. Disks with coherent rotation exhibit a typical "S"-shaped curve, such as that of SH03, indicating a smooth increase in rotational velocity towards the outskirts of the galaxy. We see that `fiducial` and `rho0.1` exhibit this characteristic shape, but to a lesser degree as a result of their increased feedback. Naturally, the high efficiency models with their disrupted morphology show a near-constant σ_ϕ profile, indicating little to no rotational support. We observe a similar stratification of behavior in the bottom panel, where SH03 shows little gas motion in the z-direction, while `fiducial`

and rho0.1 show an increased amount, and eSF100 and vareff show a stronger increase in gas disruption in this direction as a result of the strong feedback that injects a large amount of momentum in the local radial direction, resulting in increased gas velocity dispersions in all directions. Due to the broad similarity in core formation between the four SMUGGLE runs, this implies that the choice of star formation efficiency has little impact on the dark matter content while drastically affecting the gas content and morphology of dwarf galaxies.

4.5.2 Diversity of rotation curves

Figure 4.11 shows the rotational velocity v_ϕ of the gas as well as $V_{\rm circ} = \sqrt{\mathrm{G}\mathrm{M}(<r)/r}$ for each run, averaged over the final 0.5 Gyr of each run. We find that the ISM of SH03 traces the potential of the galaxy remarkably well. In contrast, the high efficiency SMUGGLE runs eSF100 and vareff are so kinematically disrupted that there is little to no measurable rotation. [72] found similarly dispersion-supported gas in dwarf galaxies within the FIRE simulations [127], and that rotational support increases with increasing mass. Further, they find that the majority of FIRE galaxies across $6.3 < \log_{10}(M_\star/\mathrm{M}_\odot) < 11.1$ have little rotational support, and while the higher mass galaxies have morphological gas discs, only a fraction of the dwarf galaxies ($M_\star \lesssim 10^9$ $\mathrm{M}_\odot$) host this feature.

It is notable that even within the 'well-behaved' variations on SMUGGLE, we find that the rotational velocity of the gas does not accurately trace the $V_{\rm circ}$ implied by the gravitational potential. A naive reading of the gas v_ϕ distribution in Figure 4.11 could suggest a core radius of $\gtrsim$2 kpc for the fiducial SMUGGLE model and rho0.1, while our method of core size measurement relying only on DM density profiles (see Section 4.3) results in values of a few hundred parsecs. Interestingly, this 2 kpc figure is consistent with the fiducial radius used to compare well-resolved rotation curves

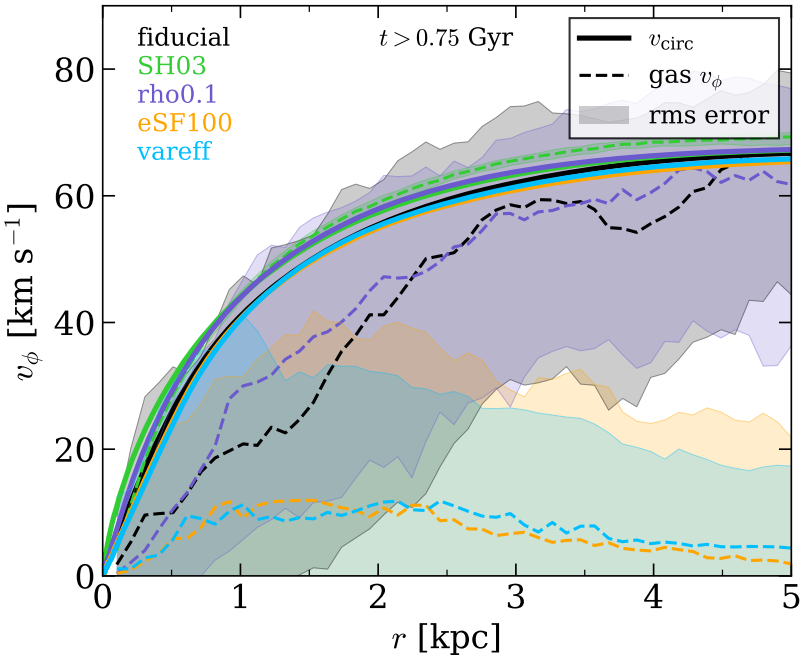

Figure 4.11: Median rotational velocity (v_ϕ) profile of gas (dashed line) and total circular velocity $V_{\rm circ} = \sqrt{{\rm GM}(<r)/r}$ (solid line). Shaded regions represent the 1σ deviation from median (inner 68 per cent confidence interval) within each r bin across time. We see that the (relatively) well-behaved ISM of `fiducial` and `rho0.1` trace the gravitational potential of the galaxy much better than the disturbed ISMs of `eSF100` and `vareff`. The large shaded errors indicate substantial variations in rotational velocity profiles over the course of the simulation.

between simulations and observations [as in 236, 202]. This result supports the notion that non-circular motion of gas in the inner regions of galaxies limits the ability of observational analyses to accurately recreate the DM profile, potentially contributing to the diversity of rotation curves in observed galaxies [203, 202, 238].

The variability in the v_ϕ distribution indicates another problem of time sampling bias. The measured gas rotational velocity is subject to frequent and substantial variation as a result of energy injection via feedback, as depicted by the shaded regions on Figure 4.11 representing the RMS error due to time-averaging. Measurements of the v_ϕ distribution taken at the extrema of the

error range could either produce rapidly rising rotation curves implying a mass distribution consistent with ΛCDM, or a slowly rising rotation curve implying an inner mass deficit and substantial core.

Figure B.3 in the Appendix plots the individual v_ϕ profiles for each snapshot of the fiducial SMUGGLE run over the final 0.5 Gyr. Here we see that, while the majority of rotation curves are below the actual DM $V_{\rm circ}$, there are a handful of profiles that demonstrate rotation speeds faster than the DM in the inner regions, i.e. profiles that would be interpreted as cuspy. Based on the number of snapshots with rotation curves that rise faster than an NFW, we place an upper limit on the presence of highly cuspy rotation curves at approximately 10 per cent. While this is an unlikely result, it indicates that cuspy profiles as a result of gas kinematics are indeed possible.

The discrepancy between the rotational velocity v_ϕ profile and the circular velocity profile $v_{\rm circ}$ indicates that the rotation of gas is rarely an accurate tracer of the DM potential in dwarf galaxies due to its sensitivity to energy injection via feedback. Our simulations predict that substantial diversity of rotation curves should be expected within the same dwarf galaxy across time. The variability of gas content and velocity in the inner regions of the galaxy on timescales $\lesssim$ 100 Myr poses a challenge to the assumption of virial equilibrium (i.e. 'steady-state') that underlies the inference of DM distributions from gas velocity profiles. As suggested by [220], expanding bubbles of HI can be used to identify post-starburst galaxies which are likely out of equilibrium. Collisionless stars may be a better tracer of the inner gravitational potential than gas.

Overall, SMUGGLE produces rotational profiles that systematically underestimate the DM content of the inner regions, consistent with previous attempts to reconcile the observed diversity of rotation curves with baryonic physics [203, 202, 220, 271, 236, 238]. This indicates either that our understanding of small-scale ISM physics within galaxies is incomplete, or that another mechanism

is responsible for creating rapidly rising rotation curves. It is possible that higher mass systems with stronger potentials are less susceptible to this effect, but we emphasize that this must be demonstrated explicitly rather than taken as an assumption.

The above considerations are only a result of ISM kinematics within an idealized, non-cosmological simulation and do not take into account additional bias introduced by observational measurement techniques, such as tilted-ring modeling and Jeans modeling, nor do they take into account evolutionary histories consistent with real galaxies or effects of cosmological environments such as mergers and infall of cold gas from filaments. Rather, these idealized tests isolate the effects of ISM modeling from other complex phenomena, allowing us to directly test the effects of baryonic feedback on the dark matter distribution of dwarf galaxies.

4.6 Summary & Conclusions

We study the behavior of the SMUGGLE [181] feedback and ISM model for the AREPO [258] moving mesh simulation code. In particular, we investigate the formation of dark matter 'cores' in idealized (non-cosmological) dwarf galaxies with $M_\star \approx 8{\times}10^7$ $M_\odot$ and $M_{200m} \approx 2{\times}10^{10}$ $M_\odot$ by comparing runs with identical initial conditions under both SMUGGLE and the SH03 model [260], a precursor to the model used in Illustris and Auriga [279, 106]. We develop a self-consistent method of measuring the core radius to track its evolution over time. We define the core radius to be the location where the actual DM density falls below the predicted DM density of an NFW profile fit to the outer regions of the halo ($r > 3$ kpc) by a factor or 2 (Figure 4.2). We then measure the slope of a power law fit to the resolved region within the measured core radius. Tracing these metrics over time, we find that SH03 does not produce a constant-density DM core, while the fiducial SMUGGLE

model creates a flattened core of radius $\sim$ 350 pc within the first 0.75 Gyr. We show that the origin of these cores is linked to the successful self-regulation of the star formation history in SMUGGLE which establishes a bursty star formation mode. These bursty cycles then create significant variations in the enclosed gas mass within 1 kpc, resulting in non-adiabatic expansion of the inner DM distribution. Contrary to the self-regulation seen in SMUGGLE, SH03 produces a steadily declining SFH, with a constant mass of gas reached after most of the originally eligible gas for star formation has been transformed into stars. This equilibrium state then preserves the steep inner density profiles that have been reported previously in the literature (Figure 4.3).

In addition, we run three simulations of identical initial set up including alterations to key feedback parameters: (i) `rho0.1` changes the star formation density threshold from the fiducial value of $\rho_{\rm th}$ = 100 cm^{-3} to a reduced value of $\rho_{\rm th}$ = 0.1 cm^{-3}; (ii) `eSF100` changes the local star formation efficiency (the mass fraction of eligible star forming gas that is converted into stars) from the fiducial value of $\varepsilon_{\rm sf}$ = 0.01 to an increased value of $\varepsilon_{\rm sf}$ = 1; and (iii) `vareff`, which implements a parameterization of the star formation efficiency based on the virial parameter (a measure of local self-gravitation; see Section 4.2.1). We find that the formation of a core is robust to these changes in SMUGGLE (though `rho0.1` does form a $\sim$ 25 per cent smaller core, and the high efficiency models exhibit stronger growth over time).

It is significant that `rho0.1` forms a feedback-induced core while SH03 does not. Since both implementations use the same star formation density threshold $\rho_{\rm th}$ = 0.1 cm^{-3}, this is an indication that the density threshold alone is not a good predictor of core formation for detailed ISM models such as SMUGGLE. It is important to note that while SH03 does not generate a core through feedback, it does experience a halo expansion due to relaxation effects and the influence of

the baryonic component [35]. Its expansion was smaller than in all SMUGGLE runs and was shown to be consistent with an adiabatic run, indicating that feedback was not a relevant factor. In contrast, rho0.1 demonstrates large fluctuations of baryonic matter in the inner regions of the halo, linking feedback to core formation.

We find that the ability to resolve dense gas ($\rho_{\rm gas} \gtrsim 10^2$ cm^{-3}; see Figure 4.7) is more predictive of core formation. For example, rho0.1 resolves gas up to $\rho \sim 10^4$ cm^{-3} while SH03 only resolves gas up to $\rho \sim 1$ cm^{-3}. This indicates that the SF density threshold is not a good proxy for actual gas density when using low local star formation efficiencies $\varepsilon_{\rm sf} \ll 1$. This then allows the dense gas to linger around and affect locally the gravitational potential even if the density threshold for star formation is nominally low. Note that this is different from predictions in other ISM implementations, such as NIHAO [69, 68].

Our high efficiency runs eSF100 and vareff have more bursty star formation than fiducial or rho0.1, yet they do not form substantially larger cores (Figure 4.5). This indicates that core size and burstiness are not tightly correlated, but that sufficiently bursty star formation, like sufficiently high gas density, are necessary conditions for core formation, as predicted previously [214, 18, 69]. All SMUGGLE variations also demonstrate mild time-dependence over the course of our runs, indicating that core expansion should continue over cosmological timescales. We hypothesize that the source of this continued expansion is the continued bursty star formation in these runs. The core evolution in the fiducial SMUGGLE run is inconclusive in its time-dependence due to the short runtime of these simulations. Density profiles of the SMUGGLE variations can be found in Figure B.2.

While there is broad agreement in core formation between the SMUGGLE variations, there are still differences between the models: rho0.1 forms the smallest core of the SMUGGLE models,

with $r_{\rm core}$~300 pc by final time, while `vareff` and `eSF100` reach final core radii of ~500 pc. Despite this difference, we maintain that `rho0.1` does indeed form a comparable core due to its highly flattened inner slope consistent with the fiducial `SMUGGLE` model. Interestingly, the fluctuations in gas mass within 1 kpc for all `SMUGGLE` runs are comparable (though with `rho0.1` having less frequent outflows). This is likely the source of the similarity in core sizes and shapes between the runs.

This similarity between variations of `SMUGGLE` indicates that the physical consequences of changing parameters such as the SF density threshold $\rho_{\rm th}$ are highly model dependent. As mentioned, $\rho_{\rm th}$ is not an accurate tracer of physical gas densities achieved by simulations when using empirically calibrated models that limit the local SF efficiency $\varepsilon_{\rm sf}$ to values $\ll 1$. Local gas densities will be highly dependent on implementations of subgrid physics. In particular, molecular and fine-structure cooling allows gas to naturally reach temperatures far lower than 10^4 K and achieve densities comparable to or higher than the average density of DM in the inner regions. The implemented modes of feedback-driven energy injection into the ISM allow this dense gas to be disrupted and flow to outer regions of the halo, repeatedly perturbing the DM potential as suggested by [214]. That is to say, changes in model parameters must result in the required physical changes within the simulation to accurately capture the details of baryon-induced core formation. Simulations that do not produce sufficiently dense gas (due either to modeling choices or resolution) are simply unable to produce the physics expected to affect core formation.

We also investigate the implications various modeling choices have on morphology. The fiducial `SMUGGLE` model and `rho0.1` both form rotationally supported disks with structured ISMs, while *SH03* naturally produces a stable galaxy with featureless ISM (see Figures 4.8 and 4.10). On

the other hand, the high efficiency models produce dispersion-dominated spheroid galaxies with lower gas fractions. This is a natural result of the increased burstiness and feedback of these models, and is in agreement with the FIRE simulations [127], which implement $\varepsilon_{\rm sf}$= 1 and also observe dwarf galaxies with spheroid morphology and dispersion supported ISM [72]. Interestingly, we find that the most compact galaxies (`eSF100` and `vareff`) form the largest cores, while the most diffuse galaxies (`rho0.1`) form the smallest cores (Figure 4.9), in agreement with [35]. However, this seems to be in contrast with the trend in observed galaxies [238]. Encouragingly, the trend with core sizes is weak with a high degree of scatter, allowing for the possibility that simulations may result in the expected trend when implemented cosmologically.

Our examination of the rotational velocity (v_ϕ) profiles of the gas content (Figure 4.11) indicates that the ISM does not trace the potential of the DM in the inner regions ($r < 2$ kpc). This is true for all `SMUGGLE` variations, though the fiducial model and `rho0.1` are better able to trace the DM $V_{\rm circ}$ in the outskirts, while `eSF100` and `vareff` demonstrate almost no rotational velocity component of the gas at any radius. Further, we find significant variations in the v_ϕ profiles across time, suggesting that a diverse morphology of rotation curves can be observed at different times within the same galaxy. We find that individual v_ϕ profiles can vary between exceeding the expected DM circular velocity and drastically underestimating it (Figure B.3). However, we find that the ISM in `SMUGGLE` systematically falls below the $V_{\rm circ}$ of the halo within the inner regions, consistent with previous work [238], further indicating that the baryon-induced core formation scheme struggles to reproduce the steep end of the diversity of rotation curves problem.

Our analysis indicates that feedback-induced core formation is fundamentally a small-scale problem. Its effects may be observed on the scale of a few kpc, but the physics which generates

these observables occur on the scales of star formation and feedback, i.e. $10 - 100$ pc, as well as sub-pc processes that are yet unresolved and only implemented through sub-grid modeling. Lack of cores in models which are not able (and do not attempt) to produce this microphysics is not evidence against the validity of baryon-induced core formation, but evidence against the suitability of such models to study this process.

Finally, our results suggest that even if perfect observations of gas rotation curves are obtained, these do not necessarily trace the DM potential in non-equilibrium systems such as dispersion-dominated dwarf galaxies. Caution is needed when attempting to infer DM distributions from gas rotation. It is important to investigate the assumption of equilibrium for dwarf galaxies, whose small sizes make them susceptible to large fluctuations in gas content and velocity. This preliminary work suggests that feedback-induced core formation is a highly complex problem that must be approached carefully.

Chapter 5

Conclusions

Dwarf galaxies are ideal laboratories in which to study the ΛCDM cosmological model as well as the physics of galaxy formation. We investigate the structure of DM halos, finding that isolated dwarf galaxies are able to expand their dark matter halos, leading to the formation of a 'core' by baryonic physics alone when sufficiently detailed ISM modeling is implemented. We also look into the abundance of dark and luminous substructure of dwarf galaxies similar to the Large Magellanic Cloud, finding that they preserve more of their subhalo population than MW-mass halos due to their shallower central potentials, and that they host a significant population of dwarf satellites, up to 7±2 with $M_\star \geq 10^4$ $M_\odot$. Finally, we investigate the formation of dwarf satellites around LMC-mass centrals, and find that they have similar star formation histories to satellites of Local Group or Milky Way like centrals, and that the quiescent fraction of LMC-satellites replicates the inverse relationship with stellar mass found elsewhere. We find that the significant gaseous halos of the hosts are capable of environmentally quenching intermediate-mass dwarf satellites, with host-satellite gravitational interactions producing tidal streams in a large fraction of systems.

5.1 Halo expansion in dwarf galaxies

We run idealized dwarf galaxies with $M_{\rm halo} = 10^{10}$ M$_\odot$ and $M_\star = 10^8$ M$_\odot$ using the Springel and Hernquist 2003 [SH03, 260] galaxy formation model, representing a classic approach similar to those used by numerous successful large-volume cosmological and zoom-in simulations, as well as with the SMUGGLE model [181], a newly developed, highly detailed galaxy formation model that implements numerous physical processes relevant to small-scale physics within galaxies. We find that, with the same initial conditions, the SMUGGLE model is able to produce dense gas and bursty star formation, leading to the expansion of the DM halo and the formation of a 'core' - an extended region of flat DM density in the inner region of the halo. Meanwhile, the SH03 model produces stable star formation rates, little gas fluctuation, and no DM core.

We further compare these runs to variations on the default SMUGGLE model. We implement a run with reduced star formation gas density threshold, `rho0.1`; a run with increased local star formation efficiency, `eSF100`; and a run with this efficiency parameterized according to the virial parameter, a measure of local self-gravitation, `vareff`. We find that all SMUGGLE models, including `rho0.1`, are able to form cores of similar (though not identical) size. The high efficiency models produce highly bursty star formation and large cores, while the SFRs of `rho0.1` are less bursty.

Notably, `rho0.1` is still able to produce significant and frequent fluctuations in the inner gas content, as well as gas densities comparable to the fiducial SMUGGLE model. This is in contrast to previous studies, which have found that gas density thresholds of this value are unable to produce cores. We suggest that this is because the role of $\rho_{\rm th}$ is model-dependent. SMUGGLE implements molecular and fine-structure cooling, as well as traces individual SN events. This allows gas to cool and condense to high densities before forming stars, which then inject large amounts of energy

locally into the ISM. This detailed ISM physics is capable of producing frequent and large variations in gas content within the inner regions of galaxies, which has been shown to produce cores [214].

Lastly, we compare the morphology and gas kinematics of our runs. SH03 produces a smooth ISM with a rotation-supported disk that shows little variation in thickness or deviation from equilibrium. The fiducial `SMUGGLE` model and `rho0.1` produce rotation-supported galaxies with structured ISMs, while the high efficiency models `eSF100` and `vareff` produce dispersion supported galaxies with low gas fractions. We find that in all `SMUGGLE` models, the rotational velocity profiles of their gas struggle to follow the DM potential as given by $v_{\rm circ} = \sqrt{GM(<R)/R}$. This indicates that the large fluctuations in gas content seen previously may disrupt the equilibrium required by circular velocity potential inference. Further, the gas rotational velocity profiles themselves demonstrate a large degree of variability across time, indicating that the diversity of rotation curves problem may be partially explained by the inconsistency of gas kinematics across time.

5.2 Substructure of LMC-mass hosts

We use cosmological zoom-in simulations of LMC-mass halos ($M_{200} \sim 10^{11}$ M$_\odot$) from the Feedback In Realistic Environments (FIRE) project [127] to investigate their dark and luminous substructure. By comparing to MW-mass halos from the same simulation suite, we find that LMC-mass halos destroy a significantly lower fraction of their dark subhalos. This is due to the reduced $M_\star/M_{200}$ ratio for these systems, as well as their cored density profiles. Both properties contribute to a shallower inner density slope than MW-mass halos. Since tidal forces are responsible for the gravitational stripping of mass from subhalos, destroying them in the process, we suggest that the shallower potential of LMC-mass centrals leads to the survival of a greater fraction of their subhalos.

We then investigate the luminous component of their satellite population, suggesting that LMC-mass halos should be host to an average of 7 ± 2 satellite galaxies with $M_\star \geq 10^4$ $M_\odot$. Using Gaia proper motions [90], and comparing to the simulated infall of observed Magellanic satellites from [232], we suggest that the motions of Carina and Fornax are consistent with co-infall into the MW halo with the LMC. Adding these to the previously confirmed list of Magellanic satellites [233, 138], the stellar mass function of simulated LMC-mass hosts from FIRE is highly consistent with the inferred stellar function of observed LMC satellites. We further predict that tidal processes from host-satellite interactions will have pre-processed LMC satellites prior to their infall into the MW, producing potentially observable signatures.

5.3 The effects of LMC-like environments

A similar suite of LMC-mass halos from the FIRE project were used to investigate the effects of environment on the evolution of satellite dwarf galaxies. We compare the star formation histories (SFHs) of LMC-satellites (referring to simulated satellites of LMC-mass systems, not actual satellites of the real LMC) to nearby centrals and find that LMC-satellites have a greater diversity of quenching times than the centrals, which are strongly bimodal (i.e. quenching very early or continuing to form stars). The quiescent fraction of LMC satellites follows the dependence on stellar mass seen in Local Group satellites. That is, a lower fraction of higher mass satellites are quenched, while low-mass satellites are universally quiescent below a certain cutoff. Beyond this, the SFHs of simulated LMC-satellites are highly consistent with the SFHs of simulated LG-satellites, suggesting that similar quenching mechanisms may be at play in systems at both scales.

Next, we identifed eight environmentally quenched satellites (EQSs) from our simulations. From this sample, we identify two subtypes: (i) low-mass, early-infalling satellites that quench prior to first pericenter with the host, with quenching timescales less than 1 Gyr and (ii) high-mass, late-infalling satellites that quench after first pericenter, and quenching timescales of $2-4$ Gyr. It is unclear yet whether these represent distinct subtypes, or if quenching behavior is a continuous trend with stellar mass. In all EQSs, gas content decreases dramatically very soon after their quenching times. We find that all LMC-mass hosts contain significant gaseous halos and hot coronas. These both indicate that satellite quenching is likely due to hydrodynamics (i.e. ram-pressure stripping) rather than gravitational effects such as the stripping of gas content or the prevention of fresh gas infall, which operate on longer timescales. Further, we explicitly check for ram-pressure stripping by visualizing the gas velocity field in the reference frame of satellites prior to and after their quenching times, indicating that ram pressure can operate independently or be aided by feedback, which 'loosens' gas from the gravitational potential of the satellite, allowing it to be more easily forced away by the ambient host halo gas.

The above predictions will allow our theories of cosmology and galaxy formation to be tested at smaller scales as next generation surveys [41, 134, 54, 66] produce more observational constraints on LMC-mass systems. Currently, they reveal the importance of model-dependent analysis when investigating core-formation, and that detailed baryonic feedback can produce diverse rotation curves. They further show that LMC-like systems have many similarities to, and many difference with, systems like our own MW. Much more work is needed in order to fully characterize the nature of galaxy formation and its interaction with dark matter on small scales.

Appendix A

Additional Information for Chapter 2

Here we include additional information relevant to the discussions above. We test the effects of resolution in our simulations by comparing the subhalos of `m11q` run at the 'high' and 'normal' resolutions as described in sub-section 2.2.2. We examine the subhalo $V_{\rm max}$ functions as described in sub-section 2.2.1 in Figure A.1 and the circular velocity profiles of subhalos with 8 km/s < $V_{\rm max}$ < 12 km/s as described in sub-section 2.4.3 in Figure A.2. We examine the radial distribution of subhalos in LMC-mass hosts and MW-mass hosts as described in sub-section 2.3.1 in Figure A.3. We include our observational data set as described in sub-section 2.4.1 in Table A.1, including stellar mass, galactocentric coordinates and radial velocities, distance to the LMC, as well as the current status of association to the LMC system.

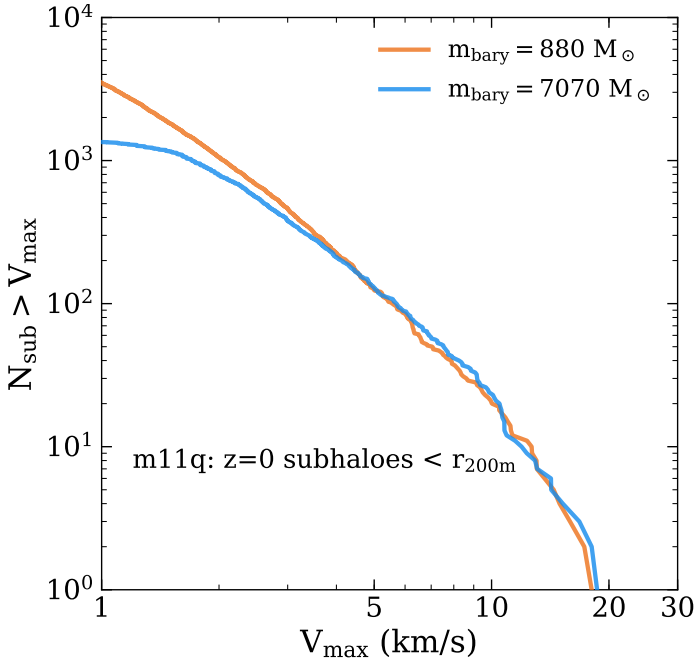

Figure A.1: Resolution convergence of the $z = 0$ subhalo population of `m11q` at two resolutions: $m_{\rm bary}$ = 7070 $M_\odot$ (blue) and $m_{\rm bary}$ = 880 $M_\odot$(orange). The populations diverge below the typical value (~4 km/s) used for our minimum subhalo $V_{\rm max}$ cutoff in Section 2.3, meaning the subhalo populations used in that analysis are well converged.

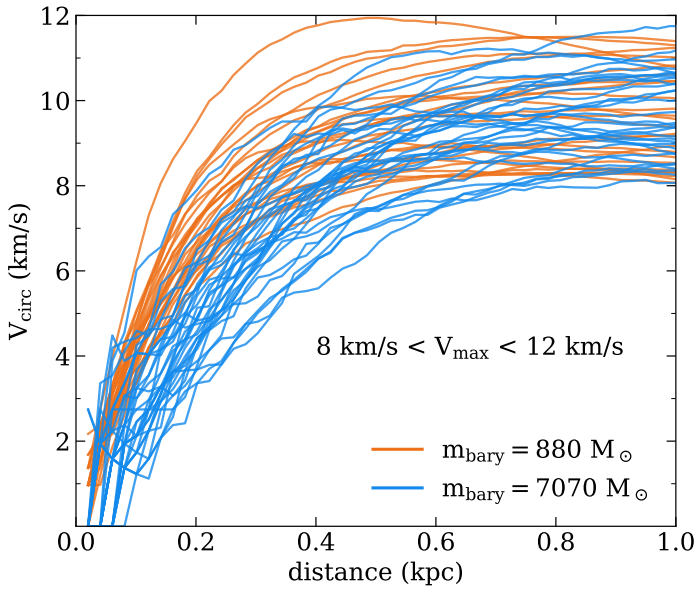

Figure A.2: Circular velocity profiles ($V_{\rm circ} = \sqrt{GM(<r)/r}$) of subhalos with 8 km/s < $V_{\rm max}$ < 12 km/s in `m11q` in high resolution ($m_{\rm bary}$ = 880 $M_\odot$, orange) and the lowest resolution included herein ($m_{\rm bary}$ = 7070 $M_\odot$, blue). The lower resolution run shows a systematic underdensity until convergence is reached at $r \sim 0.8$ kpc. Due to the integrated nature of these quantities, convergence in $V_{\rm max}$ occurs at much higher radii ($\sim$ 800 pc) than the nominal softening lengths ($\epsilon_{\rm DM} \sim 20 - 40$ pc). Distances at which ultrafaint circular velocities are measured are well below this convergence radius.

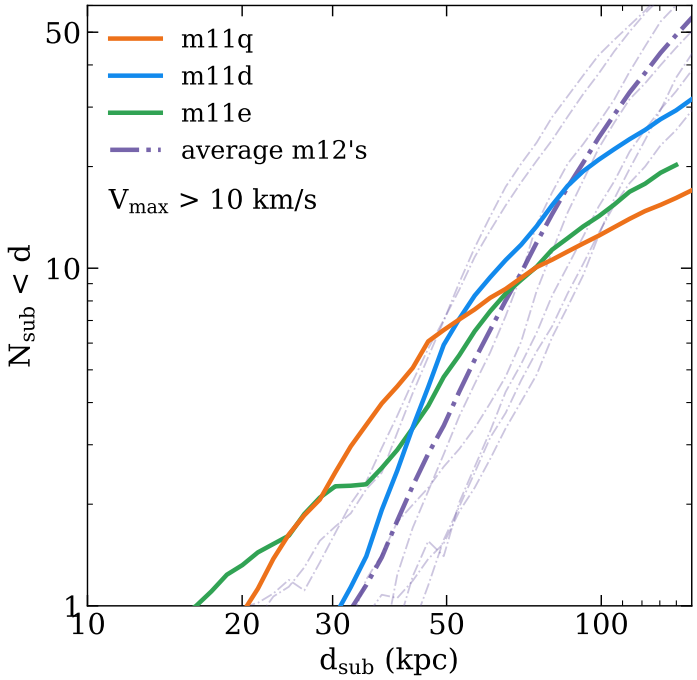

Figure A.3: The radial distribution of subhalos with V_{max} > 10 km/s around three LMC-mass hosts in FIRE (`m11q` - orange; `m11d` - `blue`; `m11e` - green) and averaged over seven MW-mass hosts in FIRE (purple dot-dash line), with all counts averaged over ~1.3 Gyr. We find that two of the three LMC-mass halos host substructure at significantly smaller distances than the MW-mass halos, with all hosting more total subhalos than the average MW-mass halo out to ~60 kpc. The existence of subhalos at closer distances to the central galaxy for LMC-mass hosts strengthens the plausibility of a detectable subhalo-galaxy interaction for hosts of this scale.

Name	$M_\star$ ($M_\odot$)	l (deg°)	b (deg°)	D_{MW} (kpc)	D_{LMC} (kpc)	V_{rad} (MW) (km s^{-1})	possible	confirmed
Antlia 2	4.30e5^{*,6}	264.9	11.2	124.2	145.4	49.6		
Bootes I	2.90e4	358.5[5]	63.3	68.3	98.7	120.4		
Canes Ven. I	2.30e5	74.3	79.8	218	254.1	78		
Carina	3.80e5	264.8[5]	-22.5	104	60.8	-13.8		this work
Car2	1.08e4*	270.0[1]	-17.1	36.2	25.3	211.4†		K18
Car3	1.56e3*	270.0[1]	-16.8	27.8	62.9	51.6†		K18
Cra2	3.26e5*	283.8[2]	42.0	116.9	114.5	-79.1†		
Draco	2.90e5	79.2[5]	34.3	77.2	125.8	-74.6		
Dra2	2.47e3*	98.3[1]	42.9	22.3[2]	125.4	-159†	K18	
Eri3	1.08e3[3]	274.3[2]	-59.6	87.1	48.2		S17	
Fornax	2.00e7	243.84[5]	-67.1	146.1	114.5	-38.2		this work
Hercules	3.70e4	28.7	36.9	126	158.5	145		
Hor1	3.92e3[3]	270.9[2]	-54.9	79.3	38.5	-30.4†		K18, S17
Hor2	1.88e3*	262.5[2]	-54.1	79	39.6		S17	
Hyd1	1.30e4*	304.5[1]	-16.5	27.6	28.4	-51.4†		K18
Hyd2	1.42e4[3]	295.6[2]	30.5	125.2	113.5	134.2†	K18	
Leo I	5.50e6	228.1[5]	50.1	250.5	263.7	159.6		
Leo II	7.40e5	223.7[5]	68.6	231.2	255.2	18.6		
LMC	1.50e9	290.2[5]	-32.5	51.8	0.0	43.4		
Phx2	2.25e3[3]	323.3[2]	-60.2	80.2	51.9		K18, S17	
Ret3[2]	2.00e3	273.9	-45.7	92	45.0		S17	
Sag2	2.06e4*	18.9[2]	-22.9	60.1	49.6			
Sculptor	2.30e6	318.6[5]	-80.2	86.7	65.6	77.0		
Sextans I	4.40e5	250.3	43.7	83.8	94.1	37.7		
SMC	4.60e8	309.4[5]	-41.8	66.2	23.2	-4.2		K18, S17
Tuc4[2]	2.20e3	313.3	-55.3	45.5	26.6		S17	
Tuc5[2]	5.00e2	316.3	-51.9	51.9	28.2		S17	
Ursa Minor	2.90e5	96.5[5]	45.6	75	125.4	-72.4		

Table A.1: Properties of dwarf galaxies near the Milky Way, selected as having either $M_\star > 3\times10^4$ $M_\odot$, or begin determined a potential LMC satellite by S17, K18, or this work. All units and coordinates are in the galactocentric frame. The columns 'possible' and 'confirmed' refer to the LMC association criteria established by [233, 'S17'] and [138, 'K18']. Galaxies determined to be consistent with the LMC system by our calculations of angular momenta (listed in Table 2.3) from Gaia DR2 data [90] are listed as 'this work.' Any $M_\star$ with a star marker (*) was calculated from the visual magnitude listed in K18 (except for Antlia 2, whose M_V was obtained from [272]) assuming a mass-to-light ratio of 2. Any V_r with a dagger (†) was converted from its originally tabulated heliocentric value in K18. Numbered superscripts refer to sources. Any row with no superscripts is from [185]. A superscript on the name of the galaxy means all properties came from that source. If a property has no superscript but there are others in its row, the nearest superscript to the left is its source. References: 1 - K18; 2 - S17; 3 - [81]; 4 - [151]; 5 - [90]; 6 - [272]

Appendix B

Additional Material for Chapter 4

To demonstrate the resolution convergence of the SMUGGLE model, Figure B.1 shows our standard high resolution run with $m_{\rm bary}$ = 850 $M_\odot$compared to a run at 10 times lower resolution ($m_{\rm bary}$ = 8500 $M_\odot$). We find good agreement in all measured quantities. The lower resolution run demonstrates marginally less bursty star formation rates. We also find stronger time dependence in the measured core radius and power law slope in the lower resolution run, but good agreement in values for these quantities across the run time. A notable similarity between the runs is their rapid fluctuations in gas mass within 1 kpc.

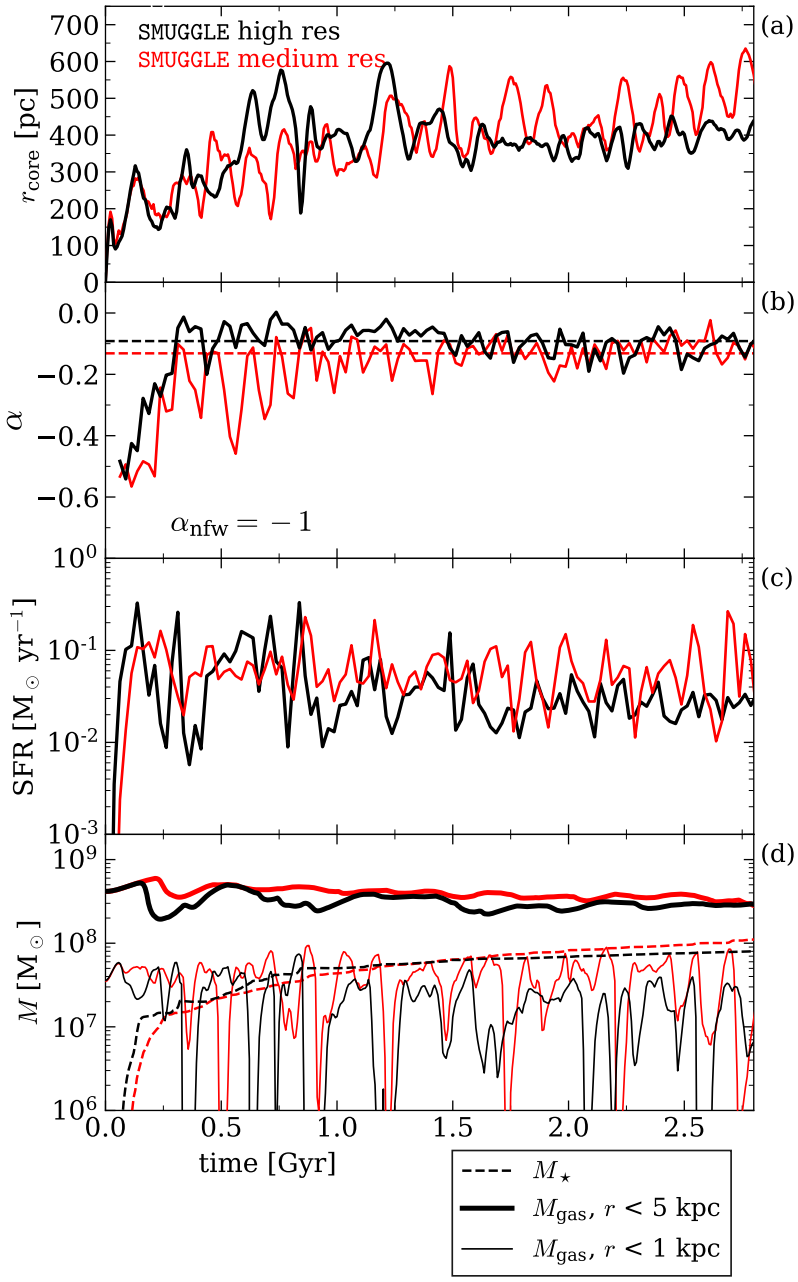

Figure B.1: Comparison between the fiducial SMUGGLE model ran at our presented resolution of $m_{\rm bary} = 850\ {\rm M}_\odot$ (high res), and at a 10× lower resolution of $m_{\rm bary} = 8500\ {\rm M}_\odot$ (medium res).

Figure B.2 depicts density profiles for the three SMUGGLE variations we explore in Section 4.4.1, similar to Figure 4.2. Each panel shows a different timestamp of the simulation, including the final snapshot in the rightmost panel. The bottom panels, as in Figure 4.2, show the ratio of densities of the fitted NFW profile to the physical DM density achieved in the simulation. The NFW profile is fitted to $r > 3$ kpc, and the core radius is chosen as the radial distance where $\rho_{\rm NFW} = 2\rho_{\rm dm}$. The core radius is depicted as a vertical dash-dot line, and its value at each timestamp is listed on the bottom panels. We find that eSF100 and vareff, models with increased local star formation efficiency, demonstrate large, flattened core. Our run with density threshold of $\rho = 0.1$ cm^{-3} (rho0.1), forms a core that is somewhat smaller than those of the high efficiency runs, though it is still consistent with the fiducial SMUGGLE model, and clearly distinct from the lack of core found in SH03, as discussed in Section 4.4.1.

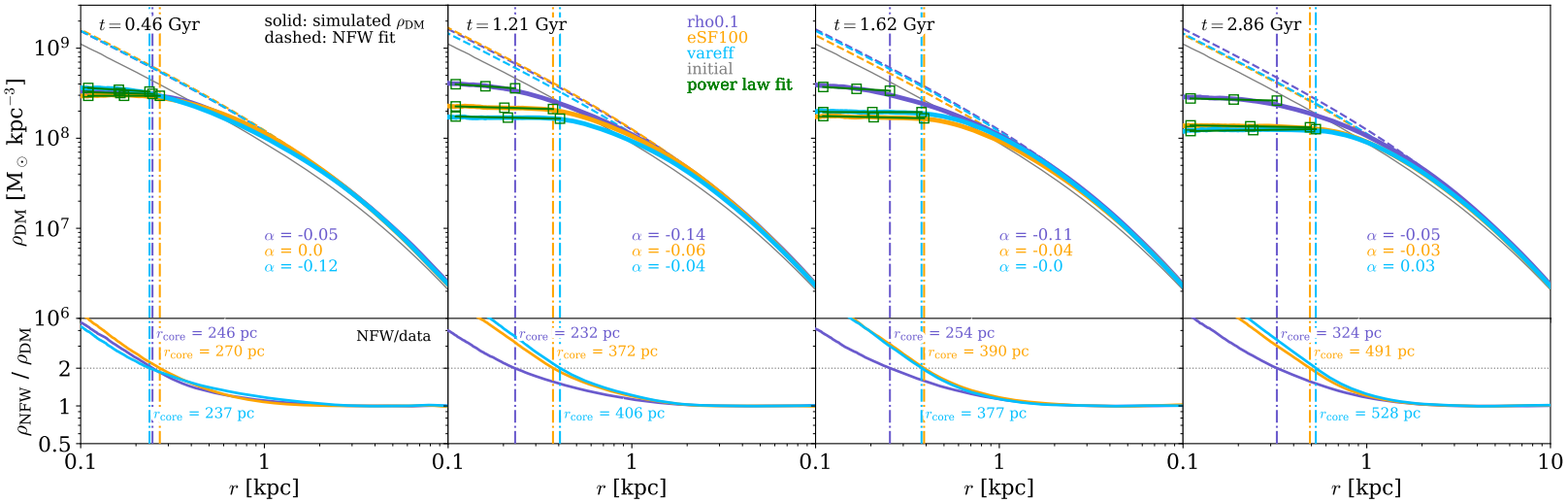

Figure B.2: Dark matter density profiles at select times for the runs with variations in the ISM model of SMUGGLE. Dashed lines indicate NFW profiles fit to the run of the corresponding color. Power law fits are shown as dark green square, and the core radius is indicated with a vertical line.

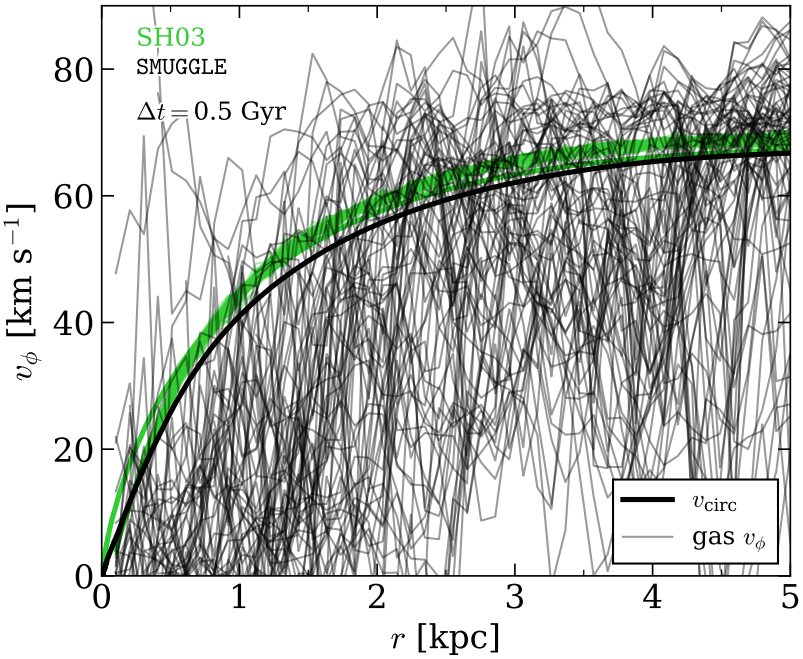

Figure B.3: Gas rotational velocity profiles of the fiducial SMUGGLE model for each snapshot in the last 0.5 Gyr of its run time. Realistic modeling of ISM physics produces large variation in the rotational component of gas within the galaxy, leading to a large diversity of rotation curves.

We plot the rotational velocity profiles of gas for both the fiducial SMUGGLE model and SH03 [260] for each snapshot of the final 0.5 Gyr of run time in Figure B.3. The median gas v_ϕ profile for all models is shown in Figure 4.11. We plot these individual profiles to explicitly show the variety of shapes that can be produced through feedback effects on the gas in SMUGGLE, and the uniformity of profiles achieved in SH03. We find that a handful of profiles (no more than 10 per cent) demonstrate steeply rising inner velocity profiles, suggesting that baryonic feedback can account for some of the observed diversity of rotation curves. Overall, we find rotational velocity profiles that tend to underestimate the circular velocity (thicker lines). These rotational profiles can also demonstrate strong fluctuations with radius, as well as time, indicating a gaseous component that is in a constant state of flux.

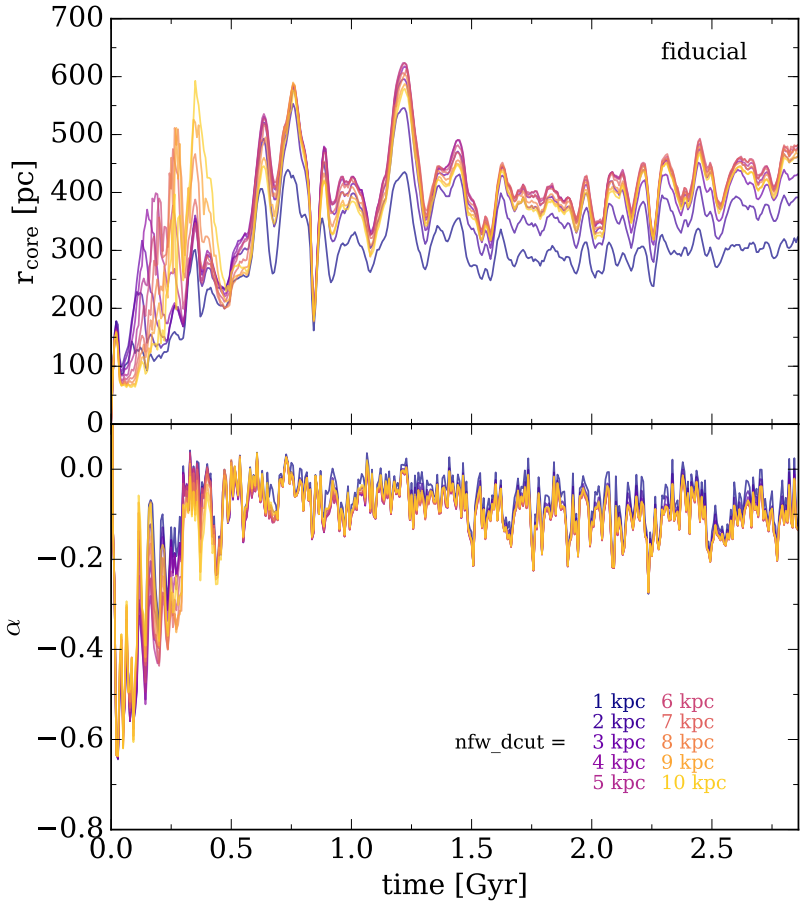

Figure B.4: Comparison of the core radius and slope measured using NFW reference profiles fit to $r >$ nfw_dcut, as listed on the figure. We find that our measurements are robust to choice of this parameter.

Figure B.4 shows the measured values of core radius and inner power law slope for the fiducial SMUGGLE model with different values of radial cutoff for the fitted NFW profile (see Section 4.3.1). We find that the measured values of $r_{\rm core}$ and inner slope α are robust to choice of NFW radial fitting cutoff in the range $1 - 10$ kpc.

Bibliography

[1] Mario G. Abadi, Ben Moore, and Richard G. Bower. Ram pressure stripping of spiral galaxies in clusters. *MNRAS*, 308(4):947–954, October 1999.

[2] Mario G. Abadi, Julio F. Navarro, and Matthias Steinmetz. Stars beyond galaxies: the origin of extended luminous haloes around galaxies. *MNRAS*, 365(3):747–758, January 2006.

[3] Mario G. Abadi, Julio F. Navarro, Matthias Steinmetz, and Vincent R. Eke. Simulations of Galaxy Formation in a Λ Cold Dark Matter Universe. I. Dynamical and Photometric Properties of a Simulated Disk Galaxy. *ApJ*, 591(2):499–514, Jul 2003.

[4] Joshua J. Adams, Joshua D. Simon, Maximilian H. Fabricius, Remco C. E. van den Bosch, John C. Barentine, Ralf Bender, Karl Gebhardt, Gary J. Hill, Jeremy D. Murphy, R. A. Swaters, Jens Thomas, and Glenn van de Ven. Dwarf Galaxy Dark Matter Density Profiles Inferred from Stellar and Gas Kinematics. *ApJ*, 789(1):63, July 2014.

[5] Hollis B. Akins, Charlotte R. Christensen, Alyson M. Brooks, Ferah Munshi, Elaad Applebaum, Anna Engelhardt, and Lucas Chamberland. Quenching Timescales of Dwarf Satellites around Milky Way-mass Hosts. *ApJ*, 909(2):139, March 2021.

[6] Elaad Applebaum, Alyson M. Brooks, Charlotte R. Christensen, Ferah Munshi, Thomas R. Quinn, Sijing Shen, and Michael Tremmel. Ultrafaint Dwarfs in a Milky Way Context: Introducing the Mint Condition DC Justice League Simulations. *ApJ*, 906(2):96, January 2021.

[7] I. K. Baldry, M. L. Balogh, R. G. Bower, K. Glazebrook, R. C. Nichol, S. P. Bamford, and T. Budavari. Galaxy bimodality versus stellar mass and environment. *MNRAS*, 373(2):469–483, December 2006.

[8] Michael L. Balogh, Ivan K. Baldry, Robert Nichol, Chris Miller, Richard Bower, and Karl Glazebrook. The Bimodal Galaxy Color Distribution: Dependence on Luminosity and Environment. *ApJ*, 615(2):L101–L104, November 2004.

[9] Steven P. Bamford, Robert C. Nichol, Ivan K. Baldry, Kate Land, Chris J. Lintott, Kevin Schawinski, Anže Slosar, Alexander S. Szalay, Daniel Thomas, Mehri Torki, Dan Andreescu, Edward M. Edmondson, Christopher J. Miller, Phil Murray, M. Jordan Raddick, and Jan Vandenberg. Galaxy Zoo: the dependence of morphology and colour on environment*. *MNRAS*, 393(4):1324–1352, March 2009.

[10] K. Bechtol, A. Drlica-Wagner, E. Balbinot, A. Pieres, J. D. Simon, B. Yanny, B. Santiago, R. H. Wechsler, J. Frieman, and A. R. Walker. Eight New Milky Way Companions Discovered in First-year Dark Energy Survey Data. *ApJ*, 807(1):50, Jul 2015.

[11] P. S. Behroozi, C. Conroy, and R. H. Wechsler. A Comprehensive Analysis of Uncertainties Affecting the Stellar Mass-Halo Mass Relation for $0 < z < 4$. *ApJ*, 717:379–403, July 2010.

[12] Peter S. Behroozi, Risa H. Wechsler, and Charlie Conroy. The Average Star Formation Histories of Galaxies in Dark Matter Halos from z = 0-8. *ApJ*, 770(1):57, Jun 2013.

[13] Peter S. Behroozi, Risa H. Wechsler, and Hao-Yi Wu. The ROCKSTAR Phase-space Temporal Halo Finder and the Velocity Offsets of Cluster Cores. *ApJ*, 762(2):109, Jan 2013.

[14] Peter S. Behroozi, Risa H. Wechsler, and Hao-Yi Wu. The ROCKSTAR Phase-space Temporal Halo Finder and the Velocity Offsets of Cluster Cores. *ApJ*, 762(2):109, Jan 2013.

[15] Peter S. Behroozi, Risa H. Wechsler, Hao-Yi Wu, Michael T. Busha, Anatoly A. Klypin, and Joel R. Primack. Gravitationally Consistent Halo Catalogs and Merger Trees for Precision Cosmology. *ApJ*, 763(1):18, January 2013.

[16] V. Belokurov, D. B. Zucker, N. W. Evans, G. Gilmore, S. Vidrih, D. M. Bramich, H. J. Newberg, R. F. G. Wyse, M. J. Irwin, M. Fellhauer, P. C. Hewett, N. A. Walton, M. I. Wilkinson, N. Cole, B. Yanny, C. M. Rockosi, T. C. Beers, E. F. Bell, J. Brinkmann, Ž. Ivezić, and R. Lupton. The Field of Streams: Sagittarius and Its Siblings. *ApJ*, 642(2):L137–L140, May 2006.

[17] José A. Benavides, Laura V. Sales, and Mario G. Abadi. Accretion of galaxy groups into galaxy clusters. *MNRAS*, 498(3):3852–3862, November 2020.

[18] Alejandro Benítez-Llambay, Carlos S. Frenk, Aaron D. Ludlow, and Julio F. Navarro. Baryon-induced dark matter cores in the EAGLE simulations. *MNRAS*, 488(2):2387–2404, September 2019.

[19] Gurtina Besla, David R. Patton, Sabrina Stierwalt, Vicente Rodriguez-Gomez, Ekta Patel, Nitya J. Kallivayalil, Kelsey E. Johnson, Sarah Pearson, George C. Privon, and Mary E. Putman. The frequency of dwarf galaxy multiples at low redshift in SDSS versus cosmological expectations. *MNRAS*, 480(3):3376–3396, Nov 2018.

[20] Paul Bode, Jeremiah P. Ostriker, and Neil Turok. Halo Formation in Warm Dark Matter Models. *ApJ*, 556(1):93–107, July 2001.

[21] Sownak Bose, Alis J. Deason, and Carlos S. Frenk. The Imprint of Cosmic Reionization on the Luminosity Function of Galaxies. *ApJ*, 863(2):123, Aug 2018.

[22] Sownak Bose, Carlos S. Frenk, Adrian Jenkins, Azadeh Fattahi, Facundo A. Gómez, Robert J. J. Grand , Federico Marinacci, Julio F. Navarro, Kyle A. Oman, Rüdiger Pakmor, Joop Schaye, Christine M. Simpson, and Volker Springel. No cores in dark matter-dominated dwarf galaxies with bursty star formation histories. *MNRAS*, 486(4):4790–4804, July 2019.

[23] M. Boylan-Kolchin, G. Besla, and L. Hernquist. Dynamics of the Magellanic Clouds in a Lambda cold dark matter universe. *MNRAS*, 414:1560–1572, June 2011.

[24] M. Boylan-Kolchin, J. S. Bullock, and M. Kaplinghat. The Milky Way's bright satellites as an apparent failure of ΛCDM. *MNRAS*, 422:1203–1218, May 2012.

[25] Michael Boylan-Kolchin, James S. Bullock, and Manoj Kaplinghat. Too big to fail? The puzzling darkness of massive Milky Way subhaloes. *MNRAS*, 415(1):L40–L44, Jul 2011.

[26] Michael Boylan-Kolchin, Volker Springel, Simon D. M. White, Adrian Jenkins, and Gerard Lemson. Resolving cosmic structure formation with the Millennium-II Simulation. *MNRAS*, 398(3):1150–1164, Sep 2009.

[27] Brandon Bozek, Alex Fitts, Michael Boylan-Kolchin, Shea Garrison-Kimmel, Kevork Abazajian, James S. Bullock, Dušan Kereš, Claude-André Faucher-Giguère, Andrew Wetzel, Robert Feldmann, and Philip F. Hopkins. Warm FIRE: simulating galaxy formation with resonant sterile neutrino dark matter. *MNRAS*, 483(3):4086–4099, March 2019.

[28] A. M. Brooks, M. Kuhlen, A. Zolotov, and D. Hooper. A Baryonic Solution to the Missing Satellites Problem. *ApJ*, 765:22, March 2013.

[29] Alyson M. Brooks and Adi Zolotov. Why Baryons Matter: The Kinematics of Dwarf Spheroidal Satellites. *ApJ*, 786(2):87, May 2014.

[30] G. L. Bryan and M. L. Norman. Statistical Properties of X-Ray Clusters: Analytic and Numerical Comparisons. *ApJ*, 495:80–99, March 1998.

[31] Tobias Buck, Andrea V. Macciò, Aaron A. Dutton, Aura Obreja, and Jonas Frings. NIHAO XV: the environmental impact of the host galaxy on galactic satellite and field dwarf galaxies. *MNRAS*, 483(1):1314–1341, February 2019.

[32] J. S. Bullock, A. V. Kravtsov, and D. H. Weinberg. Reionization and the Abundance of Galactic Satellites. *ApJ*, 539:517–521, August 2000.

[33] James S. Bullock and Michael Boylan-Kolchin. Small-Scale Challenges to the ΛCDM Paradigm. *ARA&A*, 55(1):343–387, Aug 2017.

[34] Jan D. Burger and Jesús Zavala. The nature of core formation in dark matter haloes: adiabatic or impulsive? *MNRAS*, 485(1):1008–1028, May 2019.

[35] Jan D. Burger and Jesús Zavala. SN-driven mechanism of cusp-core transformation: an appraisal. *arXiv e-prints*, page arXiv:2103.01231, March 2021.

[36] A. Burkert. The Structure of Dark Matter Halos in Dwarf Galaxies. *ApJ*, 447:L25–L28, July 1995.

[37] A. Burkert. Fuzzy Dark Matter and Dark Matter Halo Cores. *ApJ*, 904(2):161, December 2020.

[38] R. G. Carlberg, C. J. Grillmair, and N. Hetherington. The Pal 5 Star Stream Gaps. *ApJ*, 760:75, November 2012.

[39] Jeffrey L. Carlin, Christopher T. Garling, Annika H. G. Peter, Denija Crnojević, Duncan A. Forbes, Jonathan R. Hargis, Burçin Mutlu-Pakdil, Ragadeepika Pucha, Aaron J. Romanowsky, David J. Sand, Kristine Spekkens, Jay Strader, and Beth Willman. Tidal Destruction in a Low-mass Galaxy Environment: The Discovery of Tidal Tails around DDO 44. *ApJ*, 886(2):109, December 2019.

[40] Jeffrey L. Carlin, Burçin Mutlu-Pakdil, Denija Crnojević, Christopher T. Garling, Ananthan Karunakaran, Annika H. G. Peter, Erik Tollerud, Duncan A. Forbes, Jonathan R. Hargis, Sungsoon Lim, Aaron J. Romanowsky, David J. Sand, Kristine Spekkens, and Jay Strader. Hubble Space Telescope Observations of Two Faint Dwarf Satellites of Nearby LMC Analogs from MADCASH. *ApJ*, 909(2):211, March 2021.

[41] Jeffrey L. Carlin, David J. Sand, Paul Price, Beth Willman, Ananthan Karunakaran, Kristine Spekkens, Eric F. Bell, Jean P. Brodie, Denija Crnojević, and Duncan A. Forbes. First Results from the MADCASH Survey: A Faint Dwarf Galaxy Companion to the Low-mass Spiral Galaxy NGC 2403 at 3.2 Mpc. *ApJ*, 828(1):L5, Sep 2016.

[42] Marius Cautun, Alis J. Deason, Carlos S. Frenk, and Stuart McAlpine. The aftermath of the Great Collision between our Galaxy and the Large Magellanic Cloud. *MNRAS*, 483(2):2185–2196, Feb 2019.

[43] Gilles Chabrier. The Galactic Disk Mass Budget. I. Stellar Mass Function and Density. *ApJ*, 554(2):1274–1281, June 2001.

[44] T. K. Chan, D. Kereš, J. Oñorbe, P. F. Hopkins, A. L. Muratov, C. A. Faucher-Giguère, and E. Quataert. The impact of baryonic physics on the structure of dark matter haloes: the view from the FIRE cosmological simulations. *MNRAS*, 454(3):2981–3001, December 2015.

[45] T. K. Chan, D. Kereš, A. Wetzel, P. F. Hopkins, C. A. Faucher-Giguère, K. El-Badry, S. Garrison-Kimmel, and M. Boylan-Kolchin. The origin of ultra diffuse galaxies: stellar feedback and quenching. *MNRAS*, 478(1):906–925, Jul 2018.

[46] M. Chiba. Probing Dark Matter Substructure in Lens Galaxies. *ApJ*, 565:17–23, January 2002.

[47] Kun Ting Eddie Chua, Annalisa Pillepich, Mark Vogelsberger, and Lars Hernquist. Shape of dark matter haloes in the Illustris simulation: effects of baryons. *MNRAS*, 484(1):476–493, March 2019.

[48] Denis F. Cioffi, Christopher F. McKee, and Edmund Bertschinger. Dynamics of Radiative Supernova Remnants. *ApJ*, 334:252, November 1988.

[49] Michael C. Cooper, Jeffrey A. Newman, Darren J. Croton, Benjamin J. Weiner, Christopher N. A. Willmer, Brian F. Gerke, Darren S. Madgwick, S. M. Faber, Marc Davis, Alison L. Coil, Douglas P. Finkbeiner, Puragra Guhathakurta, and David C. Koo. The DEEP2 Galaxy

Redshift Survey: the relationship between galaxy properties and environment at z ∼1. *MNRAS*, 370(1):198–212, July 2006.

[50] Robert A. Crain, Joop Schaye, Richard G. Bower, Michelle Furlong, Matthieu Schaller, Tom Theuns, Claudio Dalla Vecchia, Carlos S. Frenk, Ian G. McCarthy, John C. Helly, Adrian Jenkins, Yetli M. Rosas-Guevara, Simon D. M. White, and James W. Trayford. The EAGLE simulations of galaxy formation: calibration of subgrid physics and model variations. *MNRAS*, 450(2):1937–1961, June 2015.

[51] Peter Creasey, Omid Sameie, Laura V. Sales, Hai-Bo Yu, Mark Vogelsberger, and Jesús Zavala. Spreading out and staying sharp - creating diverse rotation curves via baryonic and self-interaction effects. *MNRAS*, 468(2):2283–2295, June 2017.

[52] Romeel Davé, Daniel Anglés-Alcázar, Desika Narayanan, Qi Li, Mika H. Rafieferantsoa, and Sarah Appleby. SIMBA: Cosmological simulations with black hole growth and feedback. *MNRAS*, 486(2):2827–2849, June 2019.

[53] Romeel Davé, Benjamin D. Oppenheimer, and Kristian Finlator. Galaxy evolution in cosmological simulations with outflows - I. Stellar masses and star formation rates. *MNRAS*, 415(1):11–31, July 2011.

[54] A. Bianca Davis, Anna M. Nierenberg, Annika H. G. Peter, Christopher T. Garling, Johnny P. Greco, Christopher S. Kochanek, Dyas Utomo, Kirsten J. Casey, Richard W. Pogge, Daniella M. Roberts, David J. Sand, and Amy Sardone. The LBT satellites of Nearby Galaxies Survey (LBT-SONG): the satellite population of NGC 628. *MNRAS*, 500(3):3854–3869, January 2021.

[55] W. J. G. de Blok, Stacy S. McGaugh, Albert Bosma, and Vera C. Rubin. Mass Density Profiles of Low Surface Brightness Galaxies. *ApJ*, 552(1):L23–L26, May 2001.

[56] W. J. G. de Blok, F. Walter, E. Brinks, C. Trachternach, S. H. Oh, and Jr. Kennicutt, R. C. High-Resolution Rotation Curves and Galaxy Mass Models from THINGS. *AJ*, 136(6):2648–2719, December 2008.

[57] A. J. Deason, A. R. Wetzel, S. Garrison-Kimmel, and V. Belokurov. Satellites of LMC-mass dwarfs: close friendships ruined by Milky Way mass haloes. *MNRAS*, 453(4):3568–3574, Nov 2015.

[58] Arianna Di Cintio, Chris B. Brook, Aaron A. Dutton, Andrea V. Macciò, Greg S. Stinson, and Alexander Knebe. A mass-dependent density profile for dark matter haloes including the influence of galaxy formation. *MNRAS*, 441(4):2986–2995, July 2014.

[59] Arianna Di Cintio, Chris B. Brook, Andrea V. Macciò, Greg S. Stinson, Alexander Knebe, Aaron A. Dutton, and James Wadsley. The dependence of dark matter profiles on the stellar-to-halo mass ratio: a prediction for cusps versus cores. *MNRAS*, 437(1):415–423, January 2014.

[60] Ruth Digby, Julio F. Navarro, Azadeh Fattahi, Christine M. Simpson, Kyle A. Oman, Facundo A. Gomez, Carlos S. Frenk, Robert J. J. Grand, and Ruediger Pakmor. The star formation histories of dwarf galaxies in Local Group cosmological simulations. *MNRAS*, 485(4):5423–5437, June 2019.

[61] Scott Dodelson and Lawrence M. Widrow. Sterile neutrinos as dark matter. *Phys. Rev. Lett.*, 72(1):17–20, January 1994.

[62] Elena D'Onghia and George Lake. Small Dwarf Galaxies within Larger Dwarfs: Why Some Are Luminous while Most Go Dark. *ApJ*, 686(2):L61, Oct 2008.

[63] Elena D'Onghia, Volker Springel, Lars Hernquist, and Dusan Keres. Substructure Depletion in the Milky Way Halo by the Disk. *ApJ*, 709(2):1138–1147, Feb 2010.

[64] Gregory A. Dooley, Annika H. G. Peter, Jeffrey L. Carlin, Anna Frebel, Keith Bechtol, and Beth Willman. The predicted luminous satellite populations around SMC- and LMC-mass galaxies - a missing satellite problem around the LMC? *MNRAS*, 472(1):1060–1073, Nov 2017.

[65] A. Drlica-Wagner, K. Bechtol, E. S. Rykoff, E. Luque, A. Queiroz, Y. Y. Mao, R. H. Wechsler, J. D. Simon, B. Santiago, and B. Yanny. Eight Ultra-faint Galaxy Candidates Discovered in Year Two of the Dark Energy Survey. *ApJ*, 813(2):109, Nov 2015.

[66] A. Drlica-Wagner, J. L. Carlin, D. L. Nidever, P. S. Ferguson, N. Kuropatkin, M. Adamów, W. Cerny, Y. Choi, J. H. Esteves, C. E. Martínez-Vázquez, S. Mau, A. E. Miller, B. Mutlu-Pakdil, E. H. Neilsen, K. A. G. Olsen, A. B. Pace, A. H. Riley, J. D. Sakowska, D. J. Sand, L. Santana-Silva, E. J. Tollerud, D. L. Tucker, A. K. Vivas, E. Zaborowski, A. Zenteno, T. M. C. Abbott, S. Allam, K. Bechtol, C. P. M. Bell, E. F. Bell, P. Bilaji, C. R. Bom, J. A. Carballo-Bello, M. R. L. Cioni, A. Diaz-Ocampo, T. J. L. de Boer, D. Erkal, R. A. Gruendl, D. Hernandez-Lang, A. K. Hughes, D. J. James, L. C. Johnson, T. S. Li, Y. Y. Mao, D. Martínez-Delgado, P. Massana, M. McNanna, R. Morgan, E. O. Nadler, N. E. D. Noël, A. Palmese, A. H. G. Peter, E. S. Rykoff, J. Sánchez, N. Shipp, J. D. Simon, A. Smercina, M. Soares-Santos, G. S. Stringfellow, K. Tavangar, R. P. van der Marel, A. R. Walker, R. H. Wechsler, J. F. Wu, B. Yanny, M. Fitzpatrick, L. Huang, A. Jacques, R. Nikutta, and A. Scott. The DECam Local Volume Exploration Survey: Overview and First Data Release. *arXiv e-prints*, page arXiv:2103.07476, March 2021.

[67] Y. Dubois, C. Pichon, C. Welker, D. Le Borgne, J. Devriendt, C. Laigle, S. Codis, D. Pogosyan, S. Arnouts, K. Benabed, E. Bertin, J. Blaizot, F. Bouchet, J. F. Cardoso, S. Colombi, V. de Lapparent, V. Desjacques, R. Gavazzi, S. Kassin, T. Kimm, H. McCracken, B. Milliard, S. Peirani, S. Prunet, S. Rouberol, J. Silk, A. Slyz, T. Sousbie, R. Teyssier, L. Tresse, M. Treyer, D. Vibert, and M. Volonteri. Dancing in the dark: galactic properties trace spin swings along the cosmic web. *MNRAS*, 444(2):1453–1468, October 2014.

[68] Aaron A. Dutton, Tobias Buck, Andrea V. Macciò, Keri L. Dixon, Marvin Blank, and Aura Obreja. NIHAO - XXV. Convergence in the cusp-core transformation of cold dark matter haloes at high star formation thresholds. *MNRAS*, 499(2):2648–2661, December 2020.

[69] Aaron A. Dutton, Andrea V. Macciò, Tobias Buck, Keri L. Dixon, Marvin Blank, and Aura Obreja. NIHAO XX: the impact of the star formation threshold on the cusp-core transformation of cold dark matter haloes. *MNRAS*, 486(1):655–671, June 2019.

[70] Aaron A. Dutton, Andrea V. Macciò, Avishai Dekel, Liang Wang, Gregory Stinson, Aura Obreja, Arianna Di Cintio, Chris Brook, Tobias Buck, and Xi Kang. NIHAO IX: the role of gas inflows and outflows in driving the contraction and expansion of cold dark matter haloes. *MNRAS*, 461(3):2658–2675, September 2016.

[71] K. El-Badry, J. Bradford, E. Quataert, M. Geha, M. Boylan-Kolchin, D. R. Weisz, A. Wetzel, P. F. Hopkins, T. K. Chan, A. Fitts, D. Kereš, and C.-A. Faucher-Giguère. Gas kinematics in FIRE simulated galaxies compared to spatially unresolved H I observations. *MNRAS*, 477:1536–1548, June 2018.

[72] Kareem El-Badry, Eliot Quataert, Andrew Wetzel, Philip F. Hopkins, Daniel R. Weisz, T. K. Chan, Alex Fitts, Michael Boylan-Kolchin, Dušan Kereš, Claude-André Faucher-Giguère, and Shea Garrison-Kimmel. Gas kinematics, morphology and angular momentum in the FIRE simulations. *MNRAS*, 473(2):1930–1955, January 2018.

[73] Kareem El-Badry, Andrew Wetzel, Marla Geha, Philip F. Hopkins, Dusan Kereš, T. K. Chan, and Claude-André Faucher-Giguère. Breathing FIRE: How Stellar Feedback Drives Radial Migration, Rapid Size Fluctuations, and Population Gradients in Low-mass Galaxies. *ApJ*, 820(2):131, Apr 2016.

[74] Kareem El-Badry, Andrew R. Wetzel, Marla Geha, Eliot Quataert, Philip F. Hopkins, Dusan Kereš, T. K. Chan, and Claude-André Faucher-Giguère. When the Jeans Do Not Fit: How Stellar Feedback Drives Stellar Kinematics and Complicates Dynamical Modeling in Low-mass Galaxies. *ApJ*, 835(2):193, Feb 2017.

[75] Oliver D. Elbert, James S. Bullock, Manoj Kaplinghat, Shea Garrison-Kimmel, Andrew S. Graus, and Miguel Rocha. A Testable Conspiracy: Simulating Baryonic Effects on Self-interacting Dark Matter Halos. *ApJ*, 853(2):109, February 2018.

[76] Andrew Emerick, Mordecai-Mark Mac Low, Jana Grcevich, and Andrea Gatto. Gas Loss by Ram Pressure Stripping and Internal Feedback from Low-mass Milky Way Satellites. *ApJ*, 826(2):148, August 2016.

[77] Denis Erkal and Vasily A. Belokurov. Limit on the LMC mass from a census of its satellites. *MNRAS*, 495(3):2554–2563, July 2020.

[78] Ivanna Escala, Andrew Wetzel, Evan N. Kirby, Philip F. Hopkins, Xiangcheng Ma, Coral Wheeler, Dušan Kereš, Claude-André Faucher-Giguère, and Eliot Quataert. Modelling chemical abundance distributions for dwarf galaxies in the Local Group: the impact of turbulent metal diffusion. *MNRAS*, 474(2):2194–2211, Feb 2018.

[79] A. Fattahi, J. F. Navarro, E. Starkenburg, C. R. Barber, and A. W. McConnachie. Galaxy pairs in the local group. *MNRAS*, 431:L73–L77, Apr 2013.

[80] Claude-André Faucher-Giguère, Adam Lidz, Matias Zaldarriaga, and Lars Hernquist. A New Calculation of the Ionizing Background Spectrum and the Effects of He II Reionization. *ApJ*, 703(2):1416–1443, October 2009.

[81] Ismael Ferrero, Mario G. Abadi, Julio F. Navarro, Laura V. Sales, and Sebastián. Gurovich. The dark matter haloes of dwarf galaxies: a challenge for the Λ cold dark matter paradigm? *MNRAS*, 425(4):2817–2823, Oct 2012.

[82] Katia M. Ferrière. The interstellar environment of our galaxy. *Reviews of Modern Physics*, 73(4):1031–1066, October 2001.

[83] Sean P. Fillingham, Michael C. Cooper, Michael Boylan-Kolchin, James S. Bullock, Shea Garrison-Kimmel, and Coral Wheeler. Environmental quenching of low-mass field galaxies. *MNRAS*, 477(4):4491–4498, July 2018.

[84] Sean P. Fillingham, Michael C. Cooper, Tyler Kelley, M. K. Rodriguez Wimberly, Michael Boylan-Kolchin, James S. Bullock, Shea Garrison-Kimmel, Marcel S. Pawlowski, and Coral Wheeler. Characterizing the Infall Times and Quenching Timescales of Milky Way Satellites with *Gaia* Proper Motions. *arXiv e-prints*, page arXiv:1906.04180, June 2019.

[85] Sean P. Fillingham, Michael C. Cooper, Andrew B. Pace, Michael Boylan-Kolchin, James S. Bullock, Shea Garrison-Kimmel, and Coral Wheeler. Under pressure: quenching star formation in low-mass satellite galaxies via stripping. *MNRAS*, 463(2):1916–1928, December 2016.

[86] Sean P. Fillingham, Michael C. Cooper, Coral Wheeler, Shea Garrison-Kimmel, Michael Boylan-Kolchin, and James S. Bullock. Taking care of business in a flash: constraining the time-scale for low-mass satellite quenching with ELVIS. *MNRAS*, 454(2):2039–2049, December 2015.

[87] Alex Fitts, Michael Boylan-Kolchin, Brandon Bozek, James S. Bullock, Andrew Graus, Victor Robles, Philip F. Hopkins, Kareem El-Badry, Shea Garrison-Kimmel, Claude-André Faucher-Giguère, Andrew Wetzel, and Dušan Kereš. Dwarf galaxies in CDM, WDM, and SIDM: disentangling baryons and dark matter physics. *MNRAS*, 490(1):962–977, November 2019.

[88] Alex Fitts, Michael Boylan-Kolchin, Oliver D. Elbert, James S. Bullock, Philip F. Hopkins, Jose Oñorbe, Andrew Wetzel, Coral Wheeler, Claude-André Faucher-Giguère, Dušan Kereš, Evan D. Skillman, and Daniel R. Weisz. fire in the field: simulating the threshold of galaxy formation. *MNRAS*, 471(3):3547–3562, November 2017.

[89] Ricardo A. Flores and Joel R. Primack. Observational and Theoretical Constraints on Singular Dark Matter Halos. *ApJ*, 427:L1, May 1994.

[90] Gaia Collaboration, A. Helmi, F. van Leeuwen, P. J. McMillan, D. Massari, T. Antoja, A. C. Robin, L. Lindegren, U. Bastian, and F. Arenou. Gaia Data Release 2. Kinematics of globular clusters and dwarf galaxies around the Milky Way. *A&A*, 616:A12, Aug 2018.

[91] L. Gao, S. D. M. White, A. Jenkins, F. Stoehr, and V. Springel. The subhalo populations of ΛCDM dark haloes. *MNRAS*, 355(3):819–834, Dec 2004.

[92] Christopher T. Garling, Annika H. G. Peter, Christopher S. Kochanek, David J. Sand, and Denija Crnojević. The case for strangulation in low-mass hosts: DDO 113. *MNRAS*, 492(2):1713–1730, February 2020.

[93] Shea Garrison-Kimmel, Michael Boylan-Kolchin, James S. Bullock, and Kyle Lee. ELVIS: Exploring the Local Volume in Simulations. *MNRAS*, 438(3):2578–2596, Mar 2014.

[94] Shea Garrison-Kimmel, James S. Bullock, Michael Boylan-Kolchin, and Emma Bardwell. Organized chaos: scatter in the relation between stellar mass and halo mass in small galaxies. *MNRAS*, 464(3):3108–3120, Jan 2017.

[95] Shea Garrison-Kimmel, Philip F. Hopkins, Andrew Wetzel, James S. Bullock, Michael Boylan-Kolchin, Dušan Kereš, Claude-André Faucher-Giguère, Kareem El-Badry, Astrid Lamberts, Eliot Quataert, and Robyn Sand erson. The Local Group on FIRE: Dwarf galaxy populations across a suite of hydrodynamic simulations. *MNRAS*, page 1262, May 2019.

[96] Shea Garrison-Kimmel, Philip F. Hopkins, Andrew Wetzel, Kareem El-Badry, Robyn E. Sanderson, James S. Bullock, Xiangcheng Ma, Freeke van de Voort, Zachary Hafen, Claude-André Faucher-Giguère, Christopher C. Hayward, Eliot Quataert, Dušan Kereš, and Michael Boylan-Kolchin. The origin of the diverse morphologies and kinematics of Milky Way-mass galaxies in the FIRE-2 simulations. *MNRAS*, 481(3):4133–4157, Dec 2018.

[97] Shea Garrison-Kimmel, Andrew Wetzel, James S. Bullock, Philip F. Hopkins, Michael Boylan-Kolchin, Claude-André Faucher-Giguère, Dušan Kereš, Eliot Quataert, Robyn E. Sanderson, and Andrew S. Graus. Not so lumpy after all: modelling the depletion of dark matter subhaloes by Milky Way-like galaxies. *MNRAS*, 471(2):1709–1727, Oct 2017.

[98] Shea Garrison-Kimmel, Andrew Wetzel, Philip F. Hopkins, Robyn Sanderson, Kareem El-Badry, Andrew Graus, T. K. Chan, Robert Feldmann, Michael Boylan-Kolchin, Christopher C. Hayward, James S. Bullock, Alex Fitts, Jenna Samuel, Coral Wheeler, Dušan Kereš, and Claude-André Faucher-Giguère. Star formation histories of dwarf galaxies in the FIRE simulations: dependence on mass and Local Group environment. *MNRAS*, 489(4):4574–4588, November 2019.

[99] M. Geha, M. R. Blanton, R. Yan, and J. L. Tinker. A Stellar Mass Threshold for Quenching of Field Galaxies. *ApJ*, 757(1):85, September 2012.

[100] Shy Genel, Mark Vogelsberger, Volker Springel, Debora Sijacki, Dylan Nelson, Greg Snyder, Vicente Rodriguez-Gomez, Paul Torrey, and Lars Hernquist. Introducing the Illustris project: the evolution of galaxy populations across cosmic time. *MNRAS*, 445(1):175–200, November 2014.

[101] Anna Genina, Alejandro Benítez-Llambay, Carlos S. Frenk, Shaun Cole, Azadeh Fattahi, Julio F. Navarro, Kyle A. Oman, Till Sawala, and Tom Theuns. The core-cusp problem: a matter of perspective. *MNRAS*, 474(1):1398–1411, February 2018.

[102] Gerard Gilmore, Mark I. Wilkinson, Rosemary F. G. Wyse, Jan T. Kleyna, Andreas Koch, N. Wyn Evans, and Eva K. Grebel. The Observed Properties of Dark Matter on Small Spatial Scales. *ApJ*, 663(2):948–959, July 2007.

[103] C. Giocoli, G. Tormen, and F. C. van den Bosch. The population of dark matter subhaloes: mass functions and average mass-loss rates. *MNRAS*, 386:2135–2144, June 2008.

[104] F. Governato, C. Brook, L. Mayer, A. Brooks, G. Rhee, J. Wadsley, P. Jonsson, B. Willman, G. Stinson, T. Quinn, and P. Madau. Bulgeless dwarf galaxies and dark matter cores from supernova-driven outflows. *Nature*, 463(7278):203–206, January 2010.

[105] F. Governato, L. Mayer, J. Wadsley, J. P. Gardner, Beth Willman, E. Hayashi, T. Quinn, J. Stadel, and G. Lake. The Formation of a Realistic Disk Galaxy in Λ-dominated Cosmologies. *ApJ*, 607(2):688–696, Jun 2004.

[106] Robert J. J. Grand, Facundo A. Gómez, Federico Marinacci, Rüdiger Pakmor, Volker Springel, David J. R. Campbell, Carlos S. Frenk, Adrian Jenkins, and Simon D. M. White. The Auriga Project: the properties and formation mechanisms of disc galaxies across cosmic time. *MNRAS*, 467(1):179–207, May 2017.

[107] A. S. Graus, J. S. Bullock, T. Kelley, M. Boylan-Kolchin, S. Garrison-Kimmel, and Y. Qi. How low does it go? Too few Galactic satellites with standard reionization quenching. *ArXiv e-prints*, August 2018.

[108] Jana Grcevich and Mary E. Putman. H I in Local Group Dwarf Galaxies and Stripping by the Galactic Halo. *ApJ*, 696(1):385–395, May 2009.

[109] Eva K. Grebel, III Gallagher, John S., and Daniel Harbeck. The Progenitors of Dwarf Spheroidal Galaxies. *AJ*, 125(4):1926–1939, April 2003.

[110] L. Greggio. The rates of type Ia supernovae. I. Analytical formulations. *A&A*, 441(3):1055–1078, October 2005.

[111] Brendan F. Griffen, Alexander P. Ji, Gregory A. Dooley, Facundo A. Gómez, Mark Vogelsberger, Brian W. O'Shea, and Anna Frebel. The Caterpillar Project: A Large Suite of Milky Way Sized Halos. *ApJ*, 818(1):10, Feb 2016.

[112] James E. Gunn and III Gott, J. Richard. On the Infall of Matter Into Clusters of Galaxies and Some Effects on Their Evolution. *ApJ*, 176:1, August 1972.

[113] Q. Guo, S. White, C. Li, and M. Boylan-Kolchin. How do galaxies populate dark matter haloes? *MNRAS*, 404:1111–1120, May 2010.

[114] Qi Guo, Simon White, Michael Boylan-Kolchin, Gabriella De Lucia, Guinevere Kauffmann, Gerard Lemson, Cheng Li, Volker Springel, and Simone Weinmann. From dwarf spheroidals to cD galaxies: simulating the galaxy population in a ΛCDM cosmology. *MNRAS*, 413(1):101–131, May 2011.

[115] A. Gupta, S. Mathur, Y. Krongold, F. Nicastro, and M. Galeazzi. A Huge Reservoir of Ionized Gas around the Milky Way: Accounting for the Missing Mass? *ApJ*, 756(1):L8, September 2012.

[116] Oliver Hahn and Tom Abel. Multi-scale initial conditions for cosmological simulations. *MNRAS*, 415(3):2101–2121, Aug 2011.

[117] Eric Hayashi, Julio F. Navarro, James E. Taylor, Joachim Stadel, and Thomas Quinn. The Structural Evolution of Substructure. *ApJ*, 584(2):541–558, Feb 2003.

[118] Amina Helmi and Simon D. M. White. Building up the stellar halo of the Galaxy. *MNRAS*, 307(3):495–517, August 1999.

[119] Amina Helmi and Simon D. M. White. Simple dynamical models of the Sagittarius dwarf galaxy. *MNRAS*, 323(3):529–536, May 2001.

[120] Lars Hernquist. An Analytical Model for Spherical Galaxies and Bulges. *ApJ*, 356:359, June 1990.

[121] Philip F. Hopkins. A new class of accurate, mesh-free hydrodynamic simulation methods. *MNRAS*, 450(1):53–110, Jun 2015.

[122] Philip F. Hopkins, Dušan Kereš, José Oñorbe, Claude-André Faucher-Giguère, Eliot Quataert, Norman Murray, and James S. Bullock. Galaxies on FIRE (Feedback In Realistic Environments): stellar feedback explains cosmologically inefficient star formation. *MNRAS*, 445(1):581–603, November 2014.

[123] Philip F. Hopkins, Desika Narayanan, and Norman Murray. The meaning and consequences of star formation criteria in galaxy models with resolved stellar feedback. *MNRAS*, 432(4):2647–2653, Jul 2013.

[124] Philip F. Hopkins, Eliot Quataert, and Norman Murray. Self-regulated star formation in galaxies via momentum input from massive stars. *MNRAS*, 417(2):950–973, October 2011.

[125] Philip F. Hopkins and Matthias J. Raives. Accurate, meshless methods for magnetohydrodynamics. *MNRAS*, 455(1):51–88, January 2016.

[126] Philip F. Hopkins, Andrew Wetzel, Dušan Kereš, Claude-André Faucher-Giguère, Eliot Quataert, Michael Boylan-Kolchin, Norman Murray, Christopher C. Hayward, and Kareem El-Badry. How to model supernovae in simulations of star and galaxy formation. *MNRAS*, 477(2):1578–1603, Jun 2018.

[127] Philip F. Hopkins, Andrew Wetzel, Dušan Kereš, Claude-André Faucher-Giguère, Eliot Quataert, Michael Boylan-Kolchin, Norman Murray, Christopher C. Hayward, Shea Garrison-Kimmel, Cameron Hummels, Robert Feldmann, Paul Torrey, Xiangcheng Ma, Daniel Anglés-Alcázar, Kung-Yi Su, Matthew Orr, Denise Schmitz, Ivanna Escala, Robyn Sanderson, Michael Y. Grudić, Zachary Hafen, Ji-Hoon Kim, Alex Fitts, James S. Bullock, Coral Wheeler, T. K. Chan, Oliver D. Elbert, and Desika Narayanan. FIRE-2 simulations: physics versus numerics in galaxy formation. *MNRAS*, 480(1):800–863, October 2018.

[128] Wayne Hu, Rennan Barkana, and Andrei Gruzinov. Fuzzy Cold Dark Matter: The Wave Properties of Ultralight Particles. *Phys. Rev. Lett.*, 85(6):1158–1161, August 2000.

[129] R. A. Ibata, G. Gilmore, and M. J. Irwin. A dwarf satellite galaxy in Sagittarius. *Nature*, 370(6486):194–196, July 1994.

[130] S. Ikeuchi and J. P. Ostriker. Evolution of the Intergalactic Medium: What Happened during the Epoch Z = 3–10? *ApJ*, 301:522, February 1986.

[131] G. Iorio, F. Fraternali, C. Nipoti, E. Di Teodoro, J. I. Read, and G. Battaglia. LITTLE THINGS in 3D: robust determination of the circular velocity of dwarf irregular galaxies. *MNRAS*, 466(4):4159–4192, April 2017.

[132] Ethan D. Jahn, Laura V. Sales, Andrew Wetzel, Michael Boylan-Kolchin, T. K. Chan, Kareem El-Badry, Alexandres Lazar, and James S. Bullock. Dark and luminous satellites of LMC-mass galaxies in the FIRE simulations. *MNRAS*, 489(4):5348–5364, November 2019.

[133] A. Jenkins, C. S. Frenk, F. R. Pearce, P. A. Thomas, J. M. Colberg, S. D. M. White, H. M. P. Couchman, J. A. Peacock, G. Efstathiou, and A. H. Nelson. Evolution of Structure in Cold Dark Matter Universes. *ApJ*, 499(1):20–40, May 1998.

[134] P. Jethwa, D. Erkal, and V. Belokurov. A Magellanic origin of the DES dwarfs. *MNRAS*, 461(2):2212–2233, Sep 2016.

[135] P. Jethwa, D. Erkal, and V. Belokurov. The upper bound on the lowest mass halo. *MNRAS*, 473(2):2060–2083, January 2018.

[136] Kathryn V. Johnston, David N. Spergel, and Lars Hernquist. The Disruption of the Sagittarius Dwarf Galaxy. *ApJ*, 451:598, October 1995.

[137] N. Kallivayalil, R. P. van der Marel, G. Besla, J. Anderson, and C. Alcock. Third-epoch Magellanic Cloud Proper Motions. I. Hubble Space Telescope/WFC3 Data and Orbit Implications. *ApJ*, 764:161, February 2013.

[138] Nitya Kallivayalil, Laura V. Sales, Paul Zivick, Tobias K. Fritz, Andrés Del Pino, Sangmo Tony Sohn, Gurtina Besla, Roeland P. van der Marel, Julio F. Navarro, and Elena Sacchi. The Missing Satellites of the Magellanic Clouds? Gaia Proper Motions of the Recently Discovered Ultra-faint Galaxies. *ApJ*, 867(1):19, Nov 2018.

[139] Rahul Kannan, Federico Marinacci, Mark Vogelsberger, Laura V. Sales, Paul Torrey, Volker Springel, and Lars Hernquist. Simulating the interstellar medium of galaxies with radiative transfer, non-equilibrium thermochemistry, and dust. *MNRAS*, 499(4):5732–5748, December 2020.

[140] Manoj Kaplinghat, Tao Ren, and Hai-Bo Yu. Dark matter cores and cusps in spiral galaxies and their explanations. *J. Cosmology Astropart. Phys.*, 2020(6):027, June 2020.

[141] Neal Katz, David H. Weinberg, and Lars Hernquist. Cosmological Simulations with TreeSPH. *ApJS*, 105:19, July 1996.

[142] Neal Katz and Simon D. M. White. Hierarchical Galaxy Formation: Overmerging and the Formation of an X-Ray Cluster. *ApJ*, 412:455, Aug 1993.

[143] Guinevere Kauffmann, Simon D. M. White, Timothy M. Heckman, Brice Ménard, Jarle Brinchmann, Stéphane Charlot, Christy Tremonti, and Jon Brinkmann. The environmental dependence of the relations between stellar mass, structure, star formation and nuclear activity in galaxies. *MNRAS*, 353(3):713–731, September 2004.

[144] Tyler Kelley, James S. Bullock, Shea Garrison-Kimmel, Michael Boylan-Kolchin, Marcel S. Pawlowski, and Andrew S. Graus. Phat ELVIS: The inevitable effect of the Milky Way's disc on its dark matter subhaloes. *MNRAS*, page 1496, Jun 2019.

[145] Dongwon Kim and Helmut Jerjen. Horologium II: A Second Ultra-faint Milky Way Satellite in the Horologium Constellation. *ApJ*, 808(2):L39, Aug 2015.

[146] Evan N. Kirby, James S. Bullock, Michael Boylan-Kolchin, Manoj Kaplinghat, and Judith G. Cohen. The dynamics of isolated Local Group galaxies. *MNRAS*, 439(1):1015–1027, Mar 2014.

[147] Anatoly Klypin, Andrey V. Kravtsov, James S. Bullock, and Joel R. Primack. Resolving the Structure of Cold Dark Matter Halos. *ApJ*, 554(2):903–915, June 2001.

[148] Anatoly Klypin, Andrey V. Kravtsov, Octavio Valenzuela, and Francisco Prada. Where Are the Missing Galactic Satellites? *ApJ*, 522(1):82–92, Sep 1999.

[149] S. E. Koposov, H.-W. Rix, and D. W. Hogg. Constraining the Milky Way Potential with a Six-Dimensional Phase-Space Map of the GD-1 Stellar Stream. *ApJ*, 712:260–273, March 2010.

[150] Sergey E. Koposov, Vasily Belokurov, Gabriel Torrealba, and N. Wyn Evans. Beasts of the Southern Wild: Discovery of Nine Ultra Faint Satellites in the Vicinity of the Magellanic Clouds. *ApJ*, 805(2):130, Jun 2015.

[151] Sergey E. Koposov, Matthew G. Walker, Vasily Belokurov, Andrew R. Casey, Alex Geringer-Sameth, Dougal Mackey, Gary Da Costa, Denis Erkal, Prashin Jethwa, and Mario Mateo. Snake in the Clouds: a new nearby dwarf galaxy in the Magellanic bridge*. *MNRAS*, 479(4):5343–5361, Oct 2018.

[152] John Kormendy, David B. Fisher, Mark E. Cornell, and Ralf Bender. Structure and Formation of Elliptical and Spheroidal Galaxies. *ApJS*, 182(1):216–309, May 2009.

[153] Andrey V. Kravtsov, Andreas A. Berlind, Risa H. Wechsler, Anatoly A. Klypin, Stefan Gottlöber, Brand on Allgood, and Joel R. Primack. The Dark Side of the Halo Occupation Distribution. *ApJ*, 609(1):35–49, Jul 2004.

[154] Pavel Kroupa. On the variation of the initial mass function. *MNRAS*, 322(2):231–246, Apr 2001.

[155] M. R. Krumholz and N. Y. Gnedin. A Comparison of Methods for Determining the Molecular Content of Model Galaxies. *ApJ*, 729:36, March 2011.

[156] Rachel Kuzio de Naray, Stacy S. McGaugh, and W. J. G. de Blok. Mass Models for Low Surface Brightness Galaxies with High-Resolution Optical Velocity Fields. *ApJ*, 676(2):920–943, April 2008.

[157] Rachel Kuzio de Naray, Stacy S. McGaugh, W. J. G. de Blok, and A. Bosma. High-Resolution Optical Velocity Fields of 11 Low Surface Brightness Galaxies. *ApJS*, 165(2):461–479, August 2006.

[158] Benjamin P. M. Laevens, Nicolas F. Martin, Edouard J. Bernard, Edward F. Schlafly, Branimir Sesar, Hans-Walter Rix, Eric F. Bell, Annette M. N. Ferguson, Colin T. Slater, and William E. Sweeney. Sagittarius II, Draco II and Laevens 3: Three New Milky Way Satellites Discovered in the Pan-STARRS 1 3π Survey. *ApJ*, 813(1):44, Nov 2015.

[159] Lachlan Lancaster, Cara Giovanetti, Philip Mocz, Yonatan Kahn, Mariangela Lisanti, and David N. Spergel. Dynamical friction in a Fuzzy Dark Matter universe. *J. Cosmology Astropart. Phys.*, 2020(1):001, January 2020.

[160] R. B. Larson, B. M. Tinsley, and C. N. Caldwell. The evolution of disk galaxies and the origin of S0 galaxies. *ApJ*, 237:692–707, May 1980.

[161] Alexandres Lazar, James S. Bullock, Michael Boylan-Kolchin, T. K. Chan, Philip F. Hopkins, Andrew S. Graus, Andrew Wetzel, Kareem El-Badry, Coral Wheeler, Maria C. Straight, Dušan Kereš, Claude-André Faucher-Giguère, Alex Fitts, and Shea Garrison-Kimmel. A dark matter profile to model diverse feedback-induced core sizes of ΛCDM haloes. *MNRAS*, 497(2):2393–2417, September 2020.

[162] N. Lehner and J. C. Howk. Highly ionized plasma in the Large Magellanic Cloud: evidence for outflows and a possible galactic wind. *MNRAS*, 377(2):687–704, May 2007.

[163] Claus Leitherer, Daniel Schaerer, Jeffrey D. Goldader, Rosa M. González Delgado, Carmelle Robert, Denis Foo Kune, Duília F. de Mello, Daniel Devost, and Timothy M. Heckman. Starburst99: Synthesis Models for Galaxies with Active Star Formation. *The Astrophysical Journal Supplement Series*, 123(1):3–40, Jul 1999.

[164] Federico Lelli, Stacy S. McGaugh, and James M. Schombert. SPARC: Mass Models for 175 Disk Galaxies with Spitzer Photometry and Accurate Rotation Curves. *AJ*, 152(6):157, December 2016.

[165] Hui Li, Mark Vogelsberger, Federico Marinacci, Laura V. Sales, and Paul Torrey. The effects of subgrid models on the properties of giant molecular clouds in galaxy formation simulations. *MNRAS*, 499(4):5862–5872, December 2020.

[166] Yang-Shyang Li and Amina Helmi. Infall of substructures on to a Milky Way-like dark halo. *MNRAS*, 385(3):1365–1373, April 2008.

[167] Thorsten Lisker, Eva K. Grebel, Bruno Binggeli, and Katharina Glatt. Virgo Cluster Early-Type Dwarf Galaxies with the Sloan Digital Sky Survey. III. Subpopulations: Distributions, Shapes, Origins. *ApJ*, 660(2):1186–1197, May 2007.

[168] S. Lucchini, E. D'Onghia, A. J. Fox, C. Bustard, J. Bland-Hawthorn, and E. Zweibel. The Magellanic Corona as the key to the formation of the Magellanic Stream. *Nature*, 585:203–206, January 2020.

[169] Aaron D. Ludlow, Joop Schaye, and Richard Bower. Numerical convergence of simulations of galaxy formation: the abundance and internal structure of cold dark matter haloes. *MNRAS*, 488(3):3663–3684, September 2019.

[170] Aaron D. Ludlow, Joop Schaye, Matthieu Schaller, and Richard Bower. Numerical convergence of hydrodynamical simulations of galaxy formation: the abundance and internal structure of galaxies and their cold dark matter haloes. *MNRAS*, 493(2):2926–2951, April 2020.

[171] Aaron D. Ludlow, Joop Schaye, Matthieu Schaller, and Jack Richings. Energy equipartition between stellar and dark matter particles in cosmological simulations results in spurious growth of galaxy sizes. *MNRAS*, 488(1):L123–L128, September 2019.

[172] D. Lynden-Bell and R. M. Lynden-Bell. Ghostly streams from the formation of the Galaxy's halo. *MNRAS*, 275(2):429–442, Jul 1995.

[173] Xiangcheng Ma, Philip F. Hopkins, Claude-André Faucher-Giguère, Nick Zolman, Alexander L. Muratov, Dušan Kereš, and Eliot Quataert. The origin and evolution of the galaxy mass-metallicity relation. *MNRAS*, 456(2):2140–2156, Feb 2016.

[174] A. V. Macciò, G. Stinson, C. B. Brook, J. Wadsley, H. M. P. Couchman, S. Shen, B. K. Gibson, and T. Quinn. Halo Expansion in Cosmological Hydro Simulations: Toward a Baryonic Solution of the Cusp/Core Problem in Massive Spirals. *ApJ*, 744(1):L9, January 2012.

[175] Piero Madau, Sijing Shen, and Fabio Governato. Dark Matter Heating and Early Core Formation in Dwarf Galaxies. *ApJ*, 789(1):L17, July 2014.

[176] Steven R. Majewski, Jeffrey A. Munn, and Suzanne L. Hawley. Absolute Proper Motions to B approximately 22.5: Large-Scale Streaming Motions and the Structure and Origin of the Galactic Halo. *ApJ*, 459:L73, March 1996.

[177] David Malin and Brian Hadley. HI in Shell Galaxies and Other Merger Remnants. *Publ. Astron. Soc. Australia*, 14(1):52–58, April 1997.

[178] Yao-Yuan Mao, Marla Geha, Risa H. Wechsler, Benjamin Weiner, Erik J. Tollerud, Ethan O. Nadler, and Nitya Kallivayalil. The SAGA Survey. II. Building a Statistical Sample of Satellite Systems around Milky Way-like Galaxies. *ApJ*, 907(2):85, February 2021.

[179] A. Marasco, K. A. Oman, J. F. Navarro, C. S. Frenk, and T. Oosterloo. Bars in dark-matter-dominated dwarf galaxy discs. *MNRAS*, 476(2):2168–2176, May 2018.

[180] Federico Marinacci, Rüdiger Pakmor, and Volker Springel. The formation of disc galaxies in high-resolution moving-mesh cosmological simulations. *MNRAS*, 437(2):1750–1775, January 2014.

[181] Federico Marinacci, Laura V. Sales, Mark Vogelsberger, Paul Torrey, and Volker Springel. Simulating the interstellar medium and stellar feedback on a moving mesh: implementation and isolated galaxies. *MNRAS*, 489(3):4233–4260, November 2019.

[182] David Martínez-Delgado, R. Jay Gabany, Ken Crawford, Stefano Zibetti, Steven R. Majewski, Hans-Walter Rix, Jürgen Fliri, Julio A. Carballo-Bello, Daniella C. Bardalez-Gagliuffi, Jorge Peñarrubia, Taylor S. Chonis, Barry Madore, Ignacio Trujillo, Mischa Schirmer, and David A. McDavid. Stellar Tidal Streams in Spiral Galaxies of the Local Volume: A Pilot Survey with Modest Aperture Telescopes. *AJ*, 140(4):962–967, October 2010.

[183] David Martínez-Delgado, Jorge Peñarrubia, R. Jay Gabany, Ignacio Trujillo, Steven R. Majewski, and M. Pohlen. The Ghost of a Dwarf Galaxy: Fossils of the Hierarchical Formation of the Nearby Spiral Galaxy NGC 5907. *ApJ*, 689(1):184–193, December 2008.

[184] David Martínez-Delgado, Aaron J. Romanowsky, R. Jay Gabany, Francesca Annibali, Jacob A. Arnold, Jürgen Fliri, Stefano Zibetti, Roeland P. van der Marel, Hans-Walter Rix, Taylor S. Chonis, Julio A. Carballo-Bello, Alessandra Aloisi, Andrea V. Macciò, J. Gallego-Laborda, Jean P. Brodie, and Michael R. Merrifield. Dwarfs Gobbling Dwarfs: A Stellar Tidal Stream around NGC 4449 and Hierarchical Galaxy Formation on Small Scales. *ApJ*, 748(2):L24, April 2012.

[185] Alan W. McConnachie. The Observed Properties of Dwarf Galaxies in and around the Local Group. *AJ*, 144(1):4, Jul 2012.

[186] R. B. Metcalf and H. Zhao. Flux Ratios as a Probe of Dark Substructures in Quadruple-Image Gravitational Lenses. *ApJ*, 567:L5–L8, March 2002.

[187] Philip Mocz, Mark Vogelsberger, Victor H. Robles, Jesús Zavala, Michael Boylan-Kolchin, Anastasia Fialkov, and Lars Hernquist. Galaxy formation with BECDM - I. Turbulence and relaxation of idealized haloes. *MNRAS*, 471(4):4559–4570, November 2017.

[188] Ben Moore. Evidence against dissipation-less dark matter from observations of galaxy haloes. *Nature*, 370(6491):629–631, August 1994.

[189] Ben Moore, Sebastiano Ghigna, Fabio Governato, George Lake, Thomas Quinn, Joachim Stadel, and Paolo Tozzi. Dark Matter Substructure within Galactic Halos. *ApJ*, 524(1):L19–L22, Oct 1999.

[190] Ben Moore, Neal Katz, George Lake, Alan Dressler, and Augustus Oemler. Galaxy harassment and the evolution of clusters of galaxies. *Nature*, 379(6566):613–616, February 1996.

[191] B. P. Moster, T. Naab, and S. D. M. White. Galactic star formation and accretion histories from matching galaxies to dark matter haloes. *MNRAS*, 428:3121–3138, February 2013.

[192] Benjamin P. Moster, Rachel S. Somerville, Christian Maulbetsch, Frank C. van den Bosch, Andrea V. Macciò, Thorsten Naab, and Ludwig Oser. Constraints on the Relationship between Stellar Mass and Halo Mass at Low and High Redshift. *ApJ*, 710(2):903–923, February 2010.

[193] Norman Murray, Eliot Quataert, and Todd A. Thompson. On the Maximum Luminosity of Galaxies and Their Central Black Holes: Feedback from Momentum-driven Winds. *ApJ*, 618(2):569–585, January 2005.

[194] Shinya Nakashima, Yoshiyuki Inoue, Noriko Yamasaki, Yoshiaki Sofue, Jun Kataoka, and Kazuhiro Sakai. Spatial Distribution of the Milky Way Hot Gaseous Halo Constrained by Suzaku X-Ray Observations. *ApJ*, 862(1):34, July 2018.

[195] Julio F. Navarro, Vincent R. Eke, and Carlos S. Frenk. The cores of dwarf galaxy haloes. *MNRAS*, 283(3):L72–L78, December 1996.

[196] Julio F. Navarro, Carlos S. Frenk, and Simon D. M. White. The Structure of Cold Dark Matter Halos. *ApJ*, 462:563, May 1996.

[197] A. M. Nierenberg, T. Treu, S. A. Wright, C. D. Fassnacht, and M. W. Auger. Detection of substructure with adaptive optics integral field spectroscopy of the gravitational lens B1422+231. *MNRAS*, 442:2434–2445, August 2014.

[198] Jose Oñorbe, Michael Boylan-Kolchin, James S. Bullock, Philip F. Hopkins, Dušan Kereš, Claude-André Faucher-Giguère, Eliot Quataert, and Norman Murray. Forged in FIRE: cusps, cores and baryons in low-mass dwarf galaxies. *MNRAS*, 454(2):2092–2106, Dec 2015.

[199] Se-Heon Oh, W. J. G. de Blok, Elias Brinks, Fabian Walter, and Jr. Kennicutt, Robert C. Dark and Luminous Matter in THINGS Dwarf Galaxies. *AJ*, 141(6):193, June 2011.

[200] Se-Heon Oh, Deidre A. Hunter, Elias Brinks, Bruce G. Elmegreen, Andreas Schruba, Fabian Walter, Michael P. Rupen, Lisa M. Young, Caroline E. Simpson, Megan C. Johnson, Kimberly A. Herrmann, Dana Ficut-Vicas, Phil Cigan, Volker Heesen, Trisha Ashley, and Hong-Xin Zhang. High-resolution Mass Models of Dwarf Galaxies from LITTLE THINGS. *AJ*, 149(6):180, June 2015.

[201] Takashi Okamoto and Carlos S. Frenk. The origin of failed subhaloes and the common mass scale of the Milky Way satellite galaxies. *MNRAS*, 399(1):L174–L178, Oct 2009.

[202] Kyle A. Oman, Antonino Marasco, Julio F. Navarro, Carlos S. Frenk, Joop Schaye, and Alejandro Benítez-Llambay. Non-circular motions and the diversity of dwarf galaxy rotation curves. *MNRAS*, 482(1):821–847, January 2019.

[203] Kyle A. Oman, Julio F. Navarro, Azadeh Fattahi, Carlos S. Frenk, Till Sawala, Simon D. M. White, Richard Bower, Robert A. Crain, Michelle Furlong, Matthieu Schaller, Joop Schaye, and Tom Theuns. The unexpected diversity of dwarf galaxy rotation curves. *MNRAS*, 452(4):3650–3665, October 2015.

[204] Matthew E. Orr, Christopher C. Hayward, Philip F. Hopkins, T. K. Chan, Claude-André Faucher-Giguère, Robert Feldmann, Dušan Kereš, Norman Murray, and Eliot Quataert. What FIREs up star formation: the emergence of the Kennicutt-Schmidt law from feedback. *MNRAS*, 478(3):3653–3673, Aug 2018.

[205] Paolo Padoan, Troels Haugbølle, and Åke Nordlund. A Simple Law of Star Formation. *ApJ*, 759(2):L27, November 2012.

[206] Nondh Panithanpaisal, Robyn E. Sanderson, Andrew Wetzel, Emily C. Cunningham, Jeremy Bailin, and Claude-André Faucher-Giguère. The Galaxy Progenitors of Stellar Streams around Milky Way-mass Galaxies in the FIRE Cosmological Simulations. *arXiv e-prints*, page arXiv:2104.09660, April 2021.

[207] Stephen A. Pardy, Elena D'Onghia, Julio F. Navarro, Robert Grand, Facundo A. Gómez, Federico Marinacci, Rüdiger Pakmor, Christine Simpson, and Volker Springel. Satellites of Satellites: The Case for Carina and Fornax. *MNRAS*, 492(2):1543–1549, February 2020.

[208] J. Peñarrubia, D. Martínez-Delgado, H. W. Rix, M. A. Gómez-Flechoso, J. Munn, H. Newberg, E. F. Bell, B. Yanny, D. Zucker, and E. K. Grebel. A Comprehensive Model for the Monoceros Tidal Stream. *ApJ*, 626(1):128–144, June 2005.

[209] Jorge Peñarrubia, Andrew J. Benson, Matthew G. Walker, Gerard Gilmore, Alan W. McConnachie, and Lucio Mayer. The impact of dark matter cusps and cores on the satellite galaxy population around spiral galaxies. *MNRAS*, 406(2):1290–1305, Aug 2010.

[210] Jorge Peñarrubia, Julio F. Navarro, and Alan W. McConnachie. The Tidal Evolution of Local Group Dwarf Spheroidals. *ApJ*, 673(1):226–240, Jan 2008.

[211] Sarah Pearson, Gurtina Besla, Mary E. Putman, Katharina A. Lutz, Ximena Fernández, Sabrina Stierwalt, David R. Patton, Jinhyub Kim, Nitya Kallivayalil, Kelsey Johnson, and Eon-Chang Sung. Local Volume TiNy Titans: gaseous dwarf-dwarf interactions in the Local Universe. *MNRAS*, 459(2):1827–1846, June 2016.

[212] J. E. G. Peek, Carl Heiles, M. E. Putman, and Kevin Douglas. Low-Velocity Halo Clouds. *ApJ*, 692(1):827–838, February 2009.

[213] Annalisa Pillepich, Volker Springel, Dylan Nelson, Shy Genel, Jill Naiman, Rüdiger Pakmor, Lars Hernquist, Paul Torrey, Mark Vogelsberger, Rainer Weinberger, and Federico Marinacci. Simulating galaxy formation with the IllustrisTNG model. *MNRAS*, 473(3):4077–4106, January 2018.

[214] Andrew Pontzen and Fabio Governato. How supernova feedback turns dark matter cusps into cores. *MNRAS*, 421(4):3464–3471, April 2012.

[215] C. Power, J. F. Navarro, A. Jenkins, C. S. Frenk, S. D. M. White, V. Springel, J. Stadel, and T. Quinn. The inner structure of ΛCDM haloes - I. A numerical convergence study. *MNRAS*, 338:14–34, January 2003.

[216] William H. Press and Paul Schechter. Formation of Galaxies and Clusters of Galaxies by Self-Similar Gravitational Condensation. *ApJ*, 187:425–438, Feb 1974.

[217] D. J. Price and J. J. Monaghan. An energy-conserving formalism for adaptive gravitational force softening in smoothed particle hydrodynamics and N-body codes. *MNRAS*, 374(4):1347–1358, Feb 2007.

[218] Alireza Rahmati, Andreas H. Pawlik, Milan Raičević, and Joop Schaye. On the evolution of the H I column density distribution in cosmological simulations. *MNRAS*, 430(3):2427–2445, April 2013.

[219] J. I. Read and G. Gilmore. Mass loss from dwarf spheroidal galaxies: the origins of shallow dark matter cores and exponential surface brightness profiles. *MNRAS*, 356(1):107–124, January 2005.

[220] J. I. Read, G. Iorio, O. Agertz, and F. Fraternali. Understanding the shape and diversity of dwarf galaxy rotation curves in ΛCDM. *MNRAS*, 462(4):3628–3645, November 2016.

[221] J. I. Read, M. I. Wilkinson, N. Wyn Evans, G. Gilmore, and Jan T. Kleyna. The importance of tides for the Local Group dwarf spheroidals. *MNRAS*, 367(1):387–399, Mar 2006.

[222] Tao Ren, Anna Kwa, Manoj Kaplinghat, and Hai-Bo Yu. Reconciling the Diversity and Uniformity of Galactic Rotation Curves with Self-Interacting Dark Matter. *Physical Review X*, 9(3):031020, July 2019.

[223] Adam G. Riess, Alexei V. Filippenko, Peter Challis, Alejandro Clocchiatti, Alan Diercks, Peter M. Garnavich, Ron L. Gilliland, Craig J. Hogan, Saurabh Jha, Robert P. Kirshner, B. Leibundgut, M. M. Phillips, David Reiss, Brian P. Schmidt, Robert A. Schommer, R. Chris Smith, J. Spyromilio, Christopher Stubbs, Nicholas B. Suntzeff, and John Tonry. Observational Evidence from Supernovae for an Accelerating Universe and a Cosmological Constant. *AJ*, 116(3):1009–1038, September 1998.

[224] Victor H. Robles, James S. Bullock, Oliver D. Elbert, Alex Fitts, Alejandro González-Samaniego, Michael Boylan-Kolchin, Philip F. Hopkins, Claude-André Faucher-Giguère, Dušan Kereš, and Christopher C. Hayward. SIDM on FIRE: hydrodynamical self-interacting dark matter simulations of low-mass dwarf galaxies. *MNRAS*, 472(3):2945–2954, December 2017.

[225] Miguel Rocha, Annika H. G. Peter, and James Bullock. Infall times for Milky Way satellites from their present-day kinematics. *MNRAS*, 425(1):231–244, September 2012.

[226] Miguel Rocha, Annika H. G. Peter, James S. Bullock, Manoj Kaplinghat, Shea Garrison-Kimmel, Jose Oñorbe, and Leonidas A. Moustakas. Cosmological simulations with self-interacting dark matter - I. Constant-density cores and substructure. *MNRAS*, 430(1):81–104, March 2013.

[227] M. K. Rodriguez Wimberly, M. C. Cooper, S. P. Fillingham, M. Boylan-Kolchin, J. S. Bullock, and S. Garrison-Kimmel. The suppression of star formation on the smallest scales: what role does environment play? *MNRAS*, 483(3):4031–4039, March 2019.

[228] D. H. Rogstad, I. A. Lockhart, and M. C. H. Wright. Aperture-synthesis observations of H I in the galaxy M83. *ApJ*, 193:309–319, October 1974.

[229] Laura V. Sales, Federico Marinacci, Volker Springel, and Margarita Petkova. Stellar feedback by radiation pressure and photoionization. *MNRAS*, 439(3):2990–3006, April 2014.

[230] Laura V. Sales, Julio F. Navarro, Mario G. Abadi, and Matthias Steinmetz. Cosmic ménage à trois: the origin of satellite galaxies on extreme orbits. *MNRAS*, 379(4):1475–1483, August 2007.

[231] Laura V. Sales, Julio F. Navarro, Mario G. Abadi, and Matthias Steinmetz. Satellites of simulated galaxies: survival, merging and their relationto the dark and stellar haloes. *MNRAS*, 379(4):1464–1474, Aug 2007.

[232] Laura V. Sales, Julio F. Navarro, Andrew P. Cooper, Simon D. M. White, Carlos S. Frenk, and Amina Helmi. Clues to the 'Magellanic Galaxy' from cosmological simulations. *MNRAS*, 418(1):648–658, Nov 2011.

[233] Laura V. Sales, Julio F. Navarro, Nitya Kallivayalil, and Carlos S. Frenk. Identifying true satellites of the Magellanic Clouds. *MNRAS*, 465(2):1879–1888, Feb 2017.

[234] Laura V. Sales, Wenting Wang, Simon D. M. White, and Julio F. Navarro. Satellites and haloes of dwarf galaxies. *MNRAS*, 428(1):573–578, Jan 2013.

[235] Jenna Samuel, Andrew Wetzel, Erik Tollerud, Shea Garrison-Kimmel, Sarah Loebman, Kareem El-Badry, Philip F. Hopkins, Michael Boylan-Kolchin, Claude-André Faucher-Giguère, James S. Bullock, Samantha Benincasa, and Jeremy Bailin. A profile in FIRE: resolving the radial distributions of satellite galaxies in the Local Group with simulations. *MNRAS*, 491(1):1471–1490, January 2020.

[236] Isabel M. Santos-Santos, Arianna Di Cintio, Chris B. Brook, Andrea Macciò, Aaron Dutton, and Rosa Domínguez-Tenreiro. NIHAO - XIV. Reproducing the observed diversity of dwarf galaxy rotation curve shapes in ΛCDM. *MNRAS*, 473(4):4392–4403, February 2018.

[237] Isabel M. E. Santos-Santos, Azadeh Fattahi, Laura V. Sales, and Julio F. Navarro. Magellanic satellites in ΛCDM cosmological hydrodynamical simulations of the Local Group. *MNRAS*, 504(3):4551–4567, July 2021.

[238] Isabel M. E. Santos-Santos, Julio F. Navarro, Andrew Robertson, Alejandro Benítez-Llambay, Kyle A. Oman, Mark R. Lovell, Carlos S. Frenk, Aaron D. Ludlow, Azadeh Fattahi, and Adam Ritz. Baryonic clues to the puzzling diversity of dwarf galaxy rotation curves. *MNRAS*, 495(1):58–77, June 2020.

[239] Till Sawala, Carlos S. Frenk, Azadeh Fattahi, Julio F. Navarro, Richard G. Bower, Robert A. Crain, Claudio Dalla Vecchia, Michelle Furlong, John. C. Helly, Adrian Jenkins, Kyle A. Oman, Matthieu Schaller, Joop Schaye, Tom Theuns, James Trayford, and Simon D. M. White. The APOSTLE simulations: solutions to the Local Group's cosmic puzzles. *MNRAS*, 457(2):1931–1943, April 2016.

[240] Till Sawala, Pauli Pihajoki, Peter H. Johansson, Carlos S. Frenk, Julio F. Navarro, Kyle A. Oman, and Simon D. M. White. Shaken and stirred: the Milky Way's dark substructures. *MNRAS*, 467(4):4383–4400, Jun 2017.

[241] Matthieu Schaller, Carlos S. Frenk, Richard G. Bower, Tom Theuns, Adrian Jenkins, Joop Schaye, Robert A. Crain, Michelle Furlong, Claudio Dalla Vecchia, and I. G. McCarthy. Baryon effects on the internal structure of ΛCDM haloes in the EAGLE simulations. *MNRAS*, 451(2):1247–1267, August 2015.

[242] Joop Schaye, Robert A. Crain, Richard G. Bower, Michelle Furlong, Matthieu Schaller, Tom Theuns, Claudio Dalla Vecchia, Carlos S. Frenk, I. G. McCarthy, John C. Helly, Adrian Jenkins, Y. M. Rosas-Guevara, Simon D. M. White, Maarten Baes, C. M. Booth, Peter Camps, Julio F. Navarro, Yan Qu, Alireza Rahmati, Till Sawala, Peter A. Thomas, and James Trayford. The EAGLE project: simulating the evolution and assembly of galaxies and their environments. *MNRAS*, 446(1):521–554, January 2015.

[243] Vadim A. Semenov, Andrey V. Kravtsov, and Nickolay Y. Gnedin. Nonuniversal Star Formation Efficiency in Turbulent ISM. *ApJ*, 826(2):200, August 2016.

[244] Shi Shao, Marius Cautun, Alis J. Deason, Carlos S. Frenk, and Tom Theuns. Evolution of LMC/M33-mass dwarf galaxies in the EAGLE simulation. *MNRAS*, 479(1):284–296, Sep 2018.

[245] Shi Shao, Marius Cautun, Carlos S. Frenk, Robert J. J. Grand , Facundo A. Gómez, Federico Marinacci, and Christine M. Simpson. The multiplicity and anisotropy of galactic satellite accretion. *MNRAS*, 476(2):1796–1810, May 2018.

[246] J. D. Simon. Gaia Proper Motions and Orbits of the Ultra-faint Milky Way Satellites. *ApJ*, 863:89, August 2018.

[247] Joshua D. Simon. The Faintest Dwarf Galaxies. *arXiv e-prints*, page arXiv:1901.05465, Jan 2019.

[248] Joshua D. Simon and Marla Geha. The Kinematics of the Ultra-faint Milky Way Satellites: Solving the Missing Satellite Problem. *ApJ*, 670(1):313–331, November 2007.

[249] Christine M. Simpson, Robert J. J. Grand, Facundo A. Gómez, Federico Marinacci, Rüdiger Pakmor, Volker Springel, David J. R. Campbell, and Carlos S. Frenk. Quenching and ram pressure stripping of simulated Milky Way satellite galaxies. *MNRAS*, 478(1):548–567, Jul 2018.

[250] Evan D. Skillman, Matteo Monelli, Daniel R. Weisz, Sebastian L. Hidalgo, Antonio Aparicio, Edouard J. Bernard, Michael Boylan-Kolchin, Santi Cassisi, Andrew A. Cole, Andrew E. Dolphin, Henry C. Ferguson, Carme Gallart, Mike J. Irwin, Nicolas F. Martin, Clara E. Martínez-Vázquez, Lucio Mayer, Alan W. McConnachie, Kristen B. W. McQuinn, Julio F. Navarro, and Peter B. Stetson. The ISLAndS Project. II. The Lifetime Star Formation Histories of Six Andomeda dSphS. *ApJ*, 837(2):102, March 2017.

[251] Aaron Smith, Volker Bromm, and Abraham Loeb. Lyman α radiation hydrodynamics of galactic winds before cosmic reionization. *MNRAS*, 464(3):2963–2978, January 2017.

[252] Aaron Smith, Chalence Safranek-Shrader, Volker Bromm, and Miloš Milosavljević. The Lyman α signature of the first galaxies. *MNRAS*, 449(4):4336–4362, June 2015.

[253] Matthew C. Smith, Debora Sijacki, and Sijing Shen. Supernova feedback in numerical simulations of galaxy formation: separating physics from numerics. *MNRAS*, 478(1):302–331, July 2018.

[254] Rachel S. Somerville. Can Photoionization Squelching Resolve the Substructure Crisis? *ApJ*, 572(1):L23–L26, Jun 2002.

[255] David N. Spergel and Paul J. Steinhardt. Observational Evidence for Self-Interacting Cold Dark Matter. *Phys. Rev. Lett.*, 84(17):3760–3763, April 2000.

[256] V. Springel, J. Wang, M. Vogelsberger, A. Ludlow, A. Jenkins, A. Helmi, J. F. Navarro, C. S. Frenk, and S. D. M. White. The Aquarius Project: the subhaloes of galactic haloes. *MNRAS*, 391(4):1685–1711, December 2008.

[257] Volker Springel. The cosmological simulation code GADGET-2. *MNRAS*, 364(4):1105–1134, Dec 2005.

[258] Volker Springel. E pur si muove: Galilean-invariant cosmological hydrodynamical simulations on a moving mesh. *MNRAS*, 401(2):791–851, January 2010.

[259] Volker Springel, Tiziana Di Matteo, and Lars Hernquist. Modelling feedback from stars and black holes in galaxy mergers. *MNRAS*, 361(3):776–794, August 2005.

[260] Volker Springel and Lars Hernquist. Cosmological smoothed particle hydrodynamics simulations: a hybrid multiphase model for star formation. *MNRAS*, 339(2):289–311, February 2003.

[261] Volker Springel, Simon D. M. White, Adrian Jenkins, Carlos S. Frenk, Naoki Yoshida, Liang Gao, Julio Navarro, Robert Thacker, Darren Croton, and John Helly. Simulations of the formation, evolution and clustering of galaxies and quasars. *Nature*, 435(7042):629–636, Jun 2005.

[262] Jonathan Stern, Claude-André Faucher-Giguère, Drummond Fielding, Eliot Quataert, Zachary Hafen, Alexander B. Gurvich, Xiangcheng Ma, Lindsey Byrne, Kareem El-Badry, Daniel Anglés-Alcázar, T. K. Chan, Robert Feldmann, Dušan Kereš, Andrew Wetzel, Norman Murray, and Philip F. Hopkins. Virialization of the Inner CGM in the FIRE Simulations and Implications for Galaxy Disks, Star Formation, and Feedback. *ApJ*, 911(2):88, April 2021.

[263] S. Stierwalt, G. Besla, D. Patton, K. Johnson, N. Kallivayalil, M. Putman, G. Privon, and G. Ross. TiNy Titans: The Role of Dwarf-Dwarf Interactions in Low-mass Galaxy Evolution. *ApJ*, 805:2, May 2015.

[264] Greg Stinson, Anil Seth, Neal Katz, James Wadsley, Fabio Governato, and Tom Quinn. Star formation and feedback in smoothed particle hydrodynamic simulations - I. Isolated galaxies. *MNRAS*, 373(3):1074–1090, December 2006.

[265] L. E. Strigari, C. S. Frenk, and S. D. M. White. Kinematics of Milky Way satellites in a Lambda cold dark matter universe. *MNRAS*, 408:2364–2372, November 2010.

[266] Kung-Yi Su, Philip F. Hopkins, Christopher C. Hayward, Claude-André Faucher-Giguère, Dušan Kereš, Xiangcheng Ma, and Victor H. Robles. Feedback first: the surprisingly weak effects of magnetic fields, viscosity, conduction and metal diffusion on sub-L* galaxy formation. *MNRAS*, 471(1):144–166, Oct 2017.

[267] Max Tegmark, Joseph Silk, Martin J. Rees, Alain Blanchard, Tom Abel, and Francesco Palla. How Small Were the First Cosmological Objects? *ApJ*, 474:1, Jan 1997.

[268] Romain Teyssier, Andrew Pontzen, Yohan Dubois, and Justin I. Read. Cusp-core transformations in dwarf galaxies: observational predictions. *MNRAS*, 429(4):3068–3078, March 2013.

[269] F. K. Thielemann, D. Argast, F. Brachwitz, W. R. Hix, P. Höflich, M. Liebendörfer, G. Martinez-Pinedo, A. Mezzacappa, K. Nomoto, and I. Panov. Supernova Nucleosynthesis and Galactic Evolution. In Wolfgang Hillebrandt and Bruno Leibundgut, editors, *From Twilight to Highlight: The Physics of Supernovae*, page 331, January 2003.

[270] Erik J. Tollerud, Michael Boylan-Kolchin, and James S. Bullock. M31 satellite masses compared to ΛCDM subhaloes. *MNRAS*, 440(4):3511–3519, Jun 2014.

[271] Edouard Tollet, Andrea V. Macciò, Aaron A. Dutton, Greg S. Stinson, Liang Wang, Camilla Penzo, Thales A. Gutcke, Tobias Buck, Xi Kang, Chris Brook, Arianna Di Cintio, Ben W. Keller, and James Wadsley. NIHAO - IV: core creation and destruction in dark matter density profiles across cosmic time. *MNRAS*, 456(4):3542–3552, March 2016.

[272] G. Torrealba, V. Belokurov, S. E. Koposov, T. S. Li, M. G. Walker, J. L. Sanders, A. Geringer-Sameth, D. B. Zucker, K. Kuehn, and N. W. Evans. The hidden giant: discovery of an enormous Galactic dwarf satellite in Gaia DR2. *arXiv e-prints*, page arXiv:1811.04082, Nov 2018.

[273] G. Torrealba, S. E. Koposov, V. Belokurov, M. Irwin, M. Collins, M. Spencer, R. Ibata, M. Mateo, A. Bonaca, and P. Jethwa. At the survey limits: discovery of the Aquarius 2 dwarf galaxy in the VST ATLAS and the SDSS data. *MNRAS*, 463(1):712–722, Nov 2016.

[274] Sean Tulin and Hai-Bo Yu. Dark matter self-interactions and small scale structure. *Phys. Rep.*, 730:1–57, February 2018.

[275] Frank C. van den Bosch and Go Ogiya. Dark matter substructure in numerical simulations: a tale of discreteness noise, runaway instabilities, and artificial disruption. *MNRAS*, 475(3):4066–4087, April 2018.

[276] R. P. van der Marel and N. Kallivayalil. Third-epoch Magellanic Cloud Proper Motions. II. The Large Magellanic Cloud Rotation Field in Three Dimensions. *ApJ*, 781:121, February 2014.

[277] M. Vogelsberger, S. Genel, V. Springel, P. Torrey, D. Sijacki, D. Xu, G. Snyder, S. Bird, D. Nelson, and L. Hernquist. Properties of galaxies reproduced by a hydrodynamic simulation. *Nature*, 509(7499):177–182, May 2014.

[278] Mark Vogelsberger, Shy Genel, Debora Sijacki, Paul Torrey, Volker Springel, and Lars Hernquist. A model for cosmological simulations of galaxy formation physics. *MNRAS*, 436(4):3031–3067, December 2013.

[279] Mark Vogelsberger, Shy Genel, Volker Springel, Paul Torrey, Debora Sijacki, Dandan Xu, Greg Snyder, Dylan Nelson, and Lars Hernquist. Introducing the Illustris Project: simulating the coevolution of dark and visible matter in the Universe. *MNRAS*, 444(2):1518–1547, October 2014.

[280] Mark Vogelsberger, Federico Marinacci, Paul Torrey, and Ewald Puchwein. Cosmological simulations of galaxy formation. *Nature Reviews Physics*, 2(1):42–66, January 2020.

[281] Mark Vogelsberger, Jesus Zavala, and Abraham Loeb. Subhaloes in self-interacting galactic dark matter haloes. *MNRAS*, 423(4):3740–3752, July 2012.

[282] Mark Vogelsberger, Jesus Zavala, Christine Simpson, and Adrian Jenkins. Dwarf galaxies in CDM and SIDM with baryons: observational probes of the nature of dark matter. *MNRAS*, 444(4):3684–3698, November 2014.

[283] J. W. Wadsley, J. Stadel, and T. Quinn. Gasoline: a flexible, parallel implementation of TreeSPH. *New Astron.*, 9(2):137–158, February 2004.

[284] Bart Wakker, J. Chris Howk, You-Hua Chu, Dominik Bomans, and Sean D. Points. Coronal C^{+3} in the Large Magellanic Cloud: Evidence for a Hot Halo. *ApJ*, 499(1):L87–L91, May 1998.

[285] Matthew G. Walker and Jorge Peñarrubia. A Method for Measuring (Slopes of) the Mass Profiles of Dwarf Spheroidal Galaxies. *ApJ*, 742(1):20, November 2011.

[286] Liang Wang, Aaron A. Dutton, Gregory S. Stinson, Andrea V. Macciò, Camilla Penzo, Xi Kang, Ben W. Keller, and James Wadsley. NIHAO project - I. Reproducing the inefficiency of galaxy formation across cosmic time with a large sample of cosmological hydrodynamical simulations. *MNRAS*, 454(1):83–94, November 2015.

[287] Wenting Wang, Laura V. Sales, Bruno M. B. Henriques, and Simon D. M. White. Satellite abundances around bright isolated galaxies - II. Radial distribution and environmental effects. *MNRAS*, 442(2):1363–1378, August 2014.

[288] Rainer Weinberger, Volker Springel, and Rüdiger Pakmor. The AREPO Public Code Release. *ApJS*, 248(2):32, June 2020.

[289] Daniel R. Weisz, Julianne J. Dalcanton, Benjamin F. Williams, Karoline M. Gilbert, Evan D. Skillman, Anil C. Seth, Andrew E. Dolphin, Kristen B. W. McQuinn, Stephanie M. Gogarten, Jon Holtzman, Keith Rosema, Andrew Cole, Igor D. Karachentsev, and Dennis Zaritsky. The ACS Nearby Galaxy Survey Treasury. VIII. The Global Star Formation Histories of 60 Dwarf Galaxies in the Local Volume. *ApJ*, 739(1):5, September 2011.

[290] Daniel R. Weisz, Andrew E. Dolphin, Evan D. Skillman, Jon Holtzman, Karoline M. Gilbert, Julianne J. Dalcanton, and Benjamin F. Williams. The Star Formation Histories of Local Group Dwarf Galaxies. I. Hubble Space Telescope/Wide Field Planetary Camera 2 Observations. *ApJ*, 789(2):147, July 2014.

[291] Daniel R. Weisz, Andrew E. Dolphin, Evan D. Skillman, Jon Holtzman, Karoline M. Gilbert, Julianne J. Dalcanton, and Benjamin F. Williams. The Star Formation Histories of Local Group Dwarf Galaxies. III. Characterizing Quenching in Low-mass Galaxies. *ApJ*, 804(2):136, May 2015.

[292] Andrew R. Wetzel, Alis J. Deason, and Shea Garrison-Kimmel. Satellite Dwarf Galaxies in a Hierarchical Universe: Infall Histories, Group Preprocessing, and Reionization. *ApJ*, 807(1):49, Jul 2015.

[293] Andrew R. Wetzel, Philip F. Hopkins, Ji-hoon Kim, Claude-André Faucher-Giguère, Dušan Kereš, and Eliot Quataert. Reconciling Dwarf Galaxies with ΛCDM Cosmology: Simulating a Realistic Population of Satellites around a Milky Way-mass Galaxy. *ApJ*, 827(2):L23, Aug 2016.

[294] Andrew R. Wetzel and Daisuke Nagai. The Physical Nature of the Cosmic Accretion of Baryons and Dark Matter into Halos and Their Galaxies. *ApJ*, 808(1):40, Jul 2015.

[295] Andrew R. Wetzel, Erik J. Tollerud, and Daniel R. Weisz. Rapid Environmental Quenching of Satellite Dwarf Galaxies in the Local Group. *ApJ*, 808(1):L27, July 2015.

[296] Coral Wheeler, Philip F. Hopkins, Andrew B. Pace, Shea Garrison-Kimmel, Michael Boylan-Kolchin, Andrew Wetzel, James S. Bullock, Dusan Keres, Claude-Andre Faucher-Giguere, and Eliot Quataert. Be it therefore resolved: Cosmological Simulations of Dwarf Galaxies with Extreme Resolution. *arXiv e-prints*, page arXiv:1812.02749, Dec 2018.

[297] Coral Wheeler, Jose Oñorbe, James S. Bullock, Michael Boylan-Kolchin, Oliver D. Elbert, Shea Garrison-Kimmel, Philip F. Hopkins, and Dušan Kereš. Sweating the small stuff: simulating dwarf galaxies, ultra-faint dwarf galaxies, and their own tiny satellites. *MNRAS*, 453(2):1305–1316, Oct 2015.

[298] Coral Wheeler, John I. Phillips, Michael C. Cooper, Michael Boylan-Kolchin, and James S. Bullock. The surprising inefficiency of dwarf satellite quenching. *MNRAS*, 442(2):1396–1404, August 2014.

[299] S. D. M. White and M. J. Rees. Core condensation in heavy halos: a two-stage theory for galaxy formation and clustering. *MNRAS*, 183:341–358, May 1978.

[300] J. Wolf, G. D. Martinez, J. S. Bullock, M. Kaplinghat, M. Geha, R. R. Muñoz, J. D. Simon, and F. F. Avedo. Accurate masses for dispersion-supported galaxies. *MNRAS*, 406:1220–1237, August 2010.

[301] A. H. Wright, A. S. G. Robotham, S. P. Driver, M. Alpaslan, S. K. Andrews, I. K. Baldry, J. Bland -Hawthorn, S. Brough, M. J. I. Brown, and M. Colless. Galaxy And Mass Assembly

(GAMA): the galaxy stellar mass function to z = 0.1 from the r-band selected equatorial regions. *MNRAS*, 470(1):283–302, Sep 2017.

[302] X. Yang, H. J. Mo, and F. C. van den Bosch. Constraining galaxy formation and cosmology with the conditional luminosity function of galaxies. *MNRAS*, 339:1057–1080, March 2003.

[303] X. Yang, H. J. Mo, Y. Zhang, and F. C. van den Bosch. An Analytical Model for the Accretion of Dark Matter Subhalos. *ApJ*, 741:13, November 2011.

[304] J. H. Yoon, K. V. Johnston, and D. W. Hogg. Clumpy Streams from Clumpy Halos: Detecting Missing Satellites with Cold Stellar Structures. *ApJ*, 731:58, April 2011.

[305] Naoki Yoshida, Volker Springel, Simon D. M. White, and Giuseppe Tormen. Weakly Self-interacting Dark Matter and the Structure of Dark Halos. *ApJ*, 544(2):L87–L90, December 2000.

[306] Sijie Yu, James S. Bullock, Andrew Wetzel, Robyn E. Sanderson, Andrew S. Graus, Michael Boylan-Kolchin, Anna M. Nierenberg, Michael Y. Grudić, Philip F. Hopkins, Dušan Kereš, and Claude-André Faucher-Giguère. Stars made in outflows may populate the stellar halo of the Milky Way. *MNRAS*, 494(2):1539–1559, May 2020.

[307] Jesús Zavala, Mark R. Lovell, Mark Vogelsberger, and Jan D. Burger. Diverse dark matter density at sub-kiloparsec scales in Milky Way satellites: Implications for the nature of dark matter. *Phys. Rev. D*, 100(6):063007, September 2019.

[308] Adi Zolotov, Alyson M. Brooks, Beth Willman, Fabio Governato, Andrew Pontzen, Charlotte Christensen, Avishai Dekel, Tom Quinn, Sijing Shen, and James Wadsley. Baryons Matter: Why Luminous Satellite Galaxies have Reduced Central Masses. *ApJ*, 761(1):71, December 2012.